

# Search for New Physics in All-hadronic Events with AlphaT in 8 TeV Data at CERN

by

Yossof Eshaq

Submitted in Partial Fulfillment of the

Requirements for the Degree

Doctor of Philosophy

Supervised by Professor Aran Garcia-Bellido

Department of Physics & Astronomy

Arts, Sciences and Engineering

School of Arts and Sciences

University of Rochester

Rochester, New York

2014



### Abstract

An inclusive search for supersymmetric processes that produce final states with jets and missing transverse energy is performed in pp collisions at a centre-of-mass energy of  $\sqrt{s} = 8$  TeV. The data sample corresponds to an integrated luminosity of  $19.5 \text{ fb}^{-1}$  collected by the CMS experiment at the LHC. In this search, a dimensionless kinematic variable,  $\alpha_T$ , is used to discriminate between events with genuine and misreconstructed missing transverse energy. The search is based on an examination of the number of reconstructed jets per event, the scalar sum of transverse energies of these jets, and the number of these jets identified as originating from bottom quarks. The results are interpreted in two simplified models with direct stop production.



## Contents

<b>Abstract</b>	<b>i</b>
<b>Contents</b>	<b>iii</b>
<b>List of Figures</b>	<b>vii</b>
<b>List of Tables</b>	<b>xv</b>
<b>1 Introduction</b>	<b>1</b>
<b>2 Theoretical motivation</b>	<b>2</b>
2.1 The Standard Model . . . . .	2
2.2 Supersymmetry . . . . .	3
2.3 R-parity and a candidate for dark matter . . . . .	4
2.4 Experimental signature . . . . .	5
<b>3 The Experiment</b>	<b>7</b>
3.1 The Large Hadron Collider . . . . .	7
3.1.1 High energy proton collisions . . . . .	8
3.2 The Compact Muon Solenoid detector . . . . .	10
3.2.1 The detector . . . . .	10
3.2.2 Event reconstruction . . . . .	14
<b>4 Data sets and simulated samples</b>	<b>17</b>
4.1 Data sets . . . . .	17
4.2 Simulated samples for SM backgrounds . . . . .	17
4.3 Corrections to cross sections for SM samples . . . . .	17
<b>5 Event Selection</b>	<b>21</b>
5.1 Data . . . . .	22

5.2	Event quality . . . . .	22
5.3	Physics objects . . . . .	22
5.3.1	Jets . . . . .	23
5.3.2	Muons . . . . .	23
5.3.3	Photons . . . . .	24
5.3.4	Electrons . . . . .	25
5.3.5	Missing transverse energy . . . . .	25
5.3.6	Single isolated tracks . . . . .	26
5.4	Triggers . . . . .	26
5.4.1	Hadronic search region and control samples . . . . .	26
5.5	Object vetoes . . . . .	28
5.6	Hadronic pre-selection . . . . .	29
5.7	Definition of $\alpha_T$ . . . . .	30
5.8	Final selections . . . . .	33
<b>6</b>	<b>Background estimation for processes with genuine <math>\cancel{E}_T</math></b>	<b>35</b>
6.1	Overview of the method . . . . .	36
6.2	Definition of the control samples . . . . .	38
6.2.1	Muon and photon triggers . . . . .	38
6.2.2	The $\mu$ + jets control sample . . . . .	39
6.2.3	The $\gamma$ + jets control sample . . . . .	40
<b>7</b>	<b>Closure tests and systematic uncertainties on translation factors</b>	<b>41</b>
7.1	Closure tests . . . . .	41
7.2	Systematic uncertainties from closure tests . . . . .	44
<b>8</b>	<b>Statistical framework</b>	<b>47</b>
8.1	Likelihood model . . . . .	47
8.1.1	Hadronic sample . . . . .	47
8.1.2	Electroweak control samples . . . . .	47

8.1.3	Contributions from signal . . . . .	49
8.1.4	Total likelihood . . . . .	50
<b>9</b>	<b>Results</b>	<b>51</b>
9.1	Standard Model . . . . .	51
<b>10</b>	<b>Signal models and efficiencies</b>	<b>60</b>
10.1	Introduction . . . . .	60
10.2	Efficiency times acceptance . . . . .	61
10.3	Systematic uncertainties on signal efficiency times acceptance . . . . .	63
10.3.1	Introduction . . . . .	63
10.3.2	PDF uncertainties . . . . .	63
10.3.3	Jet energy scale . . . . .	64
10.3.4	Initial state radiation . . . . .	64
10.3.5	b-tag scale factor corrections . . . . .	65
10.3.6	Total systematic uncertainties . . . . .	65
<b>11</b>	<b>Limits on SMS production cross sections</b>	<b>69</b>
11.1	Limit setting procedure . . . . .	69
11.2	Upper limits on SMS models . . . . .	70
11.2.1	Upper limits on T2cc . . . . .	70
11.2.2	Upper limits on T2tt . . . . .	71
11.3	Summary . . . . .	75
<b>A</b>	<b>Detailed example of background estimation</b>	<b>76</b>
<b>B</b>	<b>Background estimation from control samples</b>	<b>78</b>
<b>C</b>	<b>Maximum likelihood parameter values</b>	<b>82</b>
<b>D</b>	<b>SM-only yield tables</b>	<b>89</b>

<b>E</b>	<b>Efficiencies and systematic uncertainties for simplified models</b>	<b>92</b>
E.1	T2cc . . . . .	92
E.2	T2tt . . . . .	97



## List of Figures

2.1	A simulation of a hadronized quark in the CMS detector. The resulting particles from hadronization are grouped into a jet (gray cone). . . . .	5
2.2	Two Feynman diagrams depicting the top squark production and decay, in which $P$ represents a proton, $t$ a top quark, $c$ a charm quark, $\tilde{t}$ a top squark, $\tilde{\chi}_1^0$ a neutralino. . . . .	6
3.1	Left: a geographical map of the location of the LHC. Right: the layout of LHC.	8
3.2	The luminosity integrated over the course of the three separate proton-proton collision runs as recorded by CMS. Note: the 2010 curve is multiplied by 100 for legibility. . . . .	9
3.3	Left: the cross sections (in nb) of various SM processes vs. center-of-mass energy in $pp$ collisions when $\sqrt{s} > 1$ TeV, from Ref. [8]. Right: The cross sections (in pb) of various SUSY processes vs. sparticle for $pp$ collisions at $\sqrt{s} = 14$ TeV. From Ref. [9]. . . . .	10
3.4	Top: a view of one quadrant of CMS. The volume enclosing the tracker is shown in light red, the electromagnetic calorimeter in light green, the hadron calorimeter in lavender, and the forward calorimeter in magenta. The muon detectors are labeled, from Ref. [11], Bottom: a perspective view of CMS from Ref. [10]. . . . .	12
3.5	The relative $p_T$ resolution as a function of jet $p_T$ for central jets. . . . .	16
4.1	Generator-level $H_T^{\text{parton}}$ distributions and measured weights . . . . .	20
5.1	$H_T$ distribution after basic preselection, for $35 \text{ pb}^{-1}$ of data collected at 7 TeV as well as for all SM backgrounds and two SUSY signal samples, from Ref. [23]. This figure is for illustrative purposes only, as these specific SUSY models are not under study in this analysis. . . . .	21
5.2	Cumulative efficiency turn-on curves for the $H_T$ - $\alpha_T$ cross triggers (as summarized in Table 7) that record events for the three lowest $H_T$ bins for events satisfying $2 \leq n_{\text{jet}} \leq 3$ (left) and $n_{\text{jet}} \geq 4$ (right). . . . .	28

5.3	The $\alpha_T$ distribution for $11.7 \text{ fb}^{-1}$ of data collected at 8 TeV as well as for all SM backgrounds and one example SUSY signal sample, from Ref. [36]. This figure is for illustrative purposes only, as this analysis relies on data control samples to estimate contribution from SM process with genuine $\cancel{E}_T$ . . . . .	31
5.4	Data–MC comparison of the $\alpha_T$ distribution after the application of the hadronic pre-selection criteria for events satisfying $n_{\text{jet}} > 2$ and $n_b > 0$ in histograms with (a) coarse and (b) fine binning. . . . .	32
5.5	Data–MC comparisons of key variables for the hadronic search region, following the application of the full hadronic selection criteria and the requirements $H_T > 375 \text{ GeV}$ and $\alpha_T > 0.55$ : (a) $n_{\text{jet}}$ , (b) $n_b$ , (c) $\cancel{H}_T$ , and (d) $\cancel{E}_T$ distributions for an inclusive selection on $n_{\text{jet}}$ and $n_b$ , and (e,f) $H_T$ for the two event categories ( $2 \leq n_{\text{jet}} \leq 3, n_b = 0$ ) and ( $n_{\text{jet}} \geq 4, n_b = 1$ ). . . . .	34
6.1	(left) Muon trigger efficiency as a function of number of primary vertices for muon $p_T > 25 \text{ GeV}$ and $ \eta  < 2.1$ . (right) Number of primary vertices in muon control sample. . . . .	38
6.2	Cumulative efficiency turn-on curves for the HLT_Photon150 trigger as a function of photon $p_T$ for events satisfying $2 \leq n_{\text{jet}} \leq 3$ (left) and $n_{\text{jet}} \geq 4$ (right). . . . .	39
7.1	Sets of closure tests (open symbols) overlaid on top of the systematic uncertainty used for each of the $H_T$ region (shaded bands) and for the two different jet multiplicity bins: (a) $2 \leq n_{\text{jet}} \leq 3$ and (b) $n_{\text{jet}} \geq 4$ . . . . .	42
9.1	Pulls and p-values. See text for details . . . . .	52

- 9.2 Comparison of the  $H_T$ -binned observed data yields and SM expectations when requiring  $2 \leq n_{\text{jet}} \leq 3$  and  $n_b = 0$  for the (a-b) hadronic, (c)  $\mu + \text{jets}$ , (d)  $\mu\mu + \text{jets}$  and (e)  $\gamma + \text{jets}$  samples, as determined by a simultaneous fit to all data samples under the SM-only hypothesis. The observed event yields in data (black dots) and the expectations and their uncertainties (dark blue solid line with light blue bands), as determined by the simultaneous fit, are shown. For illustrative purposes only, the signal expectations (pink dashed line) for the model T2cc with  $m_{\tilde{q}} = 250 \text{ GeV}$  and  $m_{\text{LSP}} = 240 \text{ GeV}$  are stacked on top of the SM expectations. . . . . 54
- 9.3 Comparison of the  $H_T$ -binned observed data yields and SM expectations when requiring  $2 \leq n_{\text{jet}} \leq 3$  and  $n_b = 1$  for the (a-b) hadronic, (c)  $\mu + \text{jets}$ , (d)  $\mu\mu + \text{jets}$  and (e)  $\gamma + \text{jets}$  samples, as determined by a simultaneous fit to all data samples under the SM-only hypothesis. The observed event yields in data (black dots) and the expectations and their uncertainties (dark blue solid line with light blue bands), as determined by the simultaneous fit, are shown. For illustrative purposes only, the signal expectations (pink dashed line) for the model T2cc with  $m_{\tilde{q}} = 250 \text{ GeV}$  and  $m_{\text{LSP}} = 170 \text{ GeV}$  are stacked on top of the SM expectations. . . . . 55
- 9.4 Comparison of the  $H_T$ -binned observed data yields and SM expectations when requiring  $2 \leq n_{\text{jet}} \leq 3$  and  $n_b = 2$  for the (a-b) hadronic and  $\mu + \text{jets}$  samples, as determined by a simultaneous fit to both the hadronic and  $\mu + \text{jets}$  data samples under the SM-only hypothesis. The observed event yields in data (black dots) and the expectations and their uncertainties (dark blue solid line with light blue bands), as determined by the simultaneous fit, are shown. . . . 56

- 9.5 Comparison of the  $H_T$ -binned observed data yields and SM expectations when requiring  $n_{\text{jet}} \geq 4$  and  $n_b = 0$  for the (a-b) hadronic, (c)  $\mu + \text{jets}$ , (d)  $\mu\mu + \text{jets}$  and (e)  $\gamma + \text{jets}$  samples, as determined by a simultaneous fit to all data samples under the SM-only hypothesis. The observed event yields in data (black dots) and the expectations and their uncertainties (dark blue solid line with light blue bands), as determined by the simultaneous fit, are shown. For illustrative purposes only, the signal expectations (pink dashed line) for the model T2cc with  $m_{\tilde{q}} = 250 \text{ GeV}$  and  $m_{\text{LSP}} = 170 \text{ GeV}$  are stacked on top of the SM expectations. . . . . 57
- 9.6 Comparison of the  $H_T$ -binned observed data yields and SM expectations when requiring  $n_{\text{jet}} \geq 4$  and  $n_b = 1$  for the (a-b) hadronic, (c)  $\mu + \text{jets}$ , (d)  $\mu\mu + \text{jets}$  and (e)  $\gamma + \text{jets}$  samples, as determined by a simultaneous fit to all data samples under the SM-only hypothesis. The observed event yields in data (black dots) and the expectations and their uncertainties (dark blue solid line with light blue bands), as determined by the simultaneous fit, are shown. For illustrative purposes only, the signal expectations (pink dashed line) for the model T2cc with  $m_{\tilde{q}} = 250 \text{ GeV}$  and  $m_{\text{LSP}} = 170 \text{ GeV}$  are stacked on top of the SM expectations. . . . . 58
- 9.7 Comparison of the  $H_T$ -binned observed data yields and SM expectations when requiring  $n_{\text{jet}} \geq 4$  and  $n_b = 2$  for the (a-b) hadronic and  $\mu + \text{jets}$  samples, as determined by a simultaneous fit to both the hadronic and  $\mu + \text{jets}$  data samples under the SM-only hypothesis. The observed event yields in data (black dots) and the expectations and their uncertainties (dark blue solid line with light blue bands), as determined by the simultaneous fit, are shown. . . . . 59
- 10.1 Hadronic selection efficiency times acceptance for T2cc for the relevant event categories defined by  $n_{\text{jet}}$  and  $n_b$ . Note the different z-axis scales. . . . . 61
- 10.2 Hadronic selection efficiency times acceptance for the T2tt for the relevant event categories defined by  $n_{\text{jet}}$  and  $n_b$ . Note the different z-axis scales. . . . 62

10.3	The total systematic uncertainty in the signal efficiency times acceptance for all relevant event categories for the T2cc interpretation. . . . .	66
10.4	The total systematic uncertainty in the signal efficiency times acceptance for all relevant event categories for the T2tt interpretation. . . . .	67
11.1	The distributions of the test statistic $q_\mu$ in the background-only (red, on the right) and signal+background (blue, on the left) hypotheses. The black line represents the value of the $q_\mu$ on the tested data. The shaded areas represent $1 - CL_b$ (red) and $CL_{s+b}$ (blue). From [62] . . . . .	70
11.2	(a) shows the expected and observed upper limits on the production cross section for the for the model T2cc obtained in this analysis. See text for detail on each curve. (b) shows exclusion region in the same model obtained by the ATLAS collaboration, from [64] . . . . .	71
11.3	Expected and observed upper limits on the production cross section for the for the models T2tt (bottom). . . . .	72
11.4	Pulls in categories used in T2cc interpretation. . . . .	73
11.5	The $H_T$ -binned signal significance defined as the signal yield divided by the $\sqrt{b + (.1b)^2}$ where $b$ is the SM expectation obtained by a fit to all control data samples under the SM-only background hypothesis for the two categories (a) $n_{\text{jet}} \geq 4$ , $n_b = 1$ and (b) $n_{\text{jet}} \geq 4$ , $n_b = 2$ simultaneously. The signal model is T2tt with $m_{\tilde{t}} = 400$ GeV and $m_{\text{LSP}} = 100$ GeV. . . . .	73
11.6	The comparison of the $H_T$ -binned observed data yields and expectations for the hadronic sample, as determined by a simultaneous fit to all data samples under the signal plus SM background hypothesis. The observed event yields in data (black dots), the SM expectations (dark blue solid line), and the signal expectations (pink solid line), as determined by the simultaneous fit, for the signal model T2tt with $m_{\tilde{t}} = 400$ GeV and $m_{\text{LSP}} = 100$ GeV. Two event categories are considered: (a) $n_{\text{jet}} \geq 4$ and $n_b = 1$ , (b) $n_{\text{jet}} \geq 4$ and $n_b = 2$ . . .	74

11.7	The profile likelihood ratio (defined in sec. 11.1) as a function of the signal strength. The likelihood considers all data samples under the signal plus SM background hypothesis for the signal model $T2t\bar{t}$ with $m_{\tilde{t}} = 400$ GeV and $m_{LSP} = 100$ GeV. The minimum defines the signal strength estimate which maximizes the likelihood and the green vertical line on the right of the minimum indicates the upper-limit at 95% confidence level. . . . .	74
E.1	Ratio of efficiency times acceptance for the (middle) central value, (top) $+1\sigma$ value, (bottom) $-1\sigma$ value of the envelope calculation relative to the nominal PDF set used to produce the $T2cc$ sample. . . . .	92
E.2	The fractional change in signal efficiency due to systematically (Left) increasing and (Middle) decreasing all jet energies, and (Right) the resulting (symmetric) systematic uncertainties due to JES uncertainties for $T2cc$ . . . . .	93
E.3	The fractional change in signal efficiency due to systematically (Left) increasing and (Middle) decreasing event weights according to ISR uncertainties, and (Right) the resulting (symmetric) systematic uncertainties due to ISR uncertainties for $T2cc$ . . . . .	94
E.4	The fractional change in signal efficiency due to systematically (Left) increasing and (Middle) decreasing all b-tag efficiencies according to the scale factor uncertainties, and (Right) the resulting (symmetric) systematic uncertainties due to b-tag scale factor uncertainties for $T2cc$ . . . . .	95
E.5	The total systematic uncertainty in the signal efficiency times acceptance for all relevant event categories for the $T2cc$ interpretation. . . . .	96
E.6	Ratio of efficiency times acceptance for the (middle) central value, (top) $+1\sigma$ value, (bottom) $-1\sigma$ value of the envelope calculation relative to the nominal PDF set used to produce the $T2t\bar{t}$ sample. . . . .	97
E.7	The fractional change in signal efficiency due to systematically (Left) increasing and (Middle) decreasing all jet energies, and (Right) the resulting (symmetric) systematic uncertainties due to JES uncertainties for $T2t\bar{t}$ . . . . .	98

---

E.8	The fractional change in signal efficiency due to systematically (Left) increasing and (Middle) decreasing event weights according to ISR uncertainties, and (Right) the resulting (symmetric) systematic uncertainties due to ISR uncertainties for $T2t\bar{t}$ . . . . .	99
E.9	The fractional change in signal efficiency due to systematically (Left) increasing and (Middle) decreasing all b-tag efficiencies according to the scale factor uncertainties, and (Right) the resulting (symmetric) systematic uncertainties due to b-tag scale factor uncertainties for $T2t\bar{t}$ . . . . .	100





## List of Tables

1	Datasets. . . . .	17
2	MC samples for Standard Model processes. . . . .	18
3	Corrections determined from a data sideband for the W + jets and $t\bar{t}$ samples. “Corrected yield” reflects the observed data yield minus the contamination as given by MC. . . . .	19
4	Muon identification (Tight working point). . . . .	24
5	Photon identification (Tight working point). . . . .	24
6	Electron identification (Veto working point). . . . .	25
7	List of signal triggers and their efficiencies (%), as measured in the SingleMu data. The trigger efficiency is $\sim 100\%$ for all bins above $H_T > 675$ GeV. . . .	27
8	Jet $p_T$ thresholds per $H_T$ bin. . . . .	30
9	Summary of control samples used to predict the SM background for each event category. . . . .	37
10	A summary of the results obtained from fits of zeroth order polynomials (i.e. a constant) to binned $H_T$ distributions for four sets of closure tests performed in the $2 \leq n_{\text{jet}} \leq 3$ bin. . . . .	44
11	A summary of the results obtained from fits of zeroth order polynomials (i.e. a constant) to three sets of closure tests performed in the $n_{\text{jet}} \geq 4$ bin. <sup>†</sup> Further explanation of this fit can be found in the text. . . . .	44
12	A summary of the results obtained from fits of zeroth order polynomials (i.e. a constant) to four sets of closure tests ( $2 \leq n_{\text{jet}} \leq 3 \rightarrow n_{\text{jet}} \geq 4$ ) that probe the accuracy of the MC modeling of the $n_{\text{jet}}$ distribution observed in data, using the three data control samples. . . . .	45
13	A summary of the magnitude of the systematic uncertainties (%) obtain from closure tests, according to $n_{\text{jet}}$ and $H_T$ region. . . . .	45
14	A summary of the magnitude of the total systematic uncertainties (%) assigned to the translation factors, according to $n_{\text{jet}}$ and $H_T$ region. . . . .	45

15	Summary of hadronic yields from fit. . . . .	53
16	A summary of the simplified models considered for interpretation. The event categories considered for each model are listed. . . . .	60
17	Sparticle system $p_T$ dependent corrections and systematic weight variations. .	65
18	Representative ranges for each contribution to the total systematic uncertainty in the signal efficiency times acceptance for each relevant event category for the T2cc interpretation. . . . .	67
19	Representative ranges for each contribution to the total systematic uncertainty in the signal efficiency times acceptance for each relevant event category for the T2tt interpretation. . . . .	68
20	Photon Sample Predictions Normalized to $19.5\text{fb}^{-1}$ ( $2 \leq n_{\text{jet}} \leq 3, n_b = 0$ ) .	78
21	Muon Sample Predictions Normalized to $19.5\text{fb}^{-1}$ ( $2 \leq n_{\text{jet}} \leq 3, n_b = 0$ ) . .	78
22	Photon Sample Predictions Normalized to $19.5\text{fb}^{-1}$ ( $n_{\text{jet}} \geq 4, n_b = 0$ ) . . . .	79
23	Muon Sample Predictions Normalized to $19.5\text{fb}^{-1}$ ( $n_{\text{jet}} \geq 4, n_b = 0$ ) . . . . .	79
24	Photon Sample Predictions Normalized to $19.5\text{fb}^{-1}$ ( $2 \leq n_{\text{jet}} \leq 3, n_b = 1$ ) .	79
25	Muon Sample Predictions Normalized to $19.5\text{fb}^{-1}$ ( $2 \leq n_{\text{jet}} \leq 3, n_b = 1$ ) . .	80
26	Photon Sample Predictions Normalized to $19.5\text{fb}^{-1}$ ( $n_{\text{jet}} \geq 4, n_b = 1$ ) . . . .	80
27	Muon Sample Predictions Normalized to $19.5\text{fb}^{-1}$ ( $n_{\text{jet}} \geq 4, n_b = 1$ ) . . . . .	80
28	Muon Sample Predictions Normalized to $19.5\text{fb}^{-1}$ ( $2 \leq n_{\text{jet}} \leq 3, n_b = 2$ ) . .	81
29	Muon Sample Predictions Normalized to $19.5\text{fb}^{-1}$ ( $n_{\text{jet}} \geq 4, n_b = 2$ ) . . . . .	81
30	SM-only maximum-likelihood parameter values (0b le3j). . . . .	83
31	SM-only maximum-likelihood parameter values (1b le3j). . . . .	84
32	SM-only maximum-likelihood parameter values (2b le3j). . . . .	85
33	SM-only maximum-likelihood parameter values (0b ge4j). . . . .	86
34	SM-only maximum-likelihood parameter values (1b ge4j). . . . .	87
35	SM-only maximum-likelihood parameter values (2b ge4j). . . . .	88
36	0b le3j . . . . .	89
37	0b ge4j . . . . .	89
38	1b le3j . . . . .	90

---

39	1b ge4j . . . . .	90
40	2b le3j . . . . .	90
41	2b ge4j . . . . .	91



## 1 Introduction

**Intro from AN: NEED TO BE CHANGED** A search for an excess of events in data over the Standard Model expectation is performed in multijet final-states with significant  $\cancel{E}_T$ . The dominant background is multijet production, a manifestation of quantum chromodynamics (QCD), which is suppressed by very tight requirements on the  $\alpha_T$  variable to a negligible level. To estimate the remaining significant backgrounds, we make use of four data control samples: a  $\mu$  + jets sample to determine the background from  $W$  + jets,  $t\bar{t}$  and single top events; a  $\gamma$  + jets sample to determine the irreducible background from  $Z \rightarrow \nu\bar{\nu}$  + jets events; a  $\mu\mu$  + jets sample that is also used to determine the  $Z \rightarrow \nu\bar{\nu}$  + jets background; and finally a multijet-enriched hadronic control sample to determine any residual contribution from multijet production.

## 2 Theoretical motivation

### 2.1 The Standard Model

Particle physics concerns itself with the study of particles and fields. Our current knowledge of their characteristics and interactions are formalized in the quantum field theory called the Standard Model [1, 2] which relies upon symmetry principles. The global symmetry group of the Standard Model is given by three symmetries: the color charge symmetry of Quantum Chromo Dynamics (QCD) represented in  $SU(3)$ , the flavor symmetry of Quantum Flavor Dynamics (QFD) represented in  $SU(2)$  and the electric charge symmetry of Quantum Electro Dynamics represented in  $U(1)$ . Together,  $SU(3) \times SU(2) \times U(1)$  requires the SM Lagrangian be invariant under local gauge transformations [3]. It describes the electron ( $e$ ), muon ( $\mu$ ), and tau ( $\tau$ ) leptons, all with spin 1/2 and electric charge -1, and their associated neutral, massless, spin-1/2 neutrinos  $\nu_e, \nu_\mu, \nu_\tau$ . They are arranged into  $SU(2)$  doublets of weak isospin  $(\nu_l, l)_L$  of left-handed states, and singlets  $l_R$  of right-handed states. Extending the SM to include massive neutrinos, as required by the observation of neutrino flavor oscillations, is discussed in Ref. [2]. The spin-1/2 quarks are similarly arranged into three “generations”:  $(u, d), (c, s), (t, b)$ , with electric charges  $(+2/3, 1/3)$ . They carry color charge, and their weak interactions take place among a set of states mixed by a rotation matrix. Quarks are not observed free, but rather as the elementary constituents of color-neutral composite hadrons. The interactions among particles are mediated by spin-1 bosons: eight electrically neutral, massless gluons (carrying color charges) mediate strong interactions; the neutral, massless photon  $\gamma$  mediates electromagnetism; and the massive  $W^\pm$  and  $Z^0$  mediate the weak interactions. Spontaneous breaking of the electroweak  $SU(2) \times U(1)$  symmetry gives masses to the  $W$  and  $Z$ , and further gives rise to the neutral, spin-0 Higgs particle  $H^0$ , with a positive vacuum expectation value. The SM contains 19 parameters [3], usually taken to be the three lepton masses, six quark masses, four parameters characterizing generational mixing among the quarks, three coupling strengths, the masses of the  $Z$  and  $H$ , and a coefficient allowing for the violation of combined charge-conjugation and parity-inversion symmetry in strong interactions. (The

description of neutrino mass requires additional parameters.) The success of the SM at predicting and interpreting experimental results is tremendous: all of the leptons, quarks, and gauge bosons have been observed, and interact according to the SM at length scales down to approximately  $10^{-18}$  m [3]. Despite its broad success, however, the SM remains incomplete: the nature of neutrino masses and their mixing is not yet determined; it is not known how to incorporate the observed dark matter (should it consist of particles), nor the effects of gravity, which are expected to become relevant at high energies. In addition, the mass of the scalar Higgs,  $m_H$ , is not predicted, and  $m_H^2$  receives contributions via virtual particle loops that depend quadratically on the momentum cut-off used, i.e. the scale at which new physics shall enter the calculation. Assuming that  $m_H$  is  $\mathcal{O}(100)$  GeV, as is required for  $WW$  scattering to remain perturbative, then either (a) new physics enters at the scale of  $\mathcal{O}(1 \text{ TeV})$ , or (b) some mechanism is required to remove this quadratic divergence, *e.g.* supersymmetry [4].

## 2.2 Supersymmetry

Supersymmetry is a theory of new physics that posits a new symmetry between bosons and fermions as an extension to the standard model. SUSY is appealing for several reasons. It allows for cancellation of quadratic divergences that appear in higher-order corrections to the calculation of the Higgs boson mass, because terms of opposite sign are contributed by the bosonic and fermionic superpartners. The lightest supersymmetric particle (LSP) in R-parity conserving models, described below, is usually neutral, massive, and weakly interacting, SUSY thus provides a candidate for dark matter. Finally, SUSY provides a mechanism whereby the coupling constants from the three standard model symmetry groups can be unified at a high scale, leading to the possibility of an even more fundamental theory, i.e., a grand unified theory (GUT) [5].

The theoretical underpinnings of SUSY rely upon a symmetry that relates bosons to fermions. In SUSY, the fundamental particle content of the universe will at least double, as all standard model particles will have a SUSY partner. The scalar superpartners of the fermions are called sfermions and have a spin 0. The fermionic superpartners of the bosons are called bosinos

and half-integer spins. The names of the individual particles can be constructed in a similar manner. SUSY can be realized in many ways and it is important to choose a model that is consistent and yet feasible to study. A completely unconstrained minimal parametrization of SUSY contains over 100 free parameters. It is necessary to reduce the number of free parameters in order to effectively test the predictions of the theory, so certain assumptions are made to construct a consistent model with fewer free parameters. As superpartners have not yet been observed, their masses must be higher than the corresponding standard model particles. This necessarily means that SUSY is a broken symmetry, and the unknown mechanism providing the SUSY breaking can determine the type of physics one can expect to observe. Some commonly studied models, such as mSUGRA (minimal Super GRAvity) and the cMSSM (constrained Minimal Supersymmetric Standard Model), posit that gravity is responsible for providing the SUSY breaking.

### 2.3 R-parity and a candidate for dark matter

R-parity, sometimes known as matter parity, is an additional symmetry (similar to the parity symmetry of the standard model) that determines the possible decays available in SUSY models. R-parity is defined in Equation 1, where  $B$  is the baryon number,  $L$  is the lepton number, and  $s$  is the spin of the particle in question. R-parity is a multiplicative quantum number, with  $R = 1$  for ordinary standard model particles and  $R = -1$  for SUSY sparticles.

$$R = (-1)^{3B+L+2s} \quad (1)$$

R-parity-conserving models are preferred due to consequences of R-parity violating (RPV) models, which allow for the decay of the proton, among other currently unobserved decays. While RPV models are not excluded, current theoretical prejudice favors R-parity conserving models. If R-parity is conserved, this necessarily implies that a sparticle must be produced in conjunction with another sparticle, i.e., sparticles will always pair produced at collider experiments. Another consequence is that the LSP must be stable. Additionally, if the LSP is



neutral, it will be noninteracting and thus a good candidate for cold dark matter. The neutral LSP is preferred in many models being explored at the LHC due to cosmological constraints on exotic matter [5].

## 2.4 Experimental signature

Color confinement in QCD prohibits the isolation of quarks [6] and as such, when a high energy quark is produced, e.g. from a collision of other particles, it quickly fragments into a color-neutral hadron. If the quarks in the hadron have enough energy, they fragment again into other hadrons. This hadronization process continues until the resulting particles are of low enough energy that it is no longer energetically favorable to fragment. The hadronic shower of particles can be clustered into objects called “jets”. A simulation of such a jet is shown in Figure 2.1.

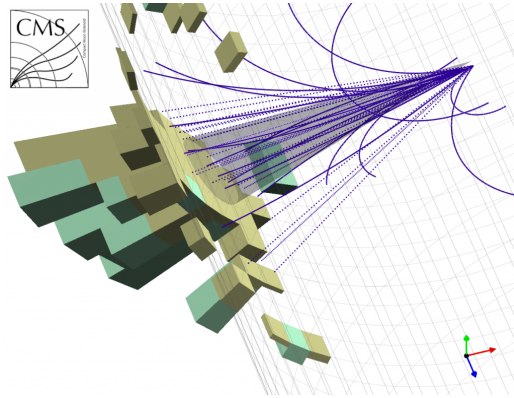


Figure 2.1: A simulation of a hadronized quark in the CMS detector. The resulting particles from hadronization are grouped into a jet (gray cone).

In this analysis, a search for excess in events consisting of jets and missing energy is conducted. This final state is expected when pairs of heavy squarks or gluinos are produced and decay hadronically to SM quarks, gluons, and neutralino, which escape the detector leaving only a signature of missing energy. The full unconstrained SUSY theory is parametrized by over 100 variables, representing masses, phases and mixing angles, but it can be simplified.

These simplified supersymmetric models (SMS) are limits of more general new-physics scenarios, where all but a few particles are integrated out [7]. The dominant contribution to the divergence of the Higgs boson mass arises from loop diagrams involving the top quark; these can be largely canceled if a scalar partner of the top quark (top squark) exists and has a mass below  $\sim 1$  TeV [7]. This relatively low mass is a motivation to interpret the results of this analysis in two decay channels of the direct pair-produced top squark. In the first channel, where the top squark decays to a top quark (followed by a semi-leptonic decay:  $t \rightarrow Wb \rightarrow l\nu b$ ), provides the highest reach in probing the mass of the top squark. The second decay scenario has only been recently pursued. It puts the mass difference between the top squark and the neutralino at 80 GeV or less, resulting in the top squark decaying directly into a charm quark. Figure 2.2 shows the schematic diagrams of these two decay channels. More detailed description of each model is left for Section 10

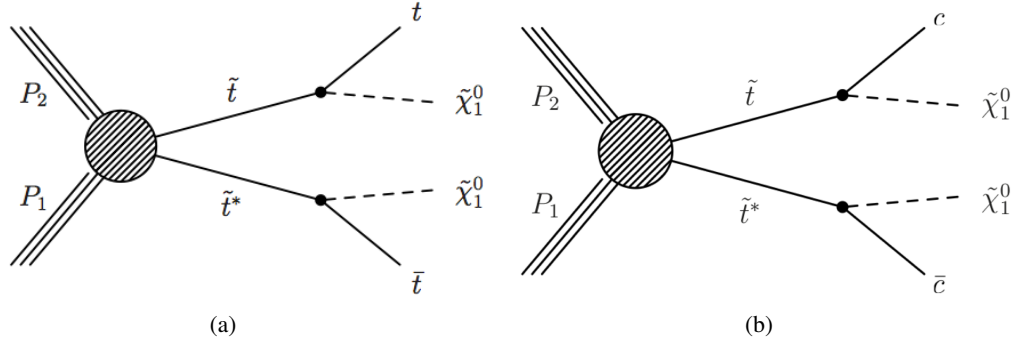


Figure 2.2: Two Feynman diagrams depicting the top squark production and decay, in which  $P$  represents a proton,  $t$  a top quark,  $c$  a charm quark,  $\tilde{t}$  a top squark,  $\tilde{\chi}_1^0$  a neutralino.

## 3 The Experiment

### 3.1 The Large Hadron Collider

The Large Hadron Collider (LHC) is a particle accelerator and collider housed 100 meters underground in a 27 km long circular tunnel situated beneath the Swiss-French border. The collider consists of two counter-circulating particle beams which are made to collide at four points along the ring. Figure 3.1 shows the location of the LHC and the four main detectors each housed at a different collision point.

The machine contains four straight long sections where acceleration, collimation, and beam dump systems are housed. The longer arc sections are in fact comprised of 1232 straight dipole magnets 15 meters in length designed to contain the particle beams in a circular path. Each section is held at a super-conductive temperature of 2 Kelvin which provides magnetic fields up to 8 Tesla that steer the beams. Higher order multi-pole magnets are placed near the interaction points to collimate and align the colliding beams. Unwanted beam interaction with residual gas in the beam pipes is minimized by vacuuming the beam pipes to pressures below  $10^{-10}$  mbar.

The protons are accelerated along straight sections of the ring where Radio-Frequency (RF) cavities generating electromagnetic fields are tuned to deliver protons a kick of energy at each revolution in the accelerator ring. Protons that are ideally timed and have exactly the desired energy, will feel a zero accelerating force from the RF cavity, while protons with slightly different energies that arrive earlier or later are decelerated or accelerated. As a result, the proton beams are divided in discrete “bunches” of protons. Each bunch, before collision, measures  $16 \mu\text{m}$  transversally and  $\sim 30$  cm long. Bunches are separated 7 m apart. The LHC has been designed to operate with 2808 bunches per beam, with about  $10^{11}$  protons per bunch. The figure of merit for colliders such as the LHC is the luminosity, a quantity influencing the rate of collisions. The instantaneous luminosity depends on the number of protons per beam, the transverse dimensions of the beams (the more the beams are squeezed, the higher the probability that a proton-proton collision takes place), and the bunch- crossing frequency. The number of events  $N$  of a certain process with cross section  $\sigma$  produced per second can be

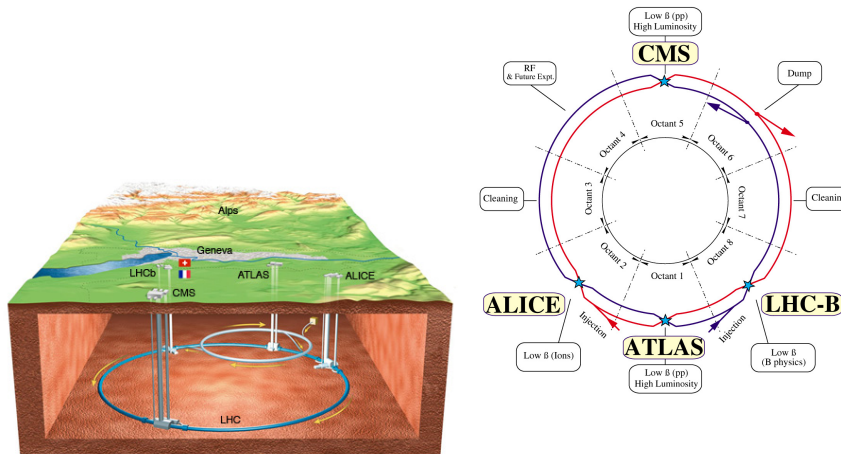


Figure 3.1: Left: a geographical map of the location of the LHC. Right: the layout of LHC.

expressed as

$$\frac{dN}{dt} = \mathcal{L} \times \sigma \quad (2)$$

The luminosity integrated over the course of the three separate proton-proton collision runs is shown in Figure 3.2. The large increases in delivered luminosity in such a short time indicates both the phenomenal success of LHC commissioning and running, and the challenge presented to CMS to accommodate new running conditions nearly continuously, in particular to design and deploy suitable trigger tables, readout thresholds, reconstruction algorithms, and analysis methods.

### 3.1.1 High energy proton collisions

The interactions sought and the SM processes that appear as backgrounds are those in which substantial momentum is transferred between the constituent partons of the LHC's colliding protons; the incident protons are destroyed and energetic outgoing elementary particles and proton remnants are produced. The distributions of what fraction of a proton's momentum a constituent gluon or quark carries are given by parton distribution functions (PDFs). For a

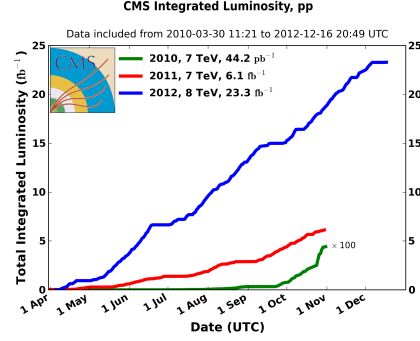


Figure 3.2: The luminosity integrated over the course of the three separate proton-proton collision runs as recorded by CMS. Note: the 2010 curve is multiplied by 100 for legibility.

particular production process, e.g.  $pp \rightarrow t\bar{t}$  or  $pp \rightarrow g\bar{g}$ , there are various parton scattering processes, e.g. from initial  $gg$  or  $q\bar{q}$ , which contribute; their cross sections are integrated over momentum fraction according to the PDFs and summed to obtain a total production cross section. Results of such cross section computations for a variety of processes are shown in Figure 3.3.

The potentially tiny rate of sparticle production compared with that of known processes presents a challenge for the search. In addition, given the total inelastic cross section of order 50 mb, the luminosity per colliding pair of bunches achieved at the LHC is sufficiently high that the expected number of interactions that occur in the same crossing as an interaction of interest is non-negligible. For the data used in this search, the mean number of such pile-up interactions is approximately 20. Quarks or gluons which emerge from a hard-scattering process fragment and eventually group into hadrons before observation in a detector. They are visible as energetic sprays of hadrons called jets, which typically leave tracks in the inner detector and deposit energy in the calorimeters. The center-of-mass of the scattering system has a boost along the beam-line which varies event-by-event. It is therefore convenient to discuss jets (as well as other reconstructed particles) in terms of these quantities: transverse momentum  $p_T$ , which is invariant under such boosts, or similarly transverse energy  $\equiv E \sin(\theta)$ , with  $0 \leq \theta \leq \pi$  where  $\theta$  is the polar angle from the beam-line; and pseudo-rapidity  $\eta \equiv \ln(\tan(\theta/2))$ , of which differences are (approximately) invariant.

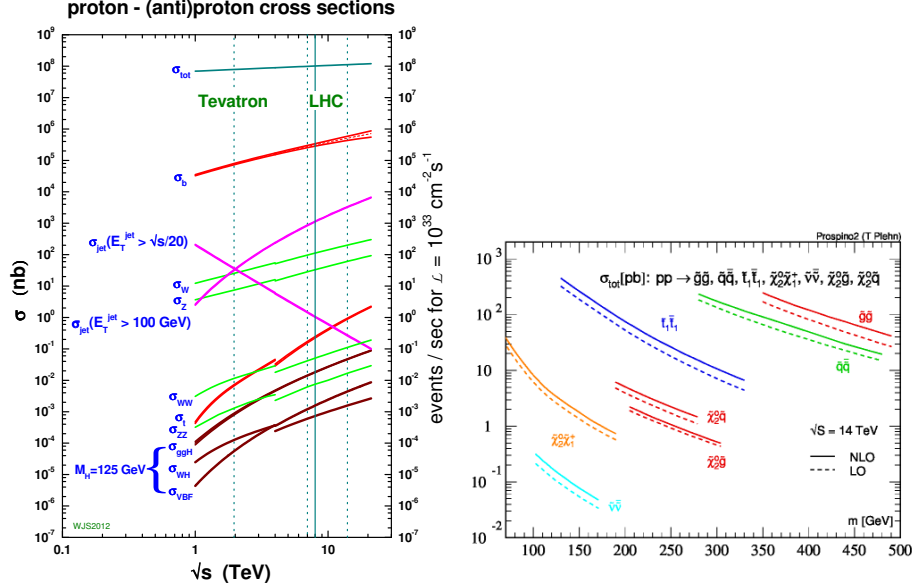


Figure 3.3: Left: the cross sections (in nb) of various SM processes vs. center-of-mass energy in  $pp$  collisions when  $\sqrt{s} > 1 \text{ TeV}$ , from Ref. [8]. Right: The cross sections (in pb) of various SUSY processes vs. sparticle for  $pp$  collisions at  $\sqrt{s} = 14 \text{ TeV}$ . From Ref. [9].

## 3.2 The Compact Muon Solenoid detector

### 3.2.1 The detector

The Compact Muon Solenoid (CMS) detector is designed to provide efficient identification and measurement of photons, electrons, muons, taus, and hadronic showers over wide ranges of transverse momentum and direction, and its nearly  $4\pi$  coverage in solid angle provides accurate measurement of global transverse momentum imbalance. It has sufficient granularity to perform these measurements even when 20+ interactions occur simultaneously in a collision of two bunches of protons, and fast enough response to do so when the time between beam crossings is 25 ns. Its components are resistant to damage from radiation, enabling its use to collect substantial luminosity, and its modularity allows for long-term maintenance and upgrades. When closed, CMS is a cylinder of length 22 m, diameter 15 m, and mass 12,500 tons. It is described in detail elsewhere [10].

The last name of the detector refers to a superconducting solenoid of radius 3 m and length 12.5 m, which carries 18 kA to provide a longitudinal magnetic field of 3.8 T. It is operated at 4.5 K. This magnet is surrounded by a central fixed “ring” and two movable rings on each side, constituting the “barrel”; it is flanked on each side by an “endcap”. The tracking system and calorimeters reside in the magnet bore. The layout is shown in the bottom plot of Figure 3.4. The x-axis is taken to point radially toward the center of the LHC ring, the y-axis to point against gravity, and the z-axis to form a right-handed coordinate system.

CMS is divided into “subdetector” systems, which perform complementary roles. The inner-most subdetector of the barrel consists of three layers of silicon pixel sensors that provide three-dimensional positions of the hit from charged tracks between 4 cm and 10 cm transverse to the beams. They are complemented by two endcap disks, enabling charged particles to leave typically three hits for pseudo-rapidity  $|\eta| < 2.5$ . Surrounding the pixel detector are ten layers of strips of silicon sensors out to 1.1 m, four of which have additional strips at a small stereo angle, allowing another dimension of hit position measurement. These are complemented by endcap disks as well. This tracking system provides efficient and precise determination of the charges, momenta, and impact parameters of charged particles. Surrounding the tracker is an electromagnetic calorimeter (ECAL), consisting of scintillating  $\text{PbWO}_4$  crystals of area  $0.017 \times 0.017$  in  $\Delta\eta \times \Delta\phi$  and length 23 cm, corresponding to about 25 radiation lengths. The crystals are instrumented with avalanche photo-diodes in the barrel ( $|\eta| < 1.479$ ) and vacuum photo-triodes in the endcap ( $1.479 < |\eta| < 3.0$ ). A lead-silicon sampling “pre-shower” detector is placed before the endcap to aid with the identification of neutral pions.

The hadron calorimeter (HCAL) consists of alternating layers of brass absorber and plastic scintillator, which sample hadronic showers, arranged in identical azimuthal units into two half-barrels and also into two endcaps. The scintillators are segmented projectively into towers of area  $\Delta\eta \times \Delta\phi = 0.087 \times 0.087$  for  $|\eta| < 1.6$ , and approximately  $0.17 \times 0.17$  for  $|\eta| > 1.6$ . The light produced in the scintillator layers is merged, wavelength-shifted and carried to the photo-cathode of a hybrid photo-diode (HPD). The single stage HPD accelerates the liberated electrons using a  $\sim 7$  kV potential difference, which then impinge on a silicon diode. The current produced is amplified, digitized, and transmitted via optical links to dedicated boards.

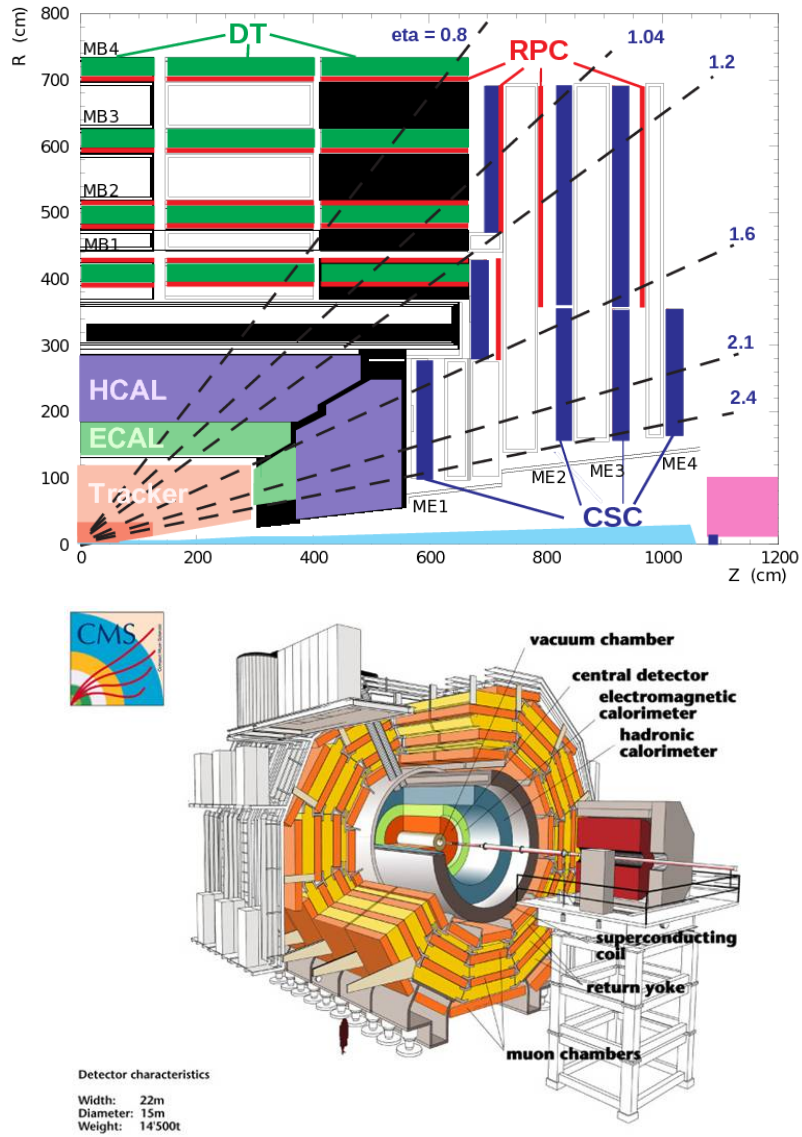


Figure 3.4: Top: a view of one quadrant of CMS. The volume enclosing the tracker is shown in light red, the electromagnetic calorimeter in light green, the hadron calorimeter in lavender, and the forward calorimeter in magenta. The muon detectors are labeled, from Ref. [11], Bottom: a perspective view of CMS from Ref. [10].

Coarse data, summed over longitudinal segments (which are present for  $|\eta| > 1.2$ ) and time, are transmitted after peak-finding to the calorimeter trigger system. The full data, after the suppression of low energy hits to reduce data volume, are sent to the data acquisition system



(DAQ).

Outside of the endcaps are forward calorimeters (HF) of steel absorber and quartz fibers, in which relativistic particles produce Cherenkov light. They cover the region  $3.0 < |\eta| < 5.0$ , thereby improving the hermeticity of CMS. Their hit-occupancy is histogrammed at 40 MHz to track the delivered luminosity, and the instantaneous luminosity computed from the histograms is reported each “luminosity section”, i.e. 218 beam orbits or approximately 23 seconds. The luminosity measurement is calibrated by scanning the transverse positions of the beams relative to each other to measure their effective overlap [12].

The magnets flux-return yoke and the endcaps are instrumented with muon detection systems, as shown in the top plot of Figure 3.4. The drift tube (DT), cathode strip chamber (CSC), and resistive plate chamber (RPC) systems provide efficient detection of muons with pseudo-rapidity  $|\eta| < 2.4$ . Further, they provide a muon trigger.

The CMS trigger system consists of two parts: “Level One” (L1), and “High Level” (HLT). The L1 is a set of electronics operating at 40 MHz, corresponding to the smallest achievable spacing between bunches in LHC, and has a latency of  $3 \mu\text{s}$ . In particular, in the trigger algorithms used in this work, coarse “trigger primitive” data from the electromagnetic and hadron calorimeters are streamed from the respective detectors. Neighboring projective towers are summed into regional transverse energies, from which electron/photon and jet candidate deposits are determined. If, in a particular time slice, at least one electron/photon candidate above a transverse energy threshold is found, or alternatively the sum of the transverse energies of the found jets exceeds a threshold, then a “Level One Accept” (L1A) signal is sent to the readout electronics of all subdetectors.

Upon receiving an L1A, approximately 600 boards transmit their event fragments via an optical network to a computer farm with approximately 1000 nodes, which subsequently builds the events. The L1A rate is limited (by design) to 100 kHz, which at a luminosity of  $2 \times 10^{33} \text{ cm}^{-2} \text{ s}^{-1}$  provides a rejection factor of approximately 200 for collisions within CMS. An additional 100 Hz of rate is used for a calibration sequence, in which subdetector channels are illuminated by laser and LED to measure drifts in transparency and gain.

The HLT processes events with software reconstruction sequences that approximate the

offline reconstruction as closely as possible, given the constraint on mean processing time of approximately 50 ms. The HLT provides a rejection factor of approximately 500 in order to achieve an event rate to disk of a few hundred per second. The recorded events are transferred from CMS to the CERN computing center, where event reconstruction is performed, and then distributed to CMS computing sites around the globe for storage and analysis. During the 2012 run, nearly all components of CMS have performed according to design specifications. Most subdetectors have a stable fraction of functional channels between 97% and 99%, and the data-taking efficiency (by luminosity) is approximately 90%.

### 3.2.2 Event reconstruction

The goal of event reconstruction is to take the raw information recorded by the detector and to compute from it higher-level quantities which correspond roughly to properties of (a) individual particles, e.g. charge, momentum, or energy; (b) groups of particles produced in a shower, e.g. multiplicity or geometric prole; (c) the global event, e.g. total energy recorded, or degree of momentum balance. Many aspects of the reconstruction sequence are described in detail in Ref. [13, 14]. Below is a brief description of those most relevant to this search.

The raw data read out from CMS are first converted to software representations of the digital samples of the detector signals, which are associated with individual detector elements. In a typical procedure, knowledge of pulse shapes, time-dependent channel-by-channel baseline values and gains, and detector geometry is then used to convert these samples into reconstructed “hits”, i.e. energy deposits in particular detector locations at particular times.

The reconstruction of particle tracks in the inner detectors proceeds in several steps: (a) seeds are determined from hits in the pixels layers; (b) approximate tracks are propagated outward, gathering matching hits and becoming more precise; (c) for each track a final fit is performed using all of its hits. Primary vertices are found by grouping tracks based on the z-coordinates of their points of closest approach to the beam-line, and for each cluster of tracks a fit is performed to determine the position of the vertex.

To identify and reconstruct muons, a trajectory is first determined using only the informa-

tion from muon systems; then, if a matching track in the inner detector is found, a fit to the hits in both detectors is performed to determine the parameters of the muon trajectory. Such a muon is referred to as a global muon. This and other approaches are described in Ref. [15].

To reconstruct photons and electrons, hits in the ECAL are first clustered in rectangular strips of 5 crystals in  $\eta$  by 35 in  $\phi$  (in the barrel), or one or more group of 5 by 5 crystals (in the endcaps) about energetic seed hits. Such a cluster contains nearly all of the energy in an electromagnetic shower, and serves already as a basic photon candidate. To reconstruct electrons, a trajectory from the measured cluster position is propagated inward to the pixel layers. If matching hits are found, they are used as a seed to build the electron track with a model that includes energy loss via radiation; the track and cluster are then used in tandem.

Jets are reconstructed using the anti-kt algorithm [16] with size parameter  $R = 0.5$ . Input to the algorithm is the set of projective calorimeter towers with total deposited energy greater than approximately 1 GeV, which are treated as massless and with directions chosen to connect the tower center to the nominal interaction point. The raw jet energies are corrected to achieve a uniform relative response as a function of pseudo-rapidity, in particular to compensate for detector non-uniformities, and a calibrated absolute response as a function of transverse momentum [17]. The relative  $p_T$  resolution for central jets, determined using dijet  $p_T$ -asymmetry, is shown in Figure 3.5.

Missing transverse energy ( $\cancel{E}_T$ ) is computed from the same towers of energy deposits in the calorimeters that are used for jet-finding; it is the negative of the vectorial sum of their components transverse to the beam-axis. Corrections are applied to accommodate the jet energy corrections and the presence of muons [18].

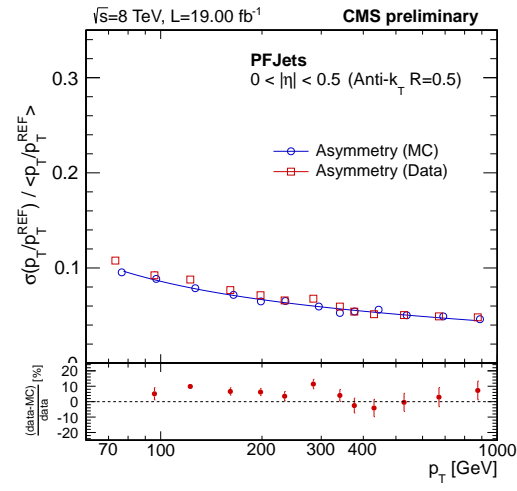


Figure 3.5: The relative  $p_T$  resolution as a function of jet  $p_T$  for central jets.

## 4 Data sets and simulated samples

### 4.1 Data sets

The following datasets are used to populate the hadronic and control samples. They correspond to the full data run of 2012 and an integrated luminosity of  $19.45 \pm 0.8 \text{ fb}^{-1}$ . Only certified luminosity sections that pass good data quality criteria are used for data taken in the run range 190456–208686.

Table 1: Datasets.

Dataset	Luminosity ( $\text{fb}^{-1}$ )
Hadronic	19.45
Muon	19.72
Photon	19.63

### 4.2 Simulated samples for SM backgrounds

The SM background Monte Carlo samples for physics at 8 TeV are taken from the Summer12 simulation production run with reconstruction software version CMSSW\_5\_3\_X with the PU\_S10 scenario. The effective luminosity of each MC sample is normalized to the integrated luminosity of the corresponding dataset, as listed in Table 2. All MC samples are reweighted on an event-by-event basis such that the distribution of pile-up (PU) interactions matches that observed in data [19].

### 4.3 Corrections to cross sections for SM samples

Every simulated event is weighted by the total number of events in the MC sample, the theoretical cross section, and total luminosity of the data being studied. Theoretical calculations are available that provide next-to-next-to leading order (NNLO) cross sections for each inclusive

Table 2: MC samples for Standard Model processes.

Sample	HT (GeV)	Cross section (pb)	Corrected Cross section (pb)
$W \rightarrow l\nu$	Inclusive	37509.0	34133.2
$W \rightarrow l\nu$	150 - 200	253.8	234.53
$W \rightarrow l\nu$	200 - 250	116.5	103.94
$W \rightarrow l\nu$	250 - 300	57.6	51.34
$W \rightarrow l\nu$	300 - 400	48.4	42.41
$W \rightarrow l\nu$	400 - $\infty$	30.8	26.36
$Z \rightarrow \nu\bar{\nu}$	50 - 100	452.8	405.21
$Z \rightarrow \nu\bar{\nu}$	100 - 200	190.4	173.76
$Z \rightarrow \nu\bar{\nu}$	200 - 400	45.1	42.41
$Z \rightarrow \nu\bar{\nu}$	400 - $\infty$	6.26	5.81
$t\bar{t}$	Inclusive	234.0	271.44
$Z/\gamma^* \rightarrow l^+l^- (m_{ll} > 50)$	Inclusive	3503.7	3258.45
$Z/\gamma^* \rightarrow l^+l^- (10 < m_{ll} < 50)$	Inclusive	13124.1	12205.4
$Z/\gamma^* \rightarrow l^+l^-$	200 - 400	24.3	22.24
$Z/\gamma^* \rightarrow l^+l^-$	400 - $\infty$	3.36	3.11
$\gamma + \text{jets}$	200 - 400	1140.8	1060.9
$\gamma + \text{jets}$	400 - $\infty$	124.7	115.97
WW	Inclusive	57.1	57.1
WZ	Inclusive	12.6	12.6
ZZ	Inclusive	8.26	8.26
t (t-channel)	Inclusive	56.4	56.4
$\bar{t}$ (t-channel)	Inclusive	30.7	30.7
t (s-channel)	Inclusive	3.79	3.79
$\bar{t}$ (s-channel)	Inclusive	1.76	1.76
t (tW-channel)	Inclusive	11.1	11.1
$\bar{t}$ (tW-channel)	Inclusive	11.1	11.1

SM sample [20]. In an attempt to provide higher statistics in tails of distribution analyses often cut on (ie  $H_T^{\text{parton}}$ ,  $N^{\text{parton}}$ ,  $\hat{p}_T$ ), MC samples are produced binned in these variables. Only the leading-order (LO) cross sections are provided [21], but in general, the  $k$ -factors required to go from LO to NNLO cross sections are determined using corresponding inclusive samples and applied to each binned sample.

Studies conducted by other analyses [22] revealed that some LO cross sections calculated for MC samples binned according to  $H_T^{\text{parton}}$  are inaccurate to a level as large as 10%, leading to non-physical discontinuities in the  $H_T^{\text{parton}}$  distribution constructed from the binned samples of a given process. Furthermore, due to an error in production, the  $W \rightarrow l\nu$   $H_T$  binned samples exhibit  $H_T$ -dependent biases. The following paragraphs describe a procedure to measure corrections to the discontinuities and biases of the  $W \rightarrow l\nu$   $H_T^{\text{parton}}$  binned samples as a function of  $H_T$ . Other analyses created similar procedures to correct the  $Z \rightarrow \mu\mu$   $H_T^{\text{parton}}$  binned samples, this analysis uses those measured corrections as  $k$ -factors.

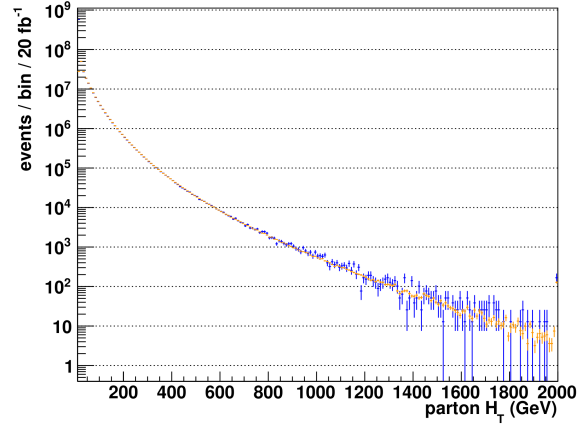
As a first step, we wish to reweigh the cross sections of the  $H_T^{\text{parton}}$  binned samples such

that their  $H_T^{\text{parton}}$  distributions match that of the inclusive sample's. Due to the inclusive sample's limited statistics in the tails of  $H_T$  distribution, we instead use the  $N^{\text{parton}}$  binned's  $H_T^{\text{parton}}$  distribution which is verified to agree well with the inclusive sample Figure 4.1 (a). Additionally, to smooth statistical fluctuations, both distributions are fitted using a double exponential of the form  $\exp(a + b * x + c * x^{1.05})$  for  $H_T > 500$  GeV, Figure 4.1 (b). The ratio of the distributions Figure 4.1(c) is applied as  $H_T^{\text{parton}}$  dependent event weight.

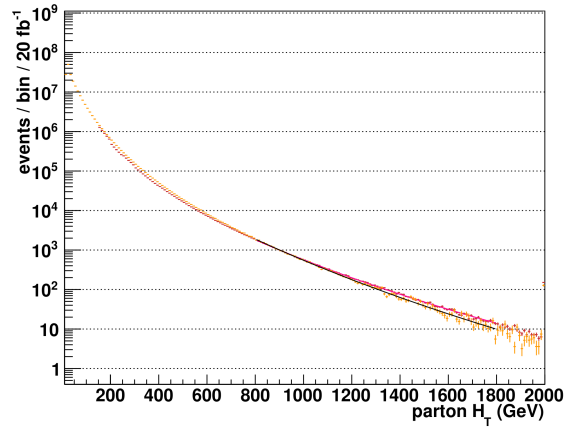
In the high- $H_T$  and high- $\cancel{E}_T$  corner of kinematic phase space of this analysis (and other SUSY analyses) the overall normalization of MC samples does not agree well with data. Therefore a data sideband in  $H_T$  is used to determine sample-specific corrections that are appropriate for the  $H_T$ - $\cancel{E}_T$  phase space covered by this analysis. This correction is determined for the  $W \rightarrow l\nu$  and  $t\bar{t}$  samples by imposing requirements on the number of muons, jets, and b-tagged jets, to obtain samples rich in  $W$  + jets, and  $t\bar{t}$  events. A sideband in  $H_T$  is used to determine both the yields in data and MC expectations. The sideband is defined by the bin  $200 < H_T < 225$  GeV and uses the jet  $p_T$  thresholds (73, 73, 37 GeV) to maintain comparable jet multiplicities, kinematics, and background admixtures as observed for the higher  $H_T$  bins. Trigger efficiency and b-tag scale factor corrections are determined and applied to the MC samples. The purity of the samples is  $> 80\%$  and any contamination is taken into account. The correction is determined by taking the ratio of the data yield over the MC expectation in the sideband. Table 3 summarizes the selection and corrections for the different samples.

Table 3: Corrections determined from a data sideband for the  $W$  + jets and  $t\bar{t}$  samples. “Corrected yield” reflects the observed data yield minus the contamination as given by MC.

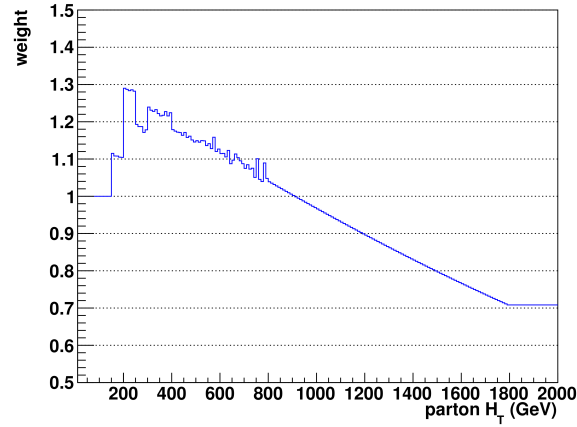
Process	Selection	Purity	Corrected yield	MC expectation	Correction Factor
$W$ + jets	$\mu$ + jets, $2 \leq n_{\text{jet}} \leq 3$ , $n_b = 0$	0.90	15682	$18013.1 \pm 85.9$	$0.87 \pm 0.01$
$t\bar{t}$	$\mu$ + jets, $n_{\text{jet}} \geq 2$ , $n_b \geq 2$	0.83	752	$736.7 \pm 11.5$	$1.02 \pm 0.05$



(a) Parton  $H_T$  distribution for the  $W \rightarrow l\nu$  inclusive sample (blue) and  $W \rightarrow l\nu N^{\text{parton}}$  binned sample (orange.)



(b) Fitted Parton  $H_T$  distribution for the  $W \rightarrow l\nu H_T^{\text{parton}}$  sample (red) and  $W \rightarrow l\nu N^{\text{parton}}$  binned sample (orange.)



(c) Event weight determined from ratio of Figure 4.1 (b)

Figure 4.1: Generator-level  $H_T^{\text{parton}}$  distributions and measured weights



## 5 Event Selection

As discussed in Section 2.2, all-hadronic SUSY signatures consist of events with no isolated objects apart from energetic jets. One can quantify the total visible energy in these type of events with the quantity,  $H_T$ , defined as the scalar sum of the transverse energy of the jets in the event. The challenges due to large backgrounds in a search for an excess in all-hadronic events becomes evident when comparing observed data events overlaid with simulated events from SM processes as a function of  $H_T$ , as shown in Figure 5.1.

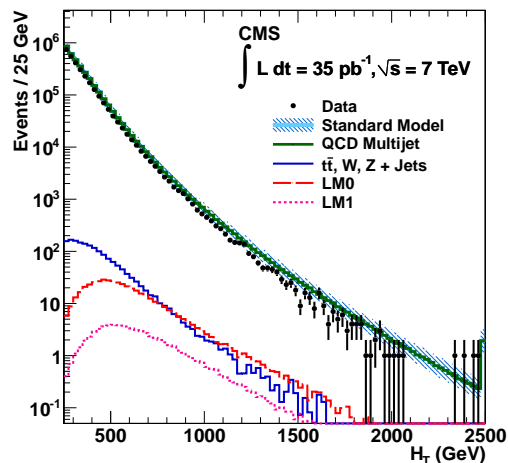


Figure 5.1:  $H_T$  distribution after basic preselection, for  $35 \text{ pb}^{-1}$  of data collected at 7 TeV as well as for all SM backgrounds and two SUSY signal samples, from Ref. [23]. This figure is for illustrative purposes only, as these specific SUSY models are not under study in this analysis.

The dominant background consist of azimuthally-balanced (i.e, back-to-back in the azimuthal angle  $\phi$ ) multijet events, stemming from QCD processes. This search reduces this background to negligible levels in the hadronic search region by employing the  $\alpha_T$  variable further discussed in Section 5.7. Furthermore, by construction,  $\alpha_T$  also reduces backgrounds from mis-measured back-to-back jets. The remaining significant backgrounds are SM process with genuine  $\cancel{E}_T$ . The expected yield of these backgrounds are measured using two control

samples. The following sections describe the identification of objects used in the hadronic and control samples, while the detailed description of the background and control samples are left for Section 6.

## 5.1 Data

The data analyzed was recorded by CMS in 2012 between April 5th and December 5th and amounts to  $19.47 \pm 0.5 \text{ fb}^{-1}$  at the center of mass energy of  $\sqrt{s} = 8 \text{ TeV}$ . The collected data is certified on a run-by-run basis, where initial automatic certification requires the LHC beams to be declared stable and all CMS subdetectors ON. Further monitoring of the data was done in real-time by experts of each subdetector through analysis of histograms updated and filled each luminosity section. Final certification was done offline, and only luminosity sections passing all criteria for good quality are used in this analysis.

## 5.2 Event quality

Each event is subjected to a series of commonly used filters in CMS to ensure good data quality. Minimal requirements are that at least one primary vertex is identified and 25% of the reconstructed tracks to be of good quality. Additionally, various event cleaning filters prescribed by the MET group [24] are applied. These filters reject events containing known problems, such as: muons with inconsistent energy or muons created by beam-gas interactions, spurious noise spikes in the calorimeter, tracking failures, and calibration laser events overlapping with physics collisions.

## 5.3 Physics objects

The following subsections describe the definitions of the physics objects used in this analysis.

### 5.3.1 Jets

Jets are reconstructed by combining information from multiple sub-detectors using the Particle-Flow (PF) algorithm [25] and clustered by the anti- $k_T$  algorithm [16] with a size parameter of 0.5. Three levels of jet energy corrections are applied; level 1 corrects for overlapping pp collisions (pile-up [26, 27]) in the jet, level 2 and 3 correct the jet energy response to be  $\eta$  and  $p_T$  independent. Further residual corrections are applied on data which correct for small remaining discrepancies in the modeling of the response. The acceptance of “fake” and poorly reconstructed jets is suppressed by selecting jets that pass jet identification at the Loose working point [28]. This requires that the jet is comprised of more than one particle and that those particles cannot all be neutral hadrons or all neutral particle deposits in the ECAL. Additionally if the jet is reconstructed beyond the tracker’s instrumentation, i.e.  $|\eta| < 2.4$ , the jet is required to have more than one charged constituent, of which not all of them deposit their energy in the ECAL. Only jets reconstructed within the barrel and endcap of the calorimeters, i.e.  $|\eta| < 3.0$ , and with transverse momentum  $p_T > 50$  GeV are considered in the analysis. Jets originating from bottom quarks (b-jets) are identified through vertices that are displaced with respect to the primary interaction [29]. The algorithm used to tag b-jets is the Combined Secondary Vertex tagger, using the “Medium” working point, which is achieved by requiring a cut of  $>0.679$  on the algorithm discriminator variable and results in a gluon/light-quark quark mis-tag rate of 1% (where “light” means  $u$ ,  $d$  and  $s$  quarks) and an efficiency in the range 60 – 70% depending on the jet  $p_T$ .

### 5.3.2 Muons

Muons are identified according to the Tight working point definition ( $\sim 95\%$  efficiency) of the muon identification algorithm [30]. The algorithm works to reject cosmic muons or muons from decays in flight for consideration in the analysis. A PF-based “combined relative” isolation [30] is determined within a cone size  $\Delta R < 0.4$ , and corrections are applied to remove the effects of pileup. Table 4 summarizes the identification and isolation requirements.

Table 4: Muon identification (Tight working point).

Global Muon	True
PFMuon	True
$\chi^2$ fit	$< 10$
Muon chamber hits	$> 0$
Muon station hits	$> 1$
Transverse impact $d_{xy}$	$< 0.2$ mm
Longitudinal dist $d_z$	$< 0.5$ mm
Pixel hits	$> 0$
Track layer hits	$> 5$
PF Isolation ( $\Delta\beta$ corrected)	$< 0.12$

### 5.3.3 Photons

Photon candidates must satisfy the Tight working point definition ( $\sim 70\%$  efficiency) of the simple cut-based photon identification algorithm [31]. The ECAL energy deposits from electrons are checked to have come from a converted photon. The ratio of energy deposits between HCAL and ECAL for a solid cone of size  $\Delta R = 0.15$  is required to be  $H/E < 5\%$ . A maximum is set on the width of the clustered energy deposit,  $\sigma_{i\eta i\eta}$ , as decay photons from neutral pions typically have larger widths. Pile-up corrected isolation is determined within a cone of size  $\Delta R < 0.3$  using the PF-based isolation algorithm [31]. Table 5 summarizes the identification and isolation requirements.

Table 5: Photon identification (Tight working point).

Categories	Barrel	EndCap
Conversion safe electron veto	Yes	Yes
Single Tower H/E	0.05	0.05
$\sigma_{i\eta i\eta}$	0.11	0.31
PF charged hadron isolation	0.70	0.50
PF neutral hadron isolation	$0.4 + 0.04 \times p_T^\gamma$	$1.5 + 0.04 \times p_T^\gamma$
PF photon isolation	$0.5 + 0.005 \times p_T^\gamma$	$1.0 + 0.005 \times p_T^\gamma$

### 5.3.4 Electrons

Electrons are identified according to the “Veto” working point definition ( $\sim 95\%$  efficiency) of the cut-based Egamma identification algorithm [32]. PF-based isolation [33] is determined within a cone size  $\Delta R < 0.3$  and corrections are applied to remove the effects of pileup. Table 6 summarizes the identification and isolation requirements.

Table 6: Electron identification (Veto working point).

Categories	Barrel	EndCap
$\Delta\eta_{In}$	0.007	0.009
$\Delta\phi_{In}$	0.15	0.10
$\sigma_{i\eta i\eta}$	0.01	0.03
H/E	0.12	0.10
$d_0$ (vtx)	0.02	0.02
$d_Z$ (vtx)	0.2	0.20
$ (1/E_{\text{ECAL}} - 1/p_{\text{trk}}) $	0.05	0.05
PF relative isolation	0.15	0.15

### 5.3.5 Missing transverse energy

Missing transverse energy ( $\cancel{E}_T$ ) is computed from the same towers of energy deposits in the calorimeters that are used for jet-finding; it is the negative of the vectorial sum of their components transverse to the beam-axis. The analysis uses the particle-flow MET algorithm [34] with jet energy corrections applied. As discussed further in Section 5.7, the  $\cancel{E}_T$  variable is only used in the following two cases: to define the transverse mass variable,  $M_T$ , which is in turn used as part of the selection criteria that define the  $\mu + \text{jets}$  control sample, described in Section 6.2; and to define a cleaning filter applied after the  $\alpha_T$  requirement, as described in Section 5.8.

### 5.3.6 Single isolated tracks

A single isolated track (SIT) [35] can be used to identify W bosons through their leptonic decays. A single isolated track is identified if a charged PF object has at least a  $p_T$  of 10 GeV, is near the primary vertex ( $\Delta z(\text{track}, \text{PV}) < 0.05$  cm) and has a relative track isolation of  $< 0.1$ . This object can be used to help suppress the “lost lepton” background from W and  $t\bar{t}$ , as described in section 5.5.

## 5.4 Triggers

### 5.4.1 Hadronic search region and control samples

Only events passing one or more HLT triggers based on online quantities are recorded to be analyzed. In any analysis, it is generally not expected that all recorded events reconstructed offline pass the online trigger as detector conditions, energy corrections, and object-based quantities differ offline. In this analysis, triggers at the HLT based on quantities  $H_T$  and  $\alpha_T$  (labeled as HTxxx\_AlphaT0pyy) are used with various thresholds to record candidate events for the hadronic search region. In order to keep the computational time low, the online quantities are constructed using calorimeter based jets (calo jets). Additionally, the use of particle-flow jets in this analysis is expected to introduce inefficiencies. Each  $H_T$  bin is seeded by a single trigger chosen based on the efficiency of the trigger in that  $H_T$  bin. The  $\alpha_T$  thresholds of the HTxxx\_AlphaT0pyy triggers were tuned according to the threshold on the  $H_T$  leg in order to fully suppress QCD multijet events [36] and simultaneously satisfying other criteria, such as maintaining acceptable trigger rates.

The HTxxx\_AlphaT0pyy trigger efficiencies are measured with a reference (i.e., unbiased) event sample recorded by an unprescaled, loosely-isolated, eta-restricted single muon trigger, HLT\_IsoMu24\_eta2p1, within the SingleMu dataset. This sample contains events with at least one isolated muon with  $p_T > 25$  GeV and  $|\eta| < 2.1$  (similar to the  $\mu + \text{jets}$  control sample defined in Section 6.2). Muons are required to be isolated: a cut of  $\Delta R > 0.5$  is placed between all muons and jets in each event, and only jets are considered in the calculation of  $H_T$ ,

and  $\alpha_T$ , i.e. the muon is ignored.

Table 7: List of signal triggers and their efficiencies (%), as measured in the SingleMu data. The trigger efficiency is  $\sim 100\%$  for all bins above  $H_T > 675$  GeV.

Offline $H_T$	Offline $\alpha_T$	L1 seed (L1)	Trigger (HLT)	Efficiency (%)	
bin (GeV)	threshold	(highest thresholds)		$2 \leq n_{\text{jet}} \leq 3$	$n_{\text{jet}} \geq 4$
$375 < H_T < 475$	0.55	DoubleJetC64 OR HTT175	HT300_AlphaT0p53	$94.2^{+0.5}_{-0.6}$	$90.5^{+1.2}_{-1.3}$
$475 < H_T < 575$	0.55	DoubleJetC64 OR HTT175	HT350_AlphaT0p52	$96.2^{+0.8}_{-0.9}$	$94.6^{+1.2}_{-1.4}$
$575 < H_T < 675$	0.55	DoubleJetC64 OR HTT175	HT400_AlphaT0p51	$95.4^{+1.4}_{-1.8}$	$98.7^{+0.7}_{-1.12}$
$H_T > 675$	0.55	DoubleJetC64 OR HTT175	HT400_AlphaT0p51	$100^{+0.0}_{-2.0}$	$100^{+0.0}_{-2.0}$

Table 7 summarizes the measured efficiencies for the HTxxx\_AlphaT0pyy triggers in the relevant  $H_T$  bins. The trigger efficiencies are measured for both  $n_{\text{jet}}$  multiplicity bins. The efficiencies are slightly lower in the higher jet multiplicity category due to a larger number of jets summing to the same  $H_T$ , resulting in softer jets. Figure 5.2 shows the efficiency curves for the HTxxx\_AlphaT0pyy triggers in the three lowest  $H_T$  bins, for the  $2 \leq n_{\text{jet}} \leq 3$  and  $n_{\text{jet}} \geq 4$  categories.

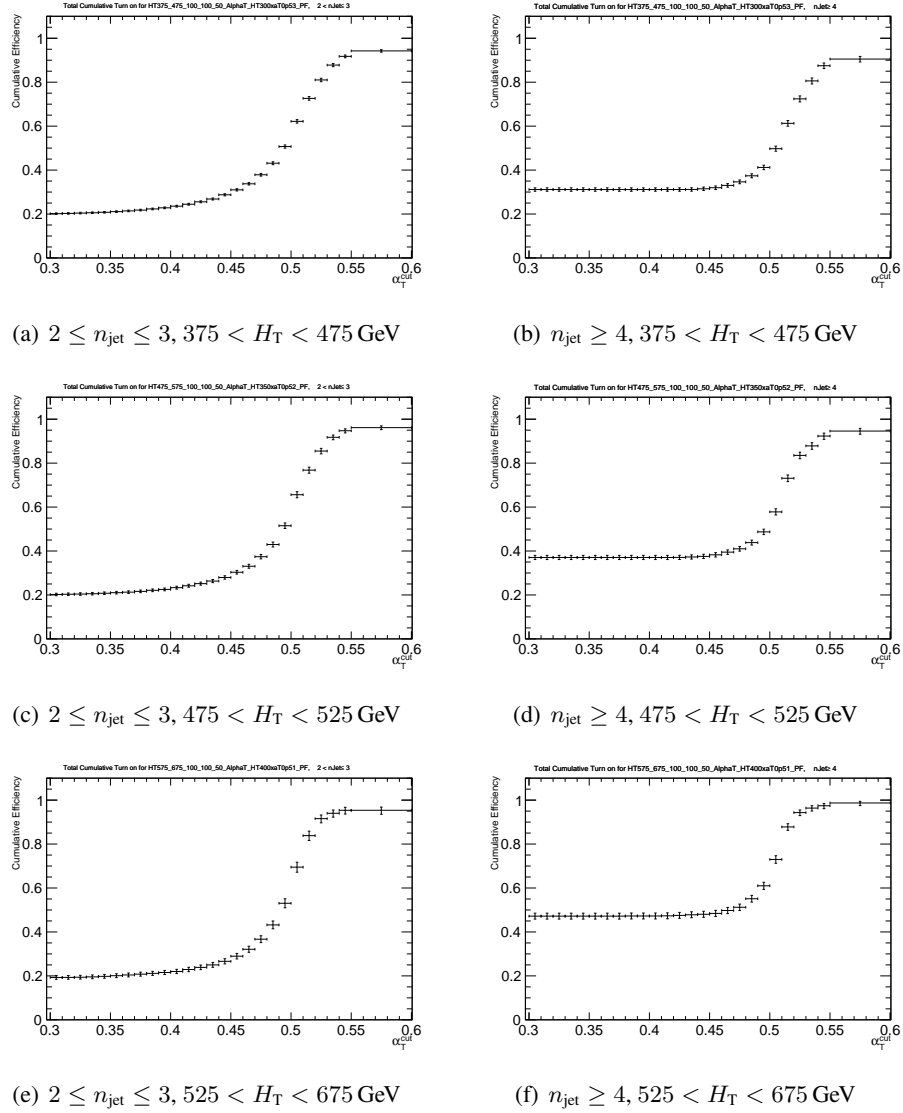


Figure 5.2: Cumulative efficiency turn-on curves for the  $H_T$ - $\alpha_T$  cross triggers (as summarized in Table 7) that record events for the three lowest  $H_T$  bins for events satisfying  $2 \leq n_{\text{jet}} \leq 3$  (left) and  $n_{\text{jet}} \geq 4$  (right).

## 5.5 Object vetoes

The background in this search can be separated into two types: reducible and irreducible.

The latter refers to backgrounds that have the same final state as the signal and therefore any



cut imposed to reduce the background processes would also reduce the signal. The process  $Z \rightarrow \nu\bar{\nu} + \text{jets}$  is the only irreducible background in this search. All other backgrounds are reducible, meaning that if no information in the event is lost and all cuts were fully efficient, the background could be eliminated without loss of signal. To suppress  $W + \text{jets}$  and  $t\bar{t}$  events, this analysis uses vetoes object to reject events where a  $W$  boson decays to a neutrino and a lepton. Events containing an isolated electron (Sec. 5.3.4) with  $p_T > 20 \text{ GeV}$  and  $|\eta| < 2.5$  or an isolated muon (Sec. 5.3.2) with  $p_T > 10 \text{ GeV}$  and  $|\eta| < 2.5$  are vetoed. In order to keep this search all-hadronic and not overlap with other analyses in CMS [38, 39], events with isolated photons (Sec. 5.3.3) with  $p_T > 25 \text{ GeV}$  and  $|\eta| < 2.5$  are also rejected. Events with a single isolated track (Sec. 5.3.6) and no object associated with it can indicate that a lepton was “lost” (i.e. either fallen out of acceptance or poorly reconstructed), hence such events are also vetoed. Detector and selection inefficiencies restrict the complete elimination of reducible backgrounds, as such, the method to estimate expected SM yields in the hadronic search region is described in Section 6.

## 5.6 Hadronic pre-selection

Events are categorized into two jet multiplicities:  $2 \leq n_{\text{jet}} \leq 3$  and  $n_{\text{jet}} \geq 4$ . Each event in these categories is further by the number of jets identified as originating from  $b$  quarks ( $n_b$ ). Events having three or more  $b$ -tagged jets are not considered in the analysis. Significant hadronic activity in the events is ensured by requiring  $H_T > 375 \text{ GeV}$ . As described in Section 5.4.1, events are further categorized in  $100 \text{ GeV}$  bins in  $H_T$  starting from  $H_T = 375 \text{ GeV}$  and ending with an open-ended bin  $H_T > 1075 \text{ GeV}$ . The two highest- $p_T$  jets are subject to a higher threshold,  $p_T > 100 \text{ GeV}$ , and the highest- $E_T$  jet is subjected to a tighter  $\eta$  acceptance requirement,  $|\eta| < 2.5$ . The variables  $H_T$  and  $\cancel{H}_T$  are computed from the number of jets,  $n_{\text{jet}}$ , that satisfy the  $p_T$  requirements listed in Table 8.

Table 8: Jet  $p_T$  thresholds per  $H_T$  bin.

$H_T$ bin	$>375$ GeV
Lead jet	100 GeV
Second jet	100 GeV
All other jets	50 GeV

## 5.7 Definition of $\alpha_T$

Multijet events stemming from QCD contribute overwhelmingly to all-hadronic events recorded by the detector. Generally, these multijet events have no significant imbalance in transverse energy and can be reduced with a requirement for high- $\cancel{E}_T$ . Yet, this approach is difficult, as the calculation of  $\cancel{E}_T$  is sensitive to detector effects and conditions, and additionally, in the high- $\cancel{E}_T$  phase space systematic uncertainties become difficult to control. The variable,  $\alpha_T$ , introduced in 2008 by Randall and Tucker-Smith [41] effectively suppresses multijet events with no significant  $\cancel{E}_T$  without relying on the measurement of  $\cancel{E}_T$ . By construction it also introduces robustness against mismeasurements of transverse energies in multijet systems. In the simplest case of a two-jet system,  $\alpha_T$  is defined as

$$\alpha_T = \frac{E_T^{j_2}}{M_T}, \quad (3)$$

where  $E_T^{j_2}$  is the transverse energy of the less energetic jet and  $M_T$  is the transverse mass of the dijet system, defined as

$$M_T = \sqrt{\left(\sum_{i=1}^2 E_T^{j_i}\right)^2 - \left(\sum_{i=1}^2 p_x^{j_i}\right)^2 - \left(\sum_{i=1}^2 p_y^{j_i}\right)^2} = \sqrt{H_T^2 + (\cancel{H}_T)^2}. \quad (4)$$

where the three terms,  $E_T^{j_i}$ ,  $p_x^{j_i}$ , and  $p_y^{j_i}$  are, respectively, the transverse energy and  $x$  or  $y$  components of the transverse momentum of jet  $j_i$ . By definition, the sum over the first term is  $H_T$  and the sums over the other two terms define  $\cancel{H}_T$ . In well measured dijet events, transverse momentum conservation requires the  $p_T$  of the two jets to be of equal magnitude and back-to-back in the plane transverse to the beam. The value of  $\alpha_T$  for these type of events can be best seen after transforming Equation 4 into CMS coordinates:

$$\alpha_T = \frac{E_T^{j_2}}{\sqrt{2E_T^{j_1} E_T^{j_2} (1 - \cos(\Delta\phi))}}. \quad (5)$$

Well balanced back-to-back jets have  $\alpha_T$  values of 0.5. For the case of an imbalance in the measured transverse energies of back-to-back jets  $\alpha_T$  is reduced to values smaller than 0.5, this gives the variable its robustness with respect to jet energy mismeasurements. In the case where the two jets are not back-to-back in the transverse plane but rather the dijet system balances genuine  $\cancel{E}_T$ , for example in leptonically decaying W boson recoiling off a system of jets, the values of  $\alpha_T$  can exceed 0.5. Figure 5.3 shows the  $\alpha_T$  distribution in two jet multiplicity bins for events passing an  $H_T$  trigger and basic pre-selection requirements. Multijet events from QCD drop to negligible levels above  $\alpha_T > 0.55$  while events with genuine  $\cancel{E}_T$  continue to populate bins in excess of  $\alpha_T > 0.55$ .

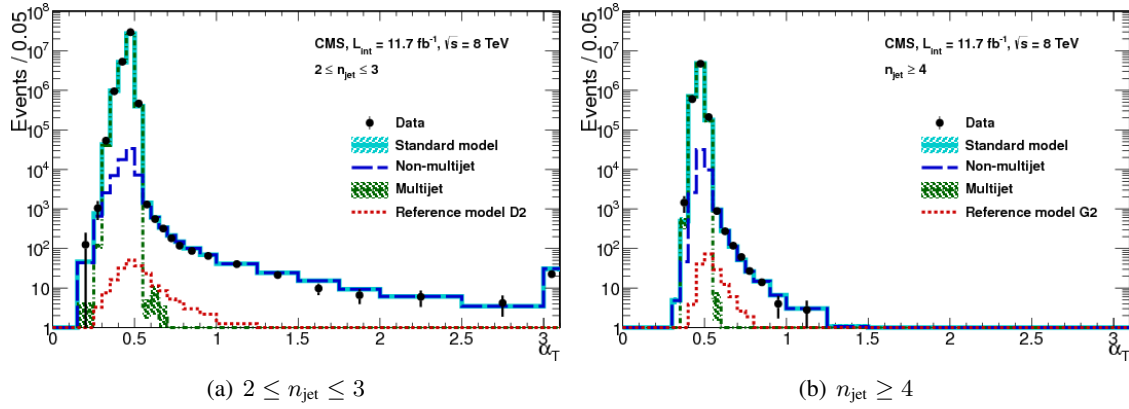


Figure 5.3: The  $\alpha_T$  distribution for  $11.7 \text{ fb}^{-1}$  of data collected at 8 TeV as well as for all SM backgrounds and one example SUSY signal sample, from Ref. [36]. This figure is for illustrative purposes only, as this analysis relies on data control samples to estimate contribution from SM process with genuine  $\cancel{E}_T$ .

An extension of  $\alpha_T$  can be made for events containing three or more jets by clustering the jets into two pseudo-jets [42]. A pseudo-jet's  $E_T$  is calculated as the scalar sum of the contributing jets' transverse energy, while the total transverse energy of the system,  $H_T$ , is defined as the scalar sum of the transverse energy of the pseudo-jets:  $H_T = E_T^{\text{pj}_1} + E_T^{\text{pj}_2}$ . All com-

binations of the  $n$ -jet system are tested, and the configuration which balances the constructed pseudo-jets'  $E_T$  is chosen, i.e. the combination which minimizes  $\Delta H_T = E_T^{\text{pj}_1} - E_T^{\text{pj}_2}$ . As balanced multijet events are expected to have small  $\Delta H_T$ , this simple clustering criterion provides the best separation between multijet events and events with genuine  $\cancel{E}_T$ . Equation (3) can therefore be generalized as:

$$\alpha_T = \frac{1}{2} \times \frac{H_T - \Delta H_T}{\sqrt{H_T^2 - \cancel{H}_T^2}} = \frac{1}{2} \times \frac{1 - (\Delta H_T/H_T)}{\sqrt{1 - (\cancel{H}_T/H_T)^2}}. \quad (6)$$

In the limit that  $\Delta H_T \rightarrow 0$ , the ratio of missing energy and visible energy can be expressed as a function of  $\alpha_T$ :

$$\frac{\cancel{H}_T}{H_T} = \sqrt{1 - \frac{1}{4 \cdot \alpha_T^2}} \quad (7)$$

This analysis uses an  $\alpha_T$  threshold of 0.55, which results in accepting events having more than 40% percent as much missing transverse energy as visible transverse energy. For an event with  $H_T = 375$  GeV, this amounts to nearly 160 GeV in  $\cancel{H}_T$ .

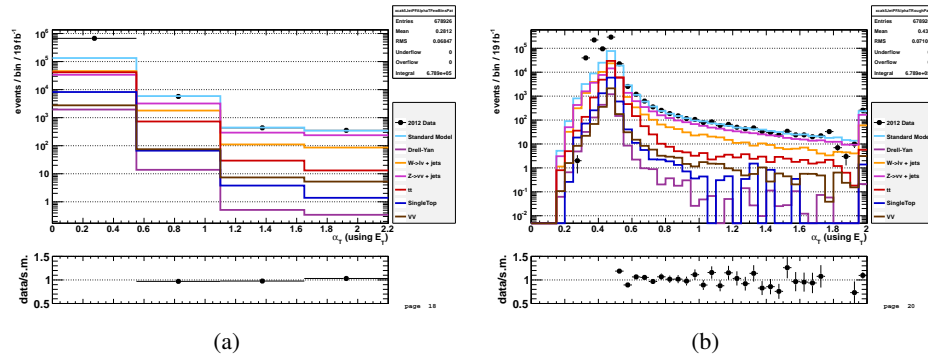


Figure 5.4: Data–MC comparison of the  $\alpha_T$  distribution after the application of the hadronic pre-selection criteria for events satisfying  $n_{\text{jet}} > 2$  and  $n_b > 0$  in histograms with (a) coarse and (b) fine binning.

## 5.8 Final selections

After applying the  $\alpha_T$  selection described in Section 5.7, the remaining events are expected to have little contamination from balanced multijet QCD events, i.e. at the sub-percent level. Furthermore, QCD events with mismeasured jets are largely rejected since they fall below the  $\alpha_T$  threshold. However, two types of rare backgrounds from multijet events can lead to values of  $\alpha_T$  greater than 0.55. The first is a rare circumstance in which several jets with similar values of the azimuthal angle ( $\phi$ ) fail to pass the jet  $p_T$  threshold. Such jets would not be considered in the calculation of  $H_T$  and as a result, they would bias the  $\cancel{H}_T$  calculation low. The events are rejected by comparing the  $\cancel{H}_T$  with the missing transverse energy,  $\cancel{E}_T^{\text{PF}}$  as defined in 5.3.5, such that events with  $R_{\text{miss}} = \cancel{H}_T / \cancel{E}_T^{\text{PF}} > 1.25$  are rejected. The second type of rare background is the severe mismeasurement of jets that are absorbed by inefficient crystals in the ECAL. These crystals, which make up 1% of the total crystal count, give only partial record of the energy deposited thereby introducing “fake”  $\cancel{H}_T$  in the event. As a filter, the quantity:

$$\Delta\phi^* \equiv \Delta\phi \left( \vec{p}_j, - \sum_{i \neq j} \vec{p}_i \right), \quad (8)$$

ie. the azimuthal distance between a jet and the  $\cancel{H}_T$  calculated when not considering the jet, is evaluated for all jets with  $p_T > 30$  GeV. Small values of  $\Delta\phi^*$  indicate jets that contributed most to the  $\cancel{H}_T$ . For each jet with  $\Delta\phi^* < 0.5$ , the number of dead ECAL cells within  $\Delta R(\vec{p}_j, \text{cell}) < 0.3$  is counted. If the number exceeds 9 for any jet, then the event is rejected.

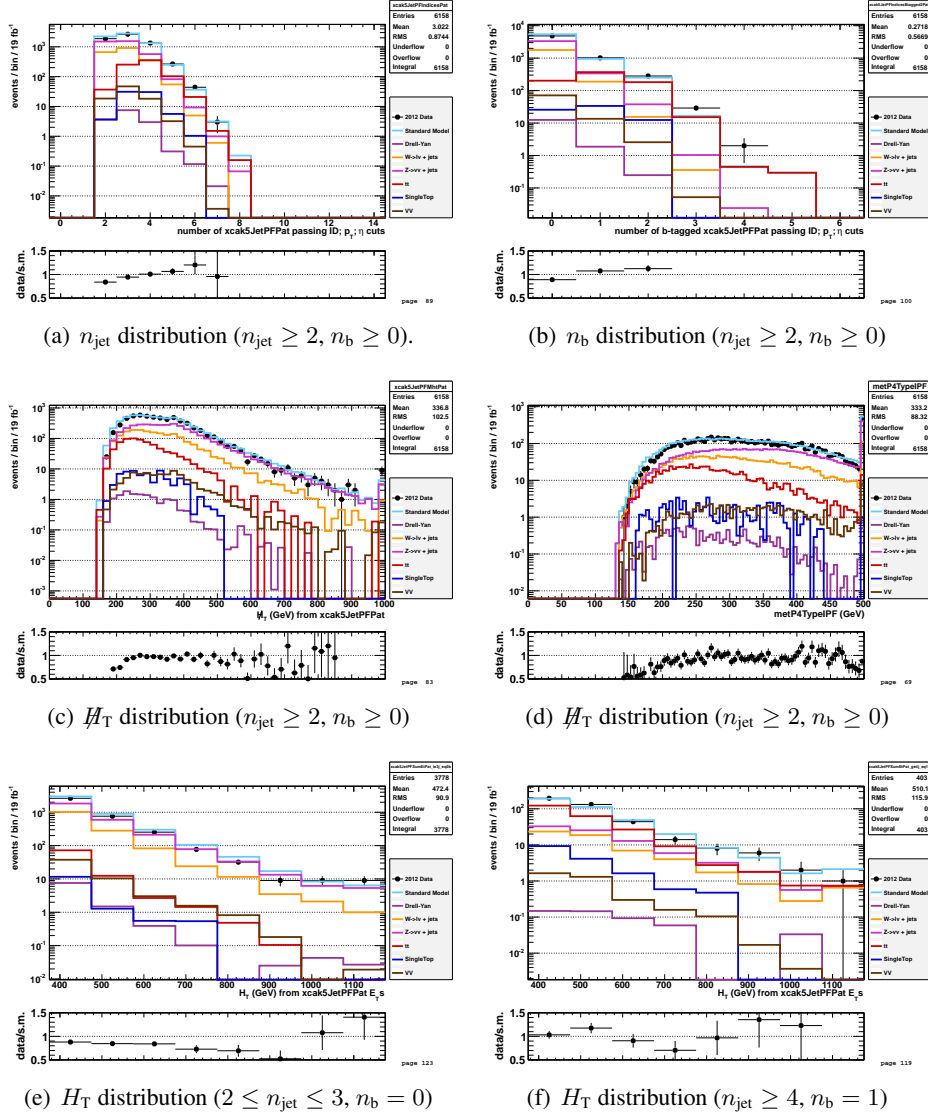


Figure 5.5: Data–MC comparisons of key variables for the hadronic search region, following the application of the full hadronic selection criteria and the requirements  $H_T > 375$  GeV and  $\alpha_T > 0.55$ : (a)  $n_{\text{jet}}$ , (b)  $n_b$ , (c)  $H_T$ , and (d)  $E_T$  distributions for an inclusive selection on  $n_{\text{jet}}$  and  $n_b$ , and (e,f)  $H_T$  for the two event categories ( $2 \leq n_{\text{jet}} \leq 3, n_b = 0$ ) and ( $n_{\text{jet}} \geq 4, n_b = 1$ ).

## 6 Background estimation for processes with genuine $\cancel{E}_T$

After applying the full hadronic selection, the remaining backgrounds are SM processes with genuine  $\cancel{E}_T$  in the final state. In the category of zero b-tagged jets, the two primary background sources are:

- $Z + \text{jets}$ ; where the  $Z$  boson decays into a pair of neutrinos,
- $W + \text{jets}$ ; where the  $W$  boson either undergoes a leptonic decay and the lepton is lost or it undergoes the weak decay  $W \rightarrow \tau \nu$  where the  $\tau$  decays into quarks

Other SM backgrounds, such as the diboson production ( $WW$ ,  $ZZ$ ,  $WZ$ ), single-top, and Drell-Yan ( $Z/\gamma^* \rightarrow l\bar{l}$ ) are also expected, but at lower yields.

For events with one or more b-tagged jets, the decay of  $t\bar{t}$ , where each top decays into a b-quark and a  $W$  boson which in turn decays into a lost lepton and a neutrino, also becomes a large background source. For events with two reconstructed b-quark jets,  $W + \text{jets}$  and  $Z + \text{jets}$  are suppressed and  $t\bar{t}$  production dominates the background.

This analysis uses a “data-driven” method to estimate backgrounds in the hadronic search region. Data control samples are used to predict the SM background yields instead of estimating them from MC simulations. This approach has two benefits. First, the beam and detector conditions for the hadronic and control data samples are very similar, therefore there is no need to rely on MC simulation getting the detector conditions correct, which is difficult. Second, the information used from MC simulation is largely in the form of ratios (Section 6.1), which has the benefit of canceling potential systematic effects or biases from the simulation.

Two different control samples are used to estimate the backgrounds. To estimate the  $Z \rightarrow \nu\bar{\nu} + \text{jets}$  background,  $\gamma + \text{jets}$  events are utilized. They have the same kinematic properties as  $Z \rightarrow \nu\bar{\nu} + \text{jets}$  when the photon is ignored, but different acceptance [43, 44]. A  $\mu + \text{jets}$  control sample is used to estimate all remaining backgrounds including the dominant  $W + \text{jets}$  and  $t\bar{t}$  process. The following sections describe the estimation method and control samples used for the estimation.

## 6.1 Overview of the method

For a given bin in  $H_T$ ,  $n_{\text{jet}}$ ,  $n_b$ , the method predict the number of events expected from background processes in the hadronic search region ( $N_{\text{pred}}^{\text{had}}$ ) by translating from the observed data yield in a control region ( $N_{\text{obs}}^{\text{control}}$ ) through the use of a *translation factor* (TF) constructed from the ratio of MC hadronic and control yields ie:

$$N_{\text{pred}}^{\text{had}} = \underbrace{\frac{N_{\text{MC}}^{\text{had}}}{N_{\text{MC}}^{\text{control}}}}_{\text{translation factor}} \times N_{\text{obs}}^{\text{control}}, \quad (9)$$

where  $N_{\text{MC}}^{\text{had}}$  is the number of expected events of the background source(s) in the hadronic selection that are present in the control region under study.  $N_{\text{MC}}^{\text{control}}$  is the sum of expected yields from all MC samples, obtained for the relevant control sample selection:

$$N_{\text{MC}}^{\text{control}} = N_W + N_{t\bar{t}} + N_{Z \rightarrow \nu\bar{\nu}} + N_{\text{DY}} + N_{\gamma} + N_{\text{top}} + N_{\text{di-boson}} \quad (10)$$

Depending on the b-tag category, one or both control samples are used to predict the backgrounds in the hadronic search region. For the b-jet multiplicity bins  $n_b = 0$  and  $n_b = 1$ , the  $\mu + \text{jets}$  and  $\gamma + \text{jets}$  control samples are used to predict the total background. The  $\gamma + \text{jets}$  control sample is used to predict the  $Z \rightarrow \nu\bar{\nu} + \text{jets}$  background and the expected yield obtained from the  $Z \rightarrow \nu\bar{\nu}$  sample enters the numerator of each translation factor:

$$N_{\text{MC}}^{\text{had}}(H_T, n_{\text{jet}}, n_b \leq 1) = N_{Z \rightarrow \nu\bar{\nu}}. \quad (11)$$

For the same b-tag categories, the  $\mu + \text{jets}$  control sample is used to predict the remaining SM background processes, namely the  $W + \text{jets}$ ,  $t\bar{t} + \text{jets}$ , Drell-Yan, di-boson and single top backgrounds, and the total expected yield from these processes enter the numerator of each translation factor:

$$N_{\text{MC}}^{\text{had}}(H_T, n_{\text{jet}}, n_b \leq 1) = N_W + N_{t\bar{t}} + N_{\text{DY}} + N_{\text{top}} + N_{\text{di-boson}} \quad (12)$$



Only the  $\mu$  + jets control sample is used to predict the background in the the b-tag multiplicity bin  $n_b = 2$ . The  $\gamma$  + jets control sample is not used as the yield in this data control sample is expected to be low due to the requirement of at least two b-jets per event. The method of using a W + jets sample to predict the  $Z \rightarrow \nu\bar{\nu}$  + jets background has been used previously [23, 36, 45]. Therefore the total predicted expected yield from all processes enter the numerator of each translation factor:

$$N_{\text{MC}}^{\text{had}}(H_T, n_{\text{jet}}, n_b = 2) = N_W + N_{t\bar{t}} + N_{\text{DY}} + N_{\text{top}} + N_{\text{di-boson}} + N_{Z \rightarrow \nu\bar{\nu}} \quad (13)$$

The control samples used to predict the SM backgrounds for each event category are summarized in Table 9. A detailed example of the background estimation procedure is given in Appendix A. Tables 20–29 in Appendix B show the control sample yields, translation factors, hadronic MC yields, for each control sample in each category. The control sample selections are described in the following sections.

Table 9: Summary of control samples used to predict the SM background for each event category.

$n_{\text{jet}}$	$n_b$	Control samples
2–3	0	$\mu$ + jets, $\gamma$ + jets
2–3	1	$\mu$ + jets, $\gamma$ + jets
2–3	2	$\mu$ + jets
$\geq 4$	0	$\mu$ + jets, $\gamma$ + jets
$\geq 4$	1	$\mu$ + jets, $\gamma$ + jets
$\geq 4$	2	$\mu$ + jets

## 6.2 Definition of the control samples

### 6.2.1 Muon and photon triggers

Events for the muon control sample are recorded with the HLT\_IsoMu24\_eta2p1 trigger. Figure 6.1 (left) shows the HLT\_IsoMu24\_eta2p1 trigger efficiency as determined in bins of number of primary vertices for muon  $p_T > 25$  GeV and  $|\eta| < 2.1$  [46]. Figure 6.1 (right) shows the distribution of the number of vertices in the muon control sample seeded by the HLT\_IsoMu24\_eta2p1. The efficiency at the mean number of vertices  $n_{vtx} = 13$  is taken as flat trigger efficiency across  $n_{jet}$ ,  $n_b$ , and  $H_T$ . This measurement agrees well with direct tag and probe measurements in bins of  $n_{jet}$ ,  $n_b$ ,  $H_T$  done elsewhere [36].

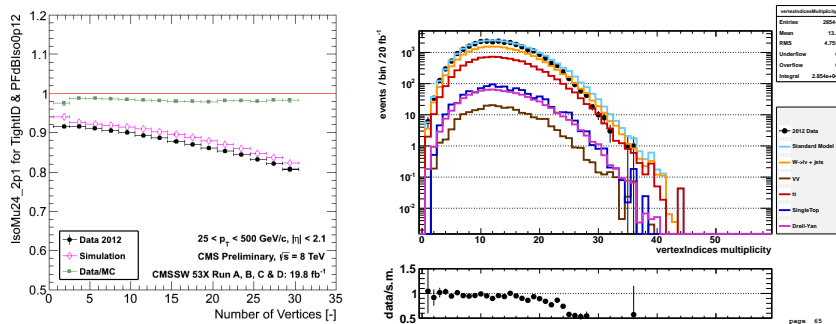


Figure 6.1: (left) Muon trigger efficiency as a function of number of primary vertices for muon  $p_T > 25$  GeV and  $|\eta| < 2.1$ . (right) Number of primary vertices in muon control sample.

Events for the photon control sample are recorded with the HLT\_Photon150 trigger, which is  $\sim 100\%$  efficient for  $E_T^{\text{photon}} > 165$  GeV and  $H_T > 375$  GeV, as shown in Figure 6.2. The efficiency measurement is made using the HLT\_Photon90 trigger as a reference.

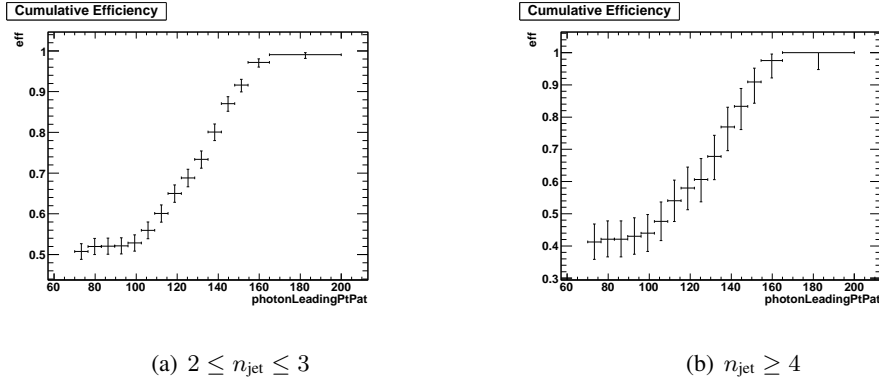


Figure 6.2: Cumulative efficiency turn-on curves for the HLT\_Photon150 trigger as a function of photon  $p_T$  for events satisfying  $2 \leq n_{\text{jet}} \leq 3$  (left) and  $n_{\text{jet}} \geq 4$  (right).

### 6.2.2 The $\mu$ + jets control sample

$W$  + jets and  $t\bar{t}$  processes are found in the hadronic search region when the decay lepton is missed by the lepton veto, either because it was not reconstructed properly, fell out of acceptance or alternatively, decayed hadronically in the case of a tau lepton from a high- $p_T$   $W$  boson. Instead of directly relying on MC simulation to estimate these backgrounds, a  $\mu$  + jets control sample is used where the selection criteria is chosen to identify  $W$  bosons decaying to a muon and a neutrino. Then, by removing the muon from the event, one effectively selects a sample of  $W$  boson decaying to a neutrino and a lost lepton. In order to select events containing  $W$  bosons, exactly one tight isolated muon 5.3 with of  $p_T > 30$  GeV and  $|\eta| < 2.1$  is required, and the transverse mass of the  $W$  candidate,  $M_T = \sqrt{2p_T^\mu E_T(1 - \cos(\Delta\phi(\vec{p}^\mu, \vec{E}_T)))}$  must be between 30 and 125 GeV. Events are vetoed if a muon is found inside a jet, i.e.  $\Delta R(\mu, \text{jet}) < 0.5$ . The single isolated track veto, described in Sections 5.3.6 and 5.5, is applied. The veto considers all single isolated tracks in the event except that associated with the identified, isolated muon. The cleaning cut  $H_T/\cancel{E}_T^{\text{PF}}$  described in 5.8 is also applied, where the  $\cancel{E}_T^{\text{PF}}$  is adjusted to exclude the muon's transverse momentum. This modification ensures that the quantities  $H_T$  and  $\cancel{E}_T^{\text{PF}}$  can be compared. Lastly, while all other jet-based quantities, like  $H_T$  and  $\cancel{H}_T$ , are kept consistent with those applied in the hadronic search region, the  $\alpha_T$

requirement is removed. This modification increases the statistical power of the sample. Removing the  $\alpha_T$  requirement is only made possible by the control sample's kinematic cuts which ensure the selection of electroweak processes while keeping contamination from multijet QCD events negligible. Because the control sample is used to extrapolate yields in a hadronic search region, which includes the  $\alpha_T$  requirement, a closure test as been devised and explained in Section 7.1 to demonstrate that no significant biases are seen from the exclusion of the  $\alpha_T$  cut.

### 6.2.3 The $\gamma$ + jets control sample

The  $Z \rightarrow \nu\bar{\nu}$  + jets background is estimated using  $\gamma$  + jets events which have a higher cross-section but similar kinematic properties as  $Z \rightarrow \nu\bar{\nu}$  + jets when the photon is ignored [43, 44]. The  $\gamma$  + jets sample is obtained by requiring exactly one tightly identified and isolated photon (as defined in Section 5.3) with a transverse momentum of at least 165 GeV. The photon is required to be contained within the barrel of the detector, ie  $|\eta_\gamma| < 1.44$ , and to not overlap with any reconstructed jets  $\Delta R(\gamma, \text{jet}) < 1.0$ . As in the muon control sample, the  $\vec{\cancel{E}}_T$  is modified to exclude the photon when imposing the  $\cancel{H}_T/\cancel{E}_T^{\text{PF}} < 1.25$  selection cut. All other selections are consistent with the hadronic search region including the  $\alpha_T > 0.55$  cut.

## 7 Closure tests and systematic uncertainties on translation factors

Limitations in simulating detector effects and event kinematics requires us to apply appropriate systematic uncertainties on the simulation-based translation factors. The following section describes how we obtain these uncertainties through the method of closure tests.

### 7.1 Closure tests

At its core, the method compares an observed yield ( $N_{\text{obs}}$ ) and a predicted yield ( $N_{\text{pred}}$ ) in a sub-sample of a control region. The predicted yield is constructed by translating from a statistically independent data sample to the data sample of interest by the use of the proper translation factor. For example, in a given  $H_T$  bin, a prediction for the  $n_{\text{jet}} \geq 4$ ,  $n_b = 1$ ,  $\mu + \text{jets}$  sample can be made by translating from the  $2 \leq n_{\text{jet}} \leq 3$ ,  $n_b = 1$ ,  $\mu + \text{jets}$  in data via the translation factor:

$$\frac{N_{\text{MC}}^{\mu+\text{jets}}(H_T, n_{\text{jet}} \geq 4, n_b = 1)}{N_{\text{MC}}^{\mu+\text{jets}}(H_T, 2 \leq n_{\text{jet}} \leq 3, n_b = 1)} \quad (14)$$

The agreement between  $N_{\text{obs}}$  and  $N_{\text{pred}}$  is expressed as  $(N_{\text{obs}} - N_{\text{pred}})/N_{\text{pred}}$ . Assuming only statistical uncertainties on  $N_{\text{obs}}$  and  $N_{\text{pred}}$ , deviation of the ratio from zero defines our level of closure. A closure test set is defined as ratios for each  $H_T$  bin. Looking at the ratio as a function of  $H_T$  allows the measurement of statistical significant biases from zero and/or any dependence on  $H_T$ . If statistically significant biases are observed, further studies are required to understand and correct for these biases.

Eight sets of closure tests probe key ingredients of the simulation modeling of the SM backgrounds with genuine  $\cancel{E}_T$  as a function of  $H_T$ , as shown in Fig. 7.1. This is done for the two jet multiplicity bins separately:  $2 \leq n_{\text{jet}} \leq 3$ , and  $n_{\text{jet}} \geq 4$ .

Under the assumption of closure for the full ensemble of tests, systematic uncertainties on the translation factors are derived for each  $n_{\text{jet}}$  category and  $H_T$  regions. The treatment for estimating the systematic uncertainties on the translation factors is described in Section 7.2.

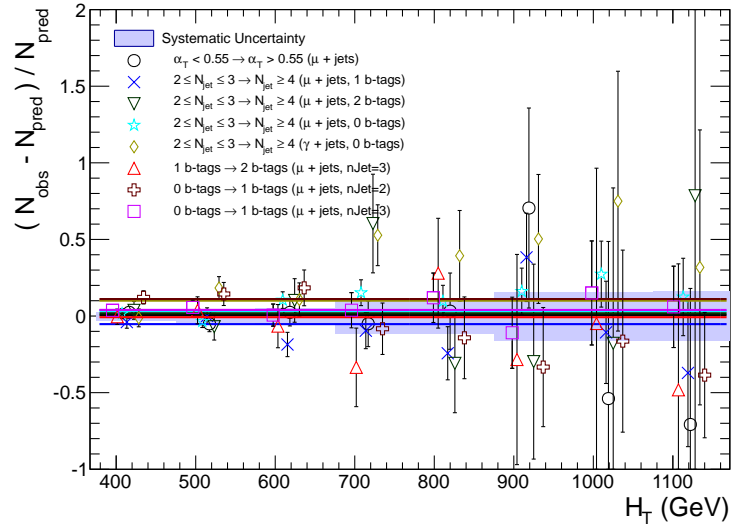
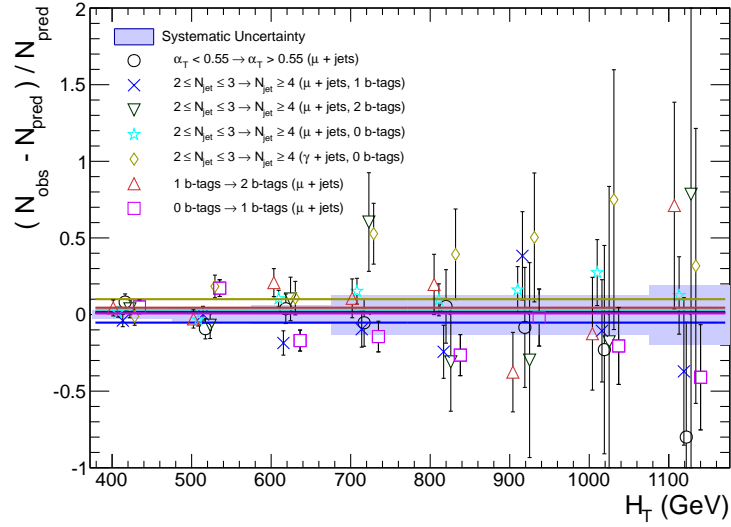
(a)  $2 \leq n_{\text{jet}} \leq 3$ ,(b)  $n_{\text{jet}} \geq 4$ ,

Figure 7.1: Sets of closure tests (open symbols) overlaid on top of the systematic uncertainty used for each of the  $H_T$  region (shaded bands) and for the two different jet multiplicity bins: (a)  $2 \leq n_{\text{jet}} \leq 3$  and (b)  $n_{\text{jet}} \geq 4$ .

As described in Section 6.2.2 the  $\alpha_T$  requirement is not imposed in the  $\mu$  + jets control sample. Therefore it is important to verify the approach of using  $\mu$  + jets samples without an  $\alpha_T$  requirement to make background predictions in the signal region. The first set of closure tests (denoted by circles) attempts to do this by probing the modeling of the  $\alpha_T$  distribution in genuine  $\cancel{E}_T$  events as a function of  $H_T$ . The test compares data yields in the  $\mu$  + jets sample with an  $\alpha_T$  requirement against predictions determined in a  $\mu$  + jets sample with the  $\alpha_T$  requirement inverted.

The next three sets (triangles, crosses, squares) probe the sensitivity of the  $\mu$  + jets translation factors to the relative admixture of events from the  $W$  + jets and  $t\bar{t}$  processes. These tests are conservative, since by construction, the admixture changes little when translating from the  $\mu$  + jets control region to the signal region, whereas the closure tests use sub-samples with different b-tag requirements and therefore have very different admixtures of  $W$  + jets and  $t\bar{t}$  events. In the  $2 \leq n_{\text{jet}} \leq 3$  bin, the test is sub-divided into separate jet categories. These tests also probe the modeling of the reconstruction of b-quark jets, although this is also addressed more fully by dedicated studies that determine systematic uncertainties via the method described in Section 10.3.5.

The remaining tests probe the simulation modeling of the jet multiplicity in the  $\mu$  + jets and  $\gamma$  + jets samples, which is checked due to the exclusive binning in jet multiplicity. As in the case of the  $W$  + jets /  $t\bar{t}$  admixture, this set of tests is a very conservative check, as predictions are always made from the same jet multiplicity bin, whereas the closure tests translate between the two bins.

Tables 10 and 11, which summarize the results obtained from fits of zeroth order polynomials (i.e. a constant) to the sets of closure tests performed in the  $2 \leq n_{\text{jet}} \leq 3$  and  $n_{\text{jet}} \geq 4$  bins. Table 12 lists the fits result common to both jet multiplicities. The best fit value and its uncertainty is listed for each set of closure tests, along with the  $\chi^2$ , the number of degrees of freedom, and the p-value of the fit. The best fit value for the constant parameter is indicative of the level of closure, as averaged across the full  $H_T$  range considered in the analysis, and the p-value is indicative of whether there is any significant dependence on  $H_T$ .

The closure tests demonstrate, within the statistical precision of each test, that there are

Table 10: A summary of the results obtained from fits of zeroth order polynomials (i.e. a constant) to binned  $H_T$  distributions for four sets of closure tests performed in the  $2 \leq n_{\text{jet}} \leq 3$  bin.

Closure test	In Fig. 7.1(a) Symbol	Constant fit			
		Best fit value	$\chi^2$	d.o.f.	p-value
$\alpha_T < 0.55 \rightarrow \alpha_T > 0.55$ ( $\mu$ + jets)	Circle	$0.007 \pm 0.02$	3.91	7	0.79
1 b-tags $\rightarrow$ 2 b-tags ( $\mu$ + jets, $n_{\text{jet}}=3$ )	Triangle	$-0.008 \pm 0.04$	3.20	7	0.87
0 b-tags $\rightarrow$ 1 b-tags ( $\mu$ + jets, $n_{\text{jet}}=2$ )	Cross	$0.111 \pm 0.03$	5.87	7	0.55
0 b-tags $\rightarrow$ 1 b-tags ( $\mu$ + jets, $n_{\text{jet}}=3$ )	Square	$0.040 \pm 0.02$	1.12	7	0.99

Table 11: A summary of the results obtained from fits of zeroth order polynomials (i.e. a constant) to three sets of closure tests performed in the  $n_{\text{jet}} \geq 4$  bin. <sup>†</sup>Further explanation of this fit can be found in the text.

Closure test	In Fig. 7.1(b) Symbol	Constant fit			
		Best fit value	$\chi^2$	d.o.f.	p-value
$\alpha_T < 0.55 \rightarrow \alpha_T > 0.55$ ( $\mu$ + jets)	Circle	$0.011 \pm 0.04$	5.81	7	0.56
1 b-tags $\rightarrow$ 2 b-tags ( $\mu$ + jets)	Triangle	$0.045 \pm 0.03$	9.36	7	0.23
0 b-tags $\rightarrow$ 1 b-tags ( $\mu$ + jets)	Square	$0.007 \pm 0.03$	25.30	7	$7.6 \times 10^{-4}$
0 b-tags $\rightarrow$ 1 b-tags ( $\mu$ + jets) <sup>†</sup>	Square	$0.009 \pm 0.03$	10.12	6	0.12

Table 12: A summary of the results obtained from fits of zeroth order polynomials (i.e. a constant) to four sets of closure tests ( $2 \leq n_{\text{jet}} \leq 3 \rightarrow n_{\text{jet}} \geq 4$ ) that probe the accuracy of the MC modeling of the  $n_{\text{jet}}$  distribution observed in data, using the three data control samples.

Closure test	In Fig. 7.1(a), 7.1(b) Symbol	Constant fit			
		Best fit value	$\chi^2$	d.o.f.	p-value
$2 \leq n_{\text{jet}} \leq 3 \rightarrow n_{\text{jet}} \geq 4$ ( $\mu$ + jets, 1 b-tags)	$\times$	$-0.053 \pm 0.03$	8.02	7	0.33
$2 \leq n_{\text{jet}} \leq 3 \rightarrow n_{\text{jet}} \geq 4$ ( $\mu$ + jets, 1 b-tags)	Invert. Triangle	$0.018 \pm 0.04$	6.23	7	0.51
$2 \leq n_{\text{jet}} \leq 3 \rightarrow n_{\text{jet}} \geq 4$ ( $\mu$ + jets, 0 b-tags)	Star	$0.034 \pm 0.02$	9.24	7	0.24
$2 \leq n_{\text{jet}} \leq 3 \rightarrow n_{\text{jet}} \geq 4$ ( $\gamma$ + jets, 0 b-tags)	Diamond	$0.100 \pm 0.04$	12.20	7	0.09

no significant biases or dependencies on  $H_T$  inherent in the translation factors obtained from simulation.

One set of tests does indicate a poor goodness of fit (indicated by a low p-value), which is the  $n_b = 0 \rightarrow n_b = 1$  test in the  $\mu$  + jets sample for the  $n_{\text{jet}} \geq 4$  category (Table 11), which has been identified as an upward (downward) fluctuation of event counts in the  $H_T$  bin



475–575 GeV (575–675 GeV) when  $n_b = 1$ . Combining these two bins yields an acceptable fit result, as indicated by the best fit value (consistent with zero), which points to a simple fluctuation rather than any systematic bias.

## 7.2 Systematic uncertainties from closure tests

Once it is established that no significant large bias or trend is observed for any set of closure tests, then systematic uncertainties are determined. For each  $H_T$  bin, the systematic uncertainty is estimated by taking the sum in quadrature of the weighted mean and sample variance of  $\frac{N_{\text{obs}} - N_{\text{pred}}}{N_{\text{pred}}}$  for each closure test. This procedure yields the values quoted in Table 13.

As the closure tests do not translate from control region to signal region, they do not probe the uncertainty in the signal trigger efficiencies. To account for this, a trigger uncertainty of 5% is added in quadrature to the uncertainty values obtained via the closure tests and the total is summarized in Table 14.

Table 13: A summary of the magnitude of the systematic uncertainties (%) obtained from closure tests, for each to  $n_{\text{jet}}$  and  $H_T$  bin.

$n_{\text{jet}}$	$H_T$ bin (GeV)							
	375–475	475–525	525–675	675–775	775–875	875–975	1075–1075	> 1175
2–3	3	4	5	11	11	16	16	16
$\geq 4$	3	4	6	13	13	13	13	20

Table 14: A summary of the magnitude of the total systematic uncertainties (%) assigned to the translation factors, according to  $n_{\text{jet}}$  and  $H_T$  bin.

$n_{\text{jet}}$	$H_T$ bin (GeV)							
	375–475	475–525	525–675	675–775	775–875	875–975	1075–1075	> 1175
2–3	6	6	7	12	12	17	17	17
$\geq 4$	6	6	8	14	14	14	14	21

Figure 7.1 shows the sets of closure tests overlaid on top of gray bands that represent the  $H_T$ -dependent systematic uncertainties in Table 13. These systematic uncertainties are assumed to be fully uncorrelated between the different b-jet multiplicity categories and also

the eight  $H_T$  bins, which is a conservative approach given that one can expect some correlation between adjacent  $H_T$  bins (due to comparable kinematics).

## 8 Statistical framework

The observations in the hadronic and control regions described in chapter 6 are interpreted through a likelihood model constructed in the following section. The method to set a limit on the cross-section of signal models is described in section 11.1.

### 8.1 Likelihood model

#### 8.1.1 Hadronic sample

For a given  $n_{\text{jet}}$  and  $n_b$  category, let  $N$  be the number of bins of  $H_T$ . Let  $n^i$  represent the number of events observed satisfying all selection requirements in each  $H_T$  bin  $i$ . The likelihood of the observations can be written as:

$$L_{\text{hadronic}} = \prod_i \text{Pois}(n^i | b^i + s^i) \quad (15)$$

where  $b^i$  represents the expected Standard Model background in bin  $i$ ,  $s^i$  represents the expected number of signal events in bin  $i$ , and  $\text{Pois}$  represents the Poisson distribution:

$$\text{Pois}(k; \lambda) = \frac{\lambda^k \exp(-\lambda)}{k!} \quad (16)$$

Due to the choice in  $\alpha_T$  and  $H_T$  thresholds, the contribution from QCD events is expected to be negligible, Sec. 5.7. Therefore, it is assumed that  $b^i \equiv \text{EWK}^i$  where  $\text{EWK}^i$  is the expected yield of electroweak events in bin  $i$ .

#### 8.1.2 Electroweak control samples

The electroweak background can be split into its reducible and irreducible backgrounds, i.e.  $\text{EWK}^i = Z_{\text{inv}}^i + ttW^i$ .  $Z_{\text{inv}}^i$  represents the contribution from  $Z \rightarrow \nu\bar{\nu} + \text{jets}$  events in  $H_T$  bin  $i$  of the hadronically selected sample, and the variable  $ttW^i$  represents the contribution from all other backgrounds in  $H_T$  bin  $i$  of the hadronically selected sample.

In each bin  $i$  of  $H_T$ , there are two measurements:  $n_{ph}^i, n_\mu^i$ , representing the event counts in the photon and single-muon. Each of these measurements has a corresponding yield in simulated data:  $MC_{ph}^i, MC_\mu^i$ . The simulation also gives expected amounts of  $Z_{\text{inv}}$  and  $t\bar{t}+W$  in the hadronically-selected sample:  $MC_{Z_{\text{inv}}}^i$  and  $MC_{t\bar{t}+W}^i$ . After defining

$$r_{ph}^i = \frac{MC_{ph}^i}{MC_{Z_{\text{inv}}}^i}; r_\mu^i = \frac{MC_\mu^i}{MC_{t\bar{t}+W}^i} \quad , \quad (17)$$

these likelihood functions are used:

$$L_{ph} = \prod_i \text{Pois}(n_{ph}^i | \rho_{phZ}^j \cdot r_{ph}^i \cdot Z_{\text{inv}}^i) \quad (18)$$

$$L_\mu = \prod_i \text{Pois}(n_\mu^i | \rho_{\mu W}^j \cdot r_\mu^i \cdot ttW^i + s_\mu^i) \quad . \quad (19)$$

Equation 18 can be used to estimate the maximum likelihood value for  $Z_{\text{inv}}^i$  (the expectation for the  $Z \rightarrow \nu\bar{\nu}$  + jets background in the hadronic signal region) given the observations  $n_{ph}^i$  in the photon control sample and the ratios  $r_{ph}^i$ . A similar construction is used when estimating  $ttW^i$  from the single muon control sample (Equ. 19). The measurements in each of the control samples and the hadronic search region, along with the ratios  $r_{ph}^i$  and  $r_\mu^i$ , are all considered simultaneously through the relationship  $\text{EWK}^i = Z_{\text{inv}}^i + ttW^i$ . The ratios  $r_{ph}^i$  and  $r_\mu^i$  are simply the inverse of the translation factor (1/TF) defined in Equ. 9 (Sec. 6.1). More specifically,  $MC_{ph}^i$  and  $MC_\mu^i$  are the yields obtained from MC after applying the selection criteria for the photon and single muon samples, as defined by Equ. 31 (Sec. 6.1). The variables  $MC_{t\bar{t}+W}^i$  and  $MC_{Z_{\text{inv}}}^i$  are defined by Eqs. 11 and 12 (Sec. 6.1), respectively.

The parameters  $\rho_{phZ}^j$  and  $\rho_{\mu W}^j$  represent “correction factors” that accommodate the systematic uncertainties associated with the control-sample-based background constraints. The quantities  $\sigma_{phZ}^j$  and  $\sigma_{\mu W}^j$  represent the relative systematic uncertainties for the control sample constraints, taken into account with the following terms:

$$L_{\text{EWK syst.}} = \prod_j \text{Logn}(1.0 | \rho_{\mu W}^j, \sigma_{\mu W}^j) \times \text{Logn}(1.0 | \rho_{phZ}^j, \sigma_{phZ}^j) \quad , \quad (20)$$

where Logn is the log-normal distribution [47]:

$$\text{Logn}(x|\mu, \sigma_{\text{rel.}}) = \frac{1}{x\sqrt{2\pi \ln k}} \exp\left(-\frac{\ln^2\left(\frac{x}{\mu}\right)}{2 \ln^2 k}\right); \quad k = 1 + \sigma_{\text{rel.}} \quad . \quad (21)$$

One systematic parameter is assigned per  $H_T$  bin.

For the categories where  $n_b = 2$ , the single muon sample is used to constrain the total EWK background thus:

$$r'_\mu{}^i \equiv \frac{MC_\mu^i}{MC_{t\bar{t}+W+Z_{\text{inv}}}^i} \quad ; \quad (22)$$

$$L_\mu = \prod_i \text{Pois}(n_\mu^i | \rho_{\mu W}^j \cdot r'_\mu{}^i \cdot \text{EWK}^i + s_\mu^i) \quad . \quad (23)$$

The photon likelihood is dropped and splitting  $\text{EWK}^i$  is no longer necessary thus  $Z_{\text{inv}}^i$  and  $t\bar{t}W^i$  can be dropped.

### 8.1.3 Contributions from signal

Let  $x$  represent the cross section for a particular signal model, and let  $l$  represent the recorded luminosity. Let  $\epsilon_{\text{had}}^i$  be the analysis efficiency as simulated for the model in  $H_T$  bin  $i$  of the hadronic sample. Let  $\delta$  represent the relative uncertainty on the signal yield, assumed to be fully correlated among the bins, and let  $\rho_{\text{sig}}$  represent the ‘‘correction factor’’ to the signal yield which accommodates this uncertainty. Let  $f$  represent an unknown multiplicative factor on the signal cross section, for which an allowed interval shall be determined.

Then the expected hadronic signal yield  $s^i$  from Equation 15 is written as  $s^i \equiv f \rho_{\text{sig}} x l \epsilon_{\text{had}}^i$ . The systematic uncertainty on the signal efficiency is included via an additional term in the likelihood:

$$L_{\text{sig}} = \text{Logn}(1.0 | \rho_{\text{sig}}, \delta) \quad . \quad (24)$$

### 8.1.4 Total likelihood

The likelihood function for a given selection  $k$  is the product of the terms described in the previous sections:

$$L^k = L_{hadronic}^k \times L_{\mu}^k \times L_{ph}^k \times L_{\text{EWK syst.}}^k \quad . \quad (25)$$

A final reparametrization of the variables  $Z_{\text{inv}}$  and  $ttW$  is made by introducing,  $f_{Z_{\text{inv}}}$ , the fraction of  $Z \rightarrow \nu\bar{\nu} + \text{jets}$  events in the total electroweak background:

$$Z_{\text{inv}}^i \equiv f_{Z_{\text{inv}}}^i \times \text{EWK}^i \quad (26)$$

$$ttW^i \equiv (1 - f_{Z_{\text{inv}}}^i) \times \text{EWK}^i \quad (27)$$

This reparametrization allows representing the fit results with the floating parameters  $\text{EWK}^i$  which is convenient for comparison to the observed data in the hadronic region.

In a category with 8  $H_T$  bins and two control samples, there are 32 nuisance parameters:  $\{\text{EWK}^i\}_{i=0}^7$ ,  $\{f_{Z_{\text{inv}}}^i\}_{i=0}^7$ ,  $\{\rho_{phZ}\}_{i=0}^7$ ,  $\{\rho_{muZ}\}_{i=0}^7$ . In the  $n_b = 2$  categories there are 18 nuisance parameters:  $\{\text{EWK}^i\}_{i=0}^7$ ,  $\{f_{Z_{\text{inv}}}^i\}_{i=0}^7$ ,  $\{\rho_{muZ}\}_{i=0}^7$ . When considering signal, there is also the parameter  $\rho_{sig}$ ; when multiple categories are fit simultaneously, the total likelihood is

$$L = L_{sig} \times \prod_k L_{hadronic}^k \times L_{\mu}^k \times L_{ph}^k \times L_{\text{EWK syst.}}^k \quad . \quad (28)$$

## 9 Results

The likelihood described in 8.1 is used to relate yields, uncertainties. It is constructed using ROOTFIT [48] and maximized using MINUIT [49].

### 9.1 Standard Model

To test compatibility with a Standard Model only hypothesis, the signal term is removed from the likelihood model. The parameter values maximizing the likelihood function are listed in Tables 30–35 found in Appendix C. The resulting SM yields along with the observed data yields are summarized in Tables D. The uncertainty on the yields are obtained by constructing a probability density function (p.d.f) from the maximized likelihood, then generating an ensemble of pseudo-experiments from this p.d.f. and maximizing the same likelihood form for each pseudo-experiment, resulting in an ensemble of yields. The 68% quantile of each ensemble defines the quoted uncertainty on the corresponding yield.

Figures 9.2–9.7 show the  $H_T$ -binned observed data yields (black filled circles) and the SM expectations and uncertainties (dark blue solid line with light blue bands) as determined by the fit for the hadronic signal region and the  $\mu + \text{jets}$  or both ( $\mu + \text{jets}, \gamma + \text{jets}$ ) control samples, depending on the event category. The uncertainties in the SM expectations obtained from the ensemble of pseudo-experiments reflect the statistical uncertainties in the considered data samples and the systematic uncertainties in the transfer factors as discussed in section 7. Figures 9.2–9.7 are summarized in tabular format in Tables 36–41 in appendix D along with observed data yields and the fit result for all event categories and both signal region and control sample bins.

For each  $n_b, n_{\text{jet}}$  category, the goodness-of-fit of the SM-only hypothesis is determined by considering simultaneously all  $H_T$  bins entering the likelihood. The goodness-of-fit described in [50] is obtained by comparing the nominal maximized likelihood value  $L_{\text{max}}^{\text{data}}$  to the corresponding ensemble of values,  $L_{\text{max}}$ . The quantile which  $L_{\text{max}}^{\text{data}}$  falls in the distributions is interpreted as a p-value. A p-value derived from a chi-square is also plotted for comparison.

The p-values obtained, shown in Figure 9.1 (Left), are found to be uniformly distributed in the range 0.0–1.0, with the lowest p-value determined to be 0.06.

The compatibility of the SM expectation and observed event count is also evaluated for each of the 48 hadronic search bins. A profile likelihood ratio is used to determine a p-value and the pull per signal region bin. Figure 9.1(b) shows the pull as a function of the signal region bin (Right). In general the SM-only hypotheses agrees well with data, though there are mild excesses (i.e.  $> 1.5\sigma$ ) in the  $n_b = 1$  and  $n_b = 2$  bins where the most pronounced excess is in the  $n_{\text{jet}} \geq 4, n_b = 2, 575 < \text{scalht} < 675$  bin, with  $2.4\sigma$ . In summary, an excess greater than  $2\sigma$  in one of 48 search bins is consistent with an, albeit rare, statistical fluctuation.

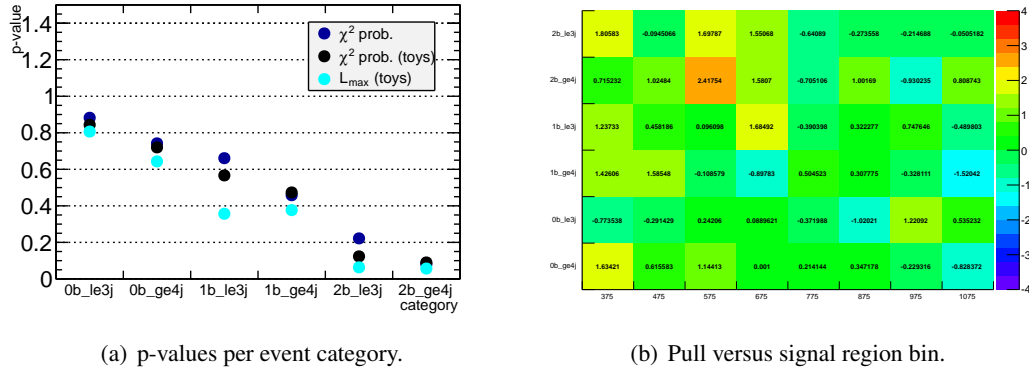


Figure 9.1: Pulls and p-values. See text for details



Table 15: Summary of hadronic yields from fit.

	375–475	475–575	575–675	675–775	775–875	875–975	975–1075	1075– $\infty$
0b le3j SM	$2744^{+48}_{-43}$	$771^{+21}_{-23}$	$254^{+13}_{-13}$	$76.5^{+6.1}_{-4.8}$	$33.7^{+3.7}_{-3.8}$	$11.8^{+1.9}_{-2.1}$	$6.3^{+1.4}_{-1.3}$	$3.2^{+1.0}_{-0.9}$
0b le3j Data	2728	766	257	77	32	9	9	4
1b le3j SM	$426^{+15}_{-17}$	$114^{+6}_{-6}$	$35.5^{+3.3}_{-2.8}$	$10.1^{+1.4}_{-1.5}$	$3.7^{+0.9}_{-0.8}$	$1.6^{+0.7}_{-0.6}$	$0.5^{+0.3}_{-0.4}$	$0.1^{+0.1}_{-0.0}$
1b le3j Data	444	118	36	15	3	2	1	0
2b le3j SM	$65.0^{+4.3}_{-4.3}$	$18.4^{+1.7}_{-1.6}$	$4.2^{+0.6}_{-0.5}$	$1.1^{+0.3}_{-0.2}$	$0.2^{+0.1}_{-0.1}$	$0.0^{+0.0}_{-0.0}$	$0.0^{+0.0}_{-0.0}$	$0.0^{+0.0}_{-0.0}$
2b le3j Data	78	18	8	3	0	0	0	0
0b ge4j SM	$456^{+15}_{-14}$	$291^{+12}_{-12}$	$148^{+8}_{-7}$	$66.0^{+5.6}_{-5.2}$	$27.1^{+2.9}_{-3.4}$	$14.0^{+1.9}_{-2.1}$	$6.5^{+1.5}_{-1.2}$	$3.2^{+1.0}_{-0.9}$
0b ge4j Data	480	299	158	66	28	15	6	2
1b ge4j SM	$190^{+10}_{-8}$	$120^{+6}_{-5}$	$45.6^{+3.1}_{-3.8}$	$17.1^{+2.6}_{-1.9}$	$6.8^{+1.5}_{-1.3}$	$5.4^{+1.3}_{-1.6}$	$2.4^{+0.9}_{-0.9}$	$1.2^{+0.7}_{-0.8}$
1b ge4j Data	206	135	45	14	8	6	2	0
2b ge4j SM	$73.6^{+4.2}_{-4.2}$	$45.7^{+2.8}_{-2.9}$	$20.4^{+1.8}_{-1.8}$	$7.7^{+1.2}_{-1.0}$	$1.9^{+0.3}_{-0.3}$	$0.9^{+0.2}_{-0.2}$	$0.4^{+0.1}_{-0.1}$	$0.4^{+0.1}_{-0.2}$
2b ge4j Data	79	52	31	12	1	2	0	1

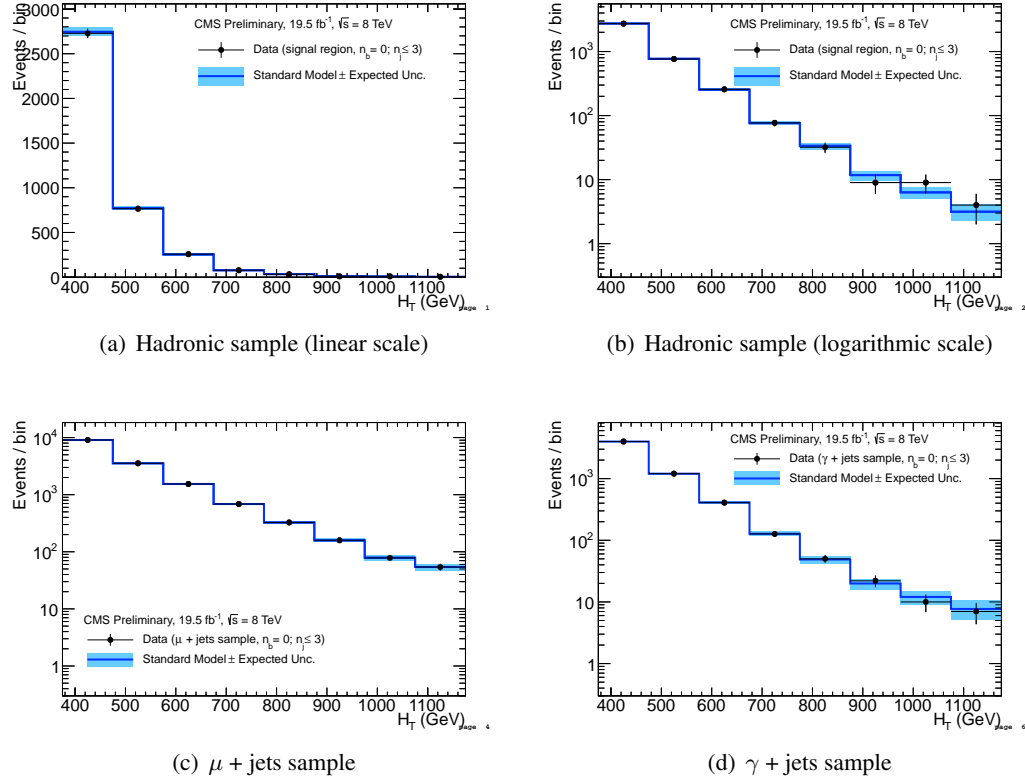
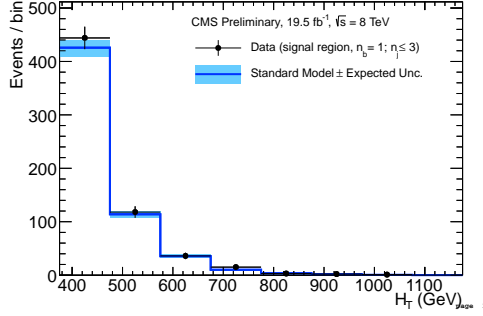
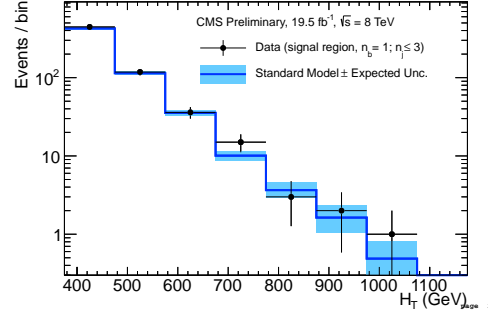


Figure 9.2: Comparison of the  $H_T$ -binned observed data yields and SM expectations when requiring  $2 \leq n_{\text{jet}} \leq 3$  and  $n_b = 0$  for the (a-b) hadronic, (c)  $\mu$  + jets, (d)  $\mu\mu$  + jets and (e)  $\gamma$  + jets samples, as determined by a simultaneous fit to all data samples under the SM-only hypothesis. The observed event yields in data (black dots) and the expectations and their uncertainties (dark blue solid line with light blue bands), as determined by the simultaneous fit, are shown. For illustrative purposes only, the signal expectations (pink dashed line) for the model T2cc with  $m_{\tilde{q}} = 250$  GeV and  $m_{\text{LSP}} = 240$  GeV are stacked on top of the SM expectations.



(a) Hadronic sample (linear scale)



(b) Hadronic sample (logarithmic scale)

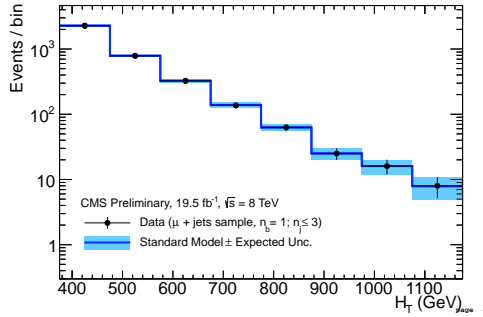
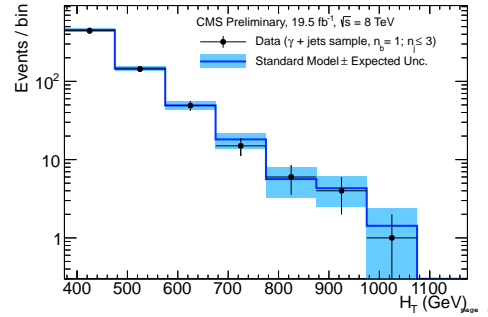
(c)  $\mu$  + jets sample(d)  $\gamma$  + jets sample

Figure 9.3: Comparison of the  $H_T$ -binned observed data yields and SM expectations when requiring  $2 \leq n_{\text{jet}} \leq 3$  and  $n_b = 1$  for the (a-b) hadronic, (c)  $\mu$  + jets, (d)  $\mu\mu$  + jets and (e)  $\gamma$  + jets samples, as determined by a simultaneous fit to all data samples under the SM-only hypothesis. The observed event yields in data (black dots) and the expectations and their uncertainties (dark blue solid line with light blue bands), as determined by the simultaneous fit, are shown. For illustrative purposes only, the signal expectations (pink dashed line) for the model T2cc with  $m_{\tilde{q}} = 250$  GeV and  $m_{\text{LSP}} = 170$  GeV are stacked on top of the SM expectations.

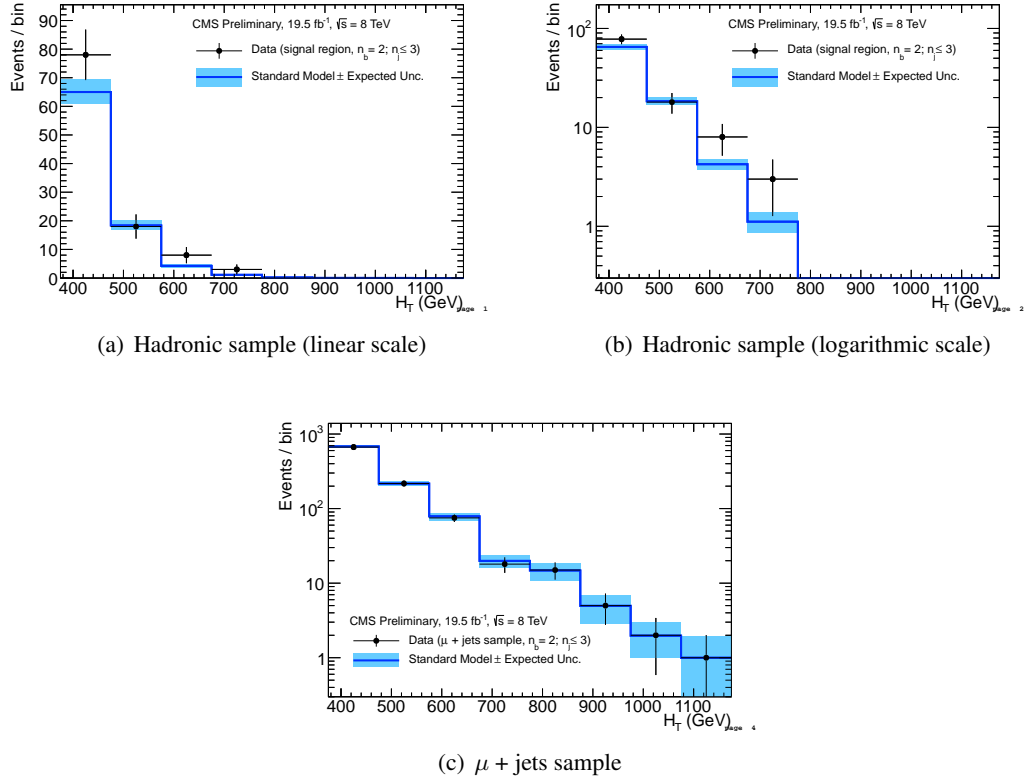
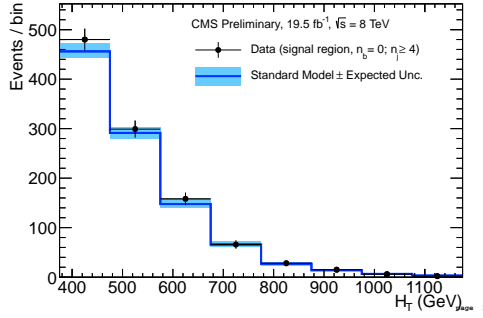
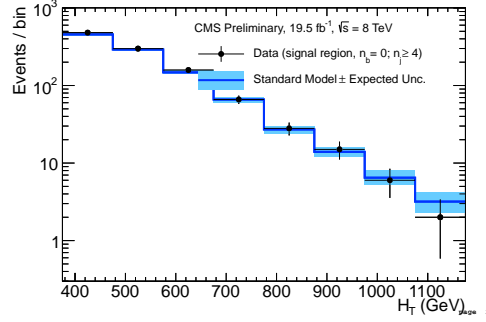


Figure 9.4: Comparison of the  $H_T$ -binned observed data yields and SM expectations when requiring  $2 \leq n_{\text{jet}} \leq 3$  and  $n_b = 2$  for the (a-b) hadronic and  $\mu$  + jets samples, as determined by a simultaneous fit to both the hadronic and  $\mu$  + jets data samples under the SM-only hypothesis. The observed event yields in data (black dots) and the expectations and their uncertainties (dark blue solid line with light blue bands), as determined by the simultaneous fit, are shown.



(a) Hadronic sample (linear scale)



(b) Hadronic sample (logarithmic scale)

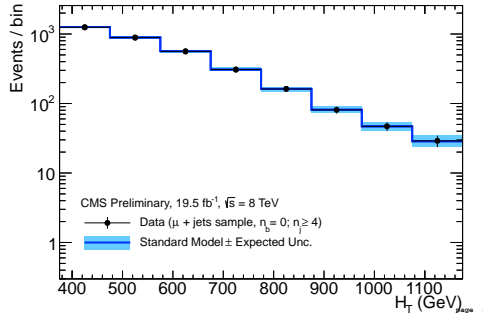
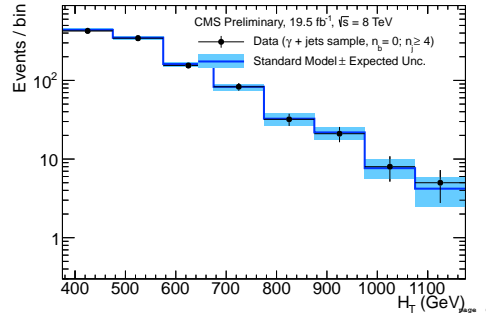
(c)  $\mu$  + jets sample(d)  $\gamma$  + jets sample

Figure 9.5: Comparison of the  $H_T$ -binned observed data yields and SM expectations when requiring  $n_{\text{jet}} \geq 4$  and  $n_b = 0$  for the (a-b) hadronic, (c)  $\mu$  + jets, (d)  $\mu\mu$  + jets and (e)  $\gamma$  + jets samples, as determined by a simultaneous fit to all data samples under the SM-only hypothesis. The observed event yields in data (black dots) and the expectations and their uncertainties (dark blue solid line with light blue bands), as determined by the simultaneous fit, are shown. For illustrative purposes only, the signal expectations (pink dashed line) for the model T2cc with  $m_{\tilde{q}} = 250$  GeV and  $m_{\text{LSP}} = 170$  GeV are stacked on top of the SM expectations.

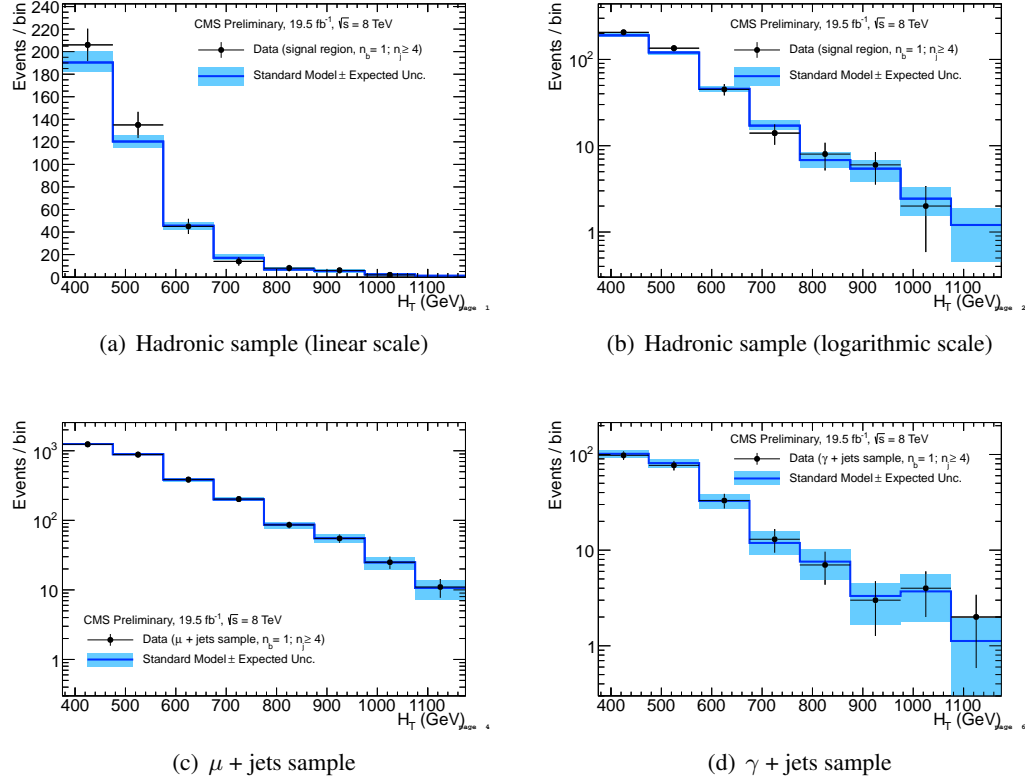


Figure 9.6: Comparison of the  $H_T$ -binned observed data yields and SM expectations when requiring  $n_{\text{jet}} \geq 4$  and  $n_b = 1$  for the (a-b) hadronic, (c)  $\mu$  + jets, (d)  $\mu\mu$  + jets and (e)  $\gamma$  + jets samples, as determined by a simultaneous fit to all data samples under the SM-only hypothesis. The observed event yields in data (black dots) and the expectations and their uncertainties (dark blue solid line with light blue bands), as determined by the simultaneous fit, are shown. For illustrative purposes only, the signal expectations (pink dashed line) for the model T2cc with  $m_{\tilde{q}} = 250$  GeV and  $m_{\text{LSP}} = 170$  GeV are stacked on top of the SM expectations.

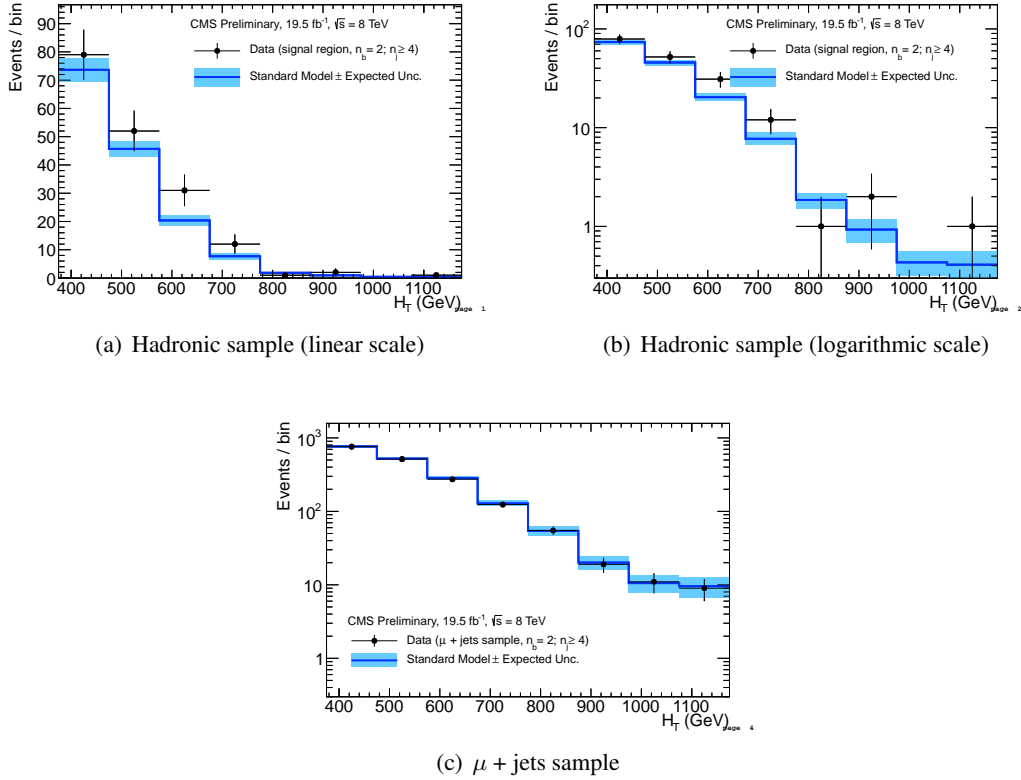


Figure 9.7: Comparison of the  $H_T$ -binned observed data yields and SM expectations when requiring  $n_{jet} \geq 4$  and  $n_b = 2$  for the (a-b) hadronic and  $\mu$  + jets samples, as determined by a simultaneous fit to both the hadronic and  $\mu$  + jets data samples under the SM-only hypothesis. The observed event yields in data (black dots) and the expectations and their uncertainties (dark blue solid line with light blue bands), as determined by the simultaneous fit, are shown.

## 10 Signal models and efficiencies

### 10.1 Introduction

As described in section 2.2, SUSY is a theory of many particles and parameters. In order to provide experiments with clear detectable signatures to search for, simplified models (SMS) have been derived [51–53] which reduce both particles and parameters. In this work, the results are interpreted in two SMS models:

- T2cc: pair produced stop sparticles each decaying into a charm quark and a neutralino
- T2tt: pair produced stop sparticles each decaying into a top quark and a neutralino.

The feynman diagrams for both models are shown in figures 2.4. SMS MC samples are generated at leading order with MADGRAPH [54] by the CMS SUSY MC group and binned in stop mass ( $m_{\text{Stop}}$ ) and neutralino mass ( $m_{\text{LSP}}$ ). The analysis efficiency is studied in the usual  $n_{\text{jet}}$ ,  $n_b$ ,  $H_T$ , binning but due to computational limitations not all categories are used to set a limit on a given model. The choice of categories for a model is made by computing the expected upper limit on the signal cross-section for each category separately. The categories are ranked by their expected upper limit. Depending on the number of mass bins and number of events per bin, two or more categories with the highest rank are chosen. The simplified models, along with the event categories considered for each, is summarized in Table 16.

Table 16: A summary of the simplified models considered for interpretation. The event categories considered for each model are listed.

Model	Production/decay mode	$(n_{\text{jet}}, n_b)$ event categories considered
T2cc	$pp \rightarrow \tilde{t}\tilde{t}^* \rightarrow c\tilde{\chi}^0 \bar{c}\tilde{\chi}^0$	$(2-3,0), (\geq 4,0), (\geq 4,1)$
T2tt	$pp \rightarrow \tilde{t}\tilde{t}^* \rightarrow t\tilde{\chi}^0 \bar{t}\tilde{\chi}^0$	$(\geq 4,1), (\geq 4,2)$



## 10.2 Efficiency times acceptance

The signal efficiency times acceptance is measured in the same binning as the analysis binning ( $n_{\text{jet}}, n_b, H_T$ ). To reduce the number of figures in this section to a manageable level, only the total efficiency for the relevant event categories and inclusive selection on  $H_T$  ( $> 375$  GeV) is shown. Figures 10.1 and 10.2 show the expected signal efficiency times acceptance for the hadronic selection the T2cc and T2tt interpretations for categories of interest.

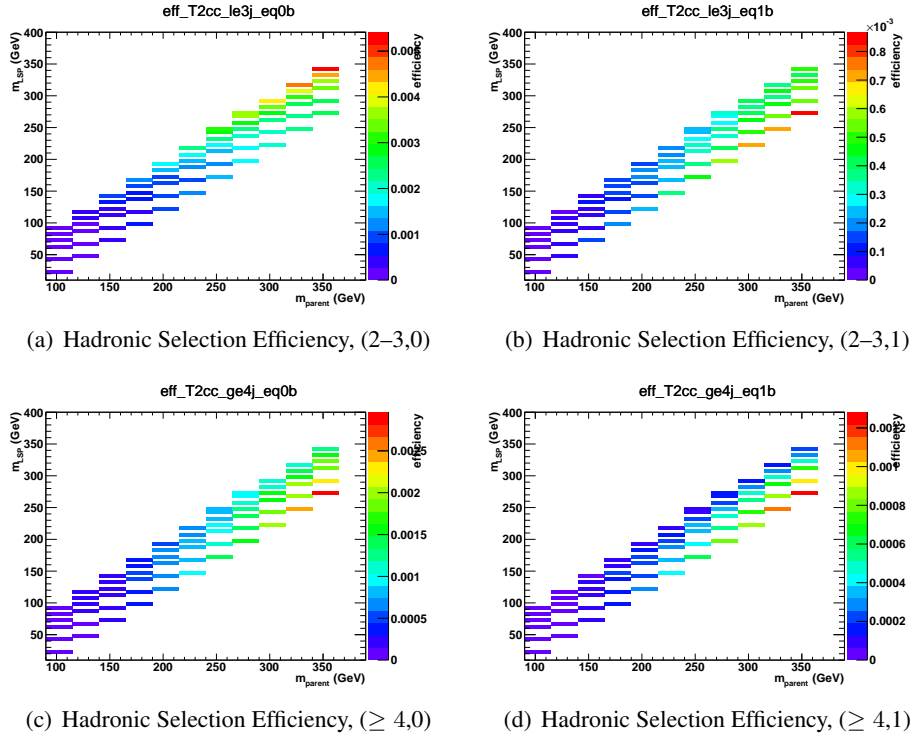


Figure 10.1: Hadronic selection efficiency times acceptance for T2cc for the relevant event categories defined by  $n_{\text{jet}}$  and  $n_b$ . Note the different z-axis scales.

In T2cc, the decay quarks become virtually undetectable as the nearly degenerate parent and daughter masses leave little energy for the decay products. Therefore any analysis interpreting in the T2cc model relies on hard- $p_T$  jets from initial state radiation for acceptance. The efficiency times acceptance is below the percent level where The largest efficiencies for the

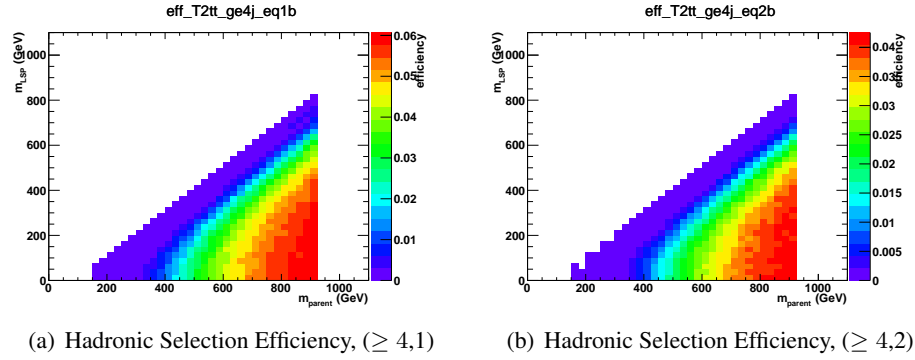


Figure 10.2: Hadronic selection efficiency times acceptance for the T2tt for the relevant event categories defined by  $n_{\text{jet}}$  and  $n_b$ . Note the different z-axis scales.

smallest mass splittings,  $\Delta M = \sim 10$  GeV, are obtained with the (2–3,0) category, while for larger mass splittings the (2–3,1), ( $\geq 4,0$ ), and ( $\geq 4,1$ ) categories contribute due to the reduced backgrounds in these categories. In T2tt the largest efficiencies are obtained in largest mass splittings in both categories of interest. In both models, the signal efficiency in the  $\mu + \text{jets}$  control sample is negligible with respect to the signal region.

## 10.3 Systematic uncertainties on signal efficiency times acceptance

### 10.3.1 Introduction

To gain statistical power, The systematic uncertainty in the signal acceptance times efficiency is determined per mass point per event category ( $n_{\text{jet}}, n_{\text{b}}$ ), but inclusively in  $H_{\text{T}}$ . This section details the methods used to determine the magnitude of the systematic uncertainties to be applied. Four sources of uncertainty are measured: the jet energy scale, the parton distribution functions, initial state radiation and b-tag scale factors. Three other uncertainties are quoted: the uncertainty in the luminosity (2.6%) and trigger (5%) measurements and the “dead ECAL” filter (3 %) used in the candidate signal event selection. Each contribution is considered to be independent and all contributions are summed in quadrature to obtain a total systematic uncertainty per mass point per category.

The following sub-sections provide an overview of the various sources of uncertainty, before details on specific models are provided.

### 10.3.2 PDF uncertainties

The simulated signal events were produced with the CTEQ6L1 PDF set by default. As recommended by PDF4LHC [55], the uncertainty in signal efficiency due to knowledge of the PDFs is obtained by comparing the signal efficiency with that obtained with three newer alternative PDF sets: CT10, NNPDF2.1, and MSTW2008. Using the envelope formula in the reference, a single efficiency is calculated from the three alternate PDF sets.

Figures E.1 and E.6 (Appendix E) show the relative difference of the signal efficiency times acceptance for the central value of the envelope calculation and the nominal PDF (CTEQ6L1) set used to produce the signal samples. The relative difference is taken as a symmetric systematic uncertainty, which varies in absolute terms within the range 0–10% in both models depending on the category of interest.

### 10.3.3 Jet energy scale

Figures E.2 and E.7 (Appendix E) show the relative change in the signal efficiency times acceptance for the relevant categories for the T2cc and T2tt interpretations when varying the energy of all jets in an event up or down according to a  $p_T$ - and  $\eta$ -dependent jet energy scale uncertainty, as recommended by the JetMET POG. In T2cc, larger variations are observed for the higher jet multiplicity category, as the jets are softer for the same requirement on  $H_T$ . Also, the variations may increase with increasing mass splitting as additional (soft) jets from the decay become hard enough to move within acceptance. The variations in both signal models range between  $\sim 5\%$  and  $\sim 15\%$  for the low and high jet multiplicity, and are largely independent of parent and daughter sparticle mass.

### 10.3.4 Initial state radiation

Signal samples produced with MADGRAPH exhibit discrepancies that have been attributed to the mismodelling of initial state radiation. These discrepancies are corrected as recommended by the SUSY PAG [56]. As per prescription, events are reweighed according to the vectorial sum of the momenta of the pair-produced sparticles. The sparticle-system  $p_T$  dependent weights are summarized in Table 17. In addition to the central weight, further variations about the central weight according to the uncertainty in the weight is applied in order to determine the systematic uncertainty associated with the correction. The resulting systematic uncertainties are largest near the diagonal where selected events contain significant amounts of boost due to the presence of initial state radiation.

Figure E.3 and E.8 (Appendix E) shows the relative change in the signal efficiency times acceptance for the relevant categories for the T2cc and T2tt interpretation when varying up and down the sparticle system  $p_T$ -dependent corrections by their uncertainties. The largest variations, up to  $\sim 25\%$  are observed for the smallest mass splittings, when the reliance on ISR jets for acceptance is largest.

Table 17: Sparticle system  $p_T$  dependent corrections and systematic weight variations.

Sparticle system $p_T$ (GeV)	Central Weight	Systematic Variation
$0 < p_T < 120$	1.00	$\pm 0.0$
$120 < p_T < 150$	0.95	$\pm 0.05$
$150 < p_T < 250$	0.90	$\pm 0.10$
$p_T > 250$	0.80	$\pm 0.20$

### 10.3.5 b-tag scale factor corrections

The uncertainty on the btag scale factors described in section [REF] is calculated by varying the scale factors up and down by their uncertainty as described in Ref. [57].

Figure E.4 and E.9 (Appendix E) show the relative change in the signal efficiency times acceptance for the relevant categories for the T2cc and T2tt interpretations when varying up and down the scale-factor corrections by their uncertainties. The variations are anti-correlated for the two  $n_b$  categories used by this interpretation and are generally small, at the level of 1–5%, with respect to other contributions.

### 10.3.6 Total systematic uncertainties

A few mass bins exhibit large uncertainties compared to neighboring mass bins. This effect attributed to low statistics when calculating the signal efficiency times acceptance in that bin. In order to decouple systematic and statistical uncertainties, these values have been replaced with appropriate values (determined by neighboring bins) in the calculation of the total uncertainty. Hence, figures E.5 and E.5, representing the total systematic uncertainty in the T2cc and T2tt interpretations for relevant categories are devoid of such fluctuations.

Table 19 presents a *representative* range of values for the contribution to the total systematic uncertainty in the signal efficiency times acceptance for each relevant event category. An uncertainty of 2.6% in the integrated luminosity is also considered. An uncertainty of 5% from the trigger uncertainty measurement Figure E.5 shows the total systematic uncertainty in the T2cc mass plane for the relevant categories.

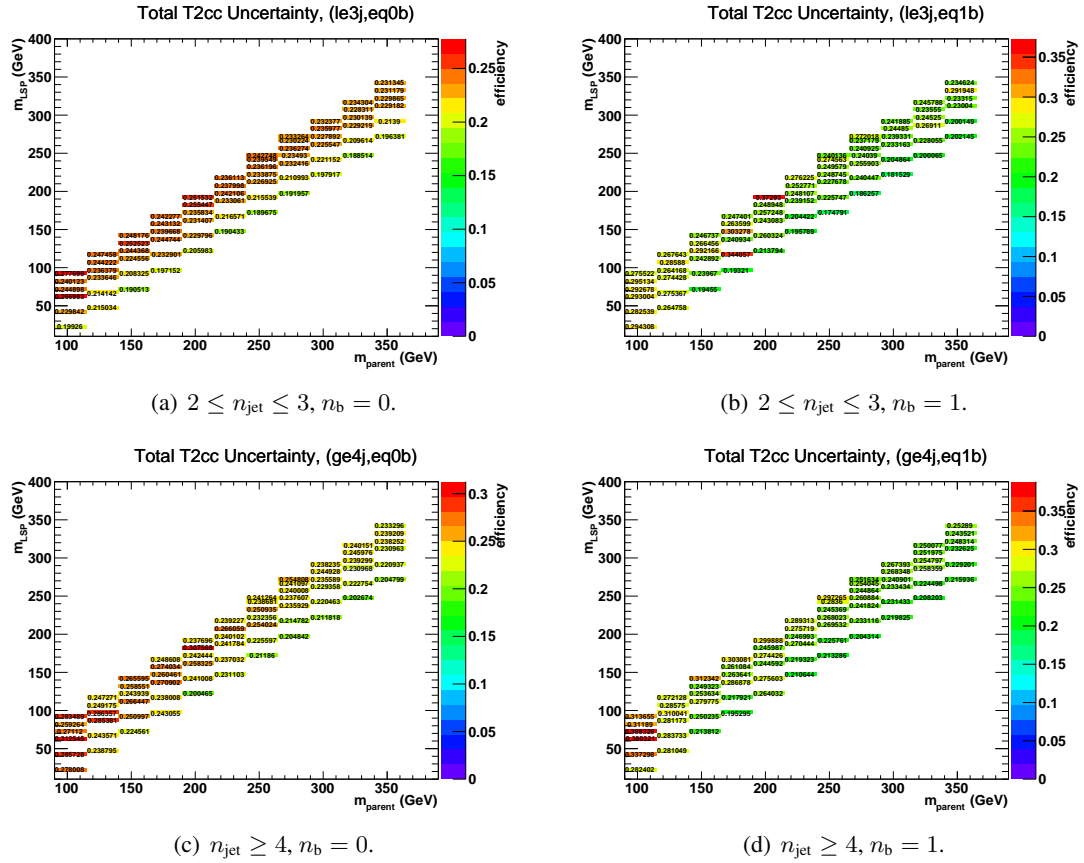


Figure 10.3: The total systematic uncertainty in the signal efficiency times acceptance for all relevant event categories for the T2cc interpretation.

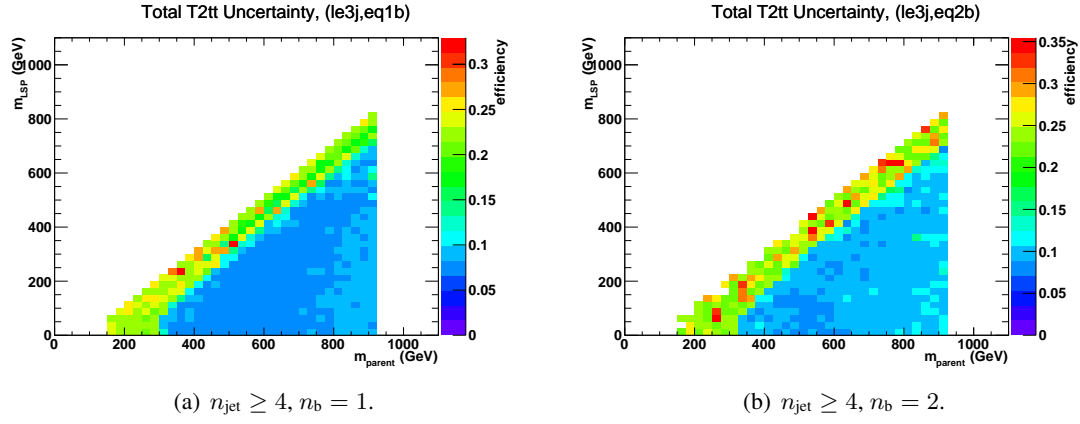


Figure 10.4: The total systematic uncertainty in the signal efficiency times acceptance for all relevant event categories for the T2tt interpretation.

Table 18: Representative ranges for each contribution to the total systematic uncertainty in the signal efficiency times acceptance for each relevant event category for the T2cc interpretation.

Category	(2–3,0)		(≥ 4,0)		(≥ 4,1)		(≥ 2,≥ 0)	
Range	Min.	Max.	Min.	Max.	Min.	Max.	Min.	Max.
PDF	0.00	0.05	0.00	0.05	0.00	0.10		
JES	0.00	0.10	0.00	0.10	0.00	0.15		
ISR	0.15	0.25	0.10	0.15	0.15	0.30		
b-tag SF	0.00	0.08	0.00	0.10	0.00	0.15		
Luminosity							0.026	0.026
Trigger							0.05	0.05
Dead Ecal							0.03	0.03
Total syst	0.18	0.25	0.19	0.30	0.20	0.38		

Table 19: Representative ranges for each contribution to the total systematic uncertainty in the signal efficiency times acceptance for each relevant event category for the T2tt interpretation.

Category	$(\geq 4,1)$		$(\geq 4,2)$		$(\geq 2,\geq 0)$	
Range	Min.	Max.	Min.	Max.	Min.	Max.
PDF	0.00	0.10	0.00	0.10		
JES	0.00	0.10	0.00	0.05		
ISR	0.00	0.20	0.00	0.22		
b-tag SF	0.00	0.05	0.00	0.10		
Luminosity					0.026	0.026
Trigger					0.05	0.05
Dead Ecal					0.03	0.03
Total syst	0.05	0.25	0.05	0.30		



## 11 Limits on SMS production cross sections

Upper limits on the production cross section of the two simplified SUSY models described in chapter 10 are discussed in this chapter.

### 11.1 Limit setting procedure

The following has been formulated in [58] and is summarized here for completeness. Consider the likelihood ratio [59]:

$$\lambda(\mu) = \frac{L(\mu, \hat{\vec{\theta}})}{L(\hat{\mu}, \hat{\vec{\theta}})} . \quad (29)$$

Where  $\hat{\vec{\theta}}$  in the numerator denotes the value of  $\vec{\theta}$ , the set of nuisance parameters in the likelihood, that maximizes  $L$  for the specified  $\mu$ . The denominator is the maximized likelihood function, i.e.,  $\hat{\mu}$  and  $\hat{\vec{\theta}}$  are their ML estimators. In the context of this analysis  $\mu \equiv f$  where  $f$  is the signal strength as defined in section 8.1.3. One can define the profile likelihood ratio test statistic as [59]:

$$q_\mu = \begin{cases} -2 \ln \lambda(\mu) & \hat{\mu} \leq \mu , \\ 0 & \hat{\mu} > \mu , \end{cases} \quad (30)$$

To test a specific signal model, one approach would be to perform many pseudo-experiments under the two separate hypotheses: background-only (i.e.  $\mu = 0$ ) and background with signal (i.e.  $\mu = 1$ ).  $CL_b$  and  $CL_{s+b}$  [60, 61] are defined as 1 - the quantile of  $q_{\mu(obs)}$  in each of these distributions, where  $q_{\mu(obs)}$  is the test statistic evaluated with the observed data. Figure 11.1 illustrates two example distributions of the test statistic under each hypothesis.  $CL_s$  is then defined as  $CL_s \equiv CL_{s+b}/CL_b$ , and a value  $CL_s < 0.05$  excludes the signal hypothesis at 95% confidence level.

Another approach is to instead calculate the upper limit on the signal cross section by

determining  $f$  at  $CL_s = 0.05$ . This approach samples CLs at varying signal strengths and the upper limit is determined through interpolation. If the upper limit on the cross section is lower than the theoretical cross section, the signal model is excluded.

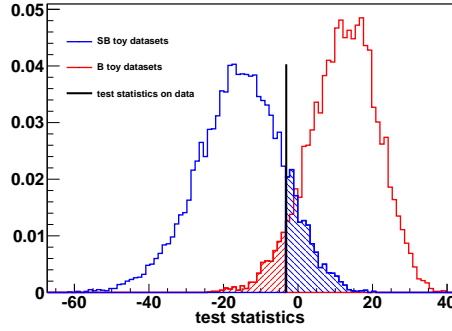


Figure 11.1: The distributions of the test statistic  $q_\mu$  in the background-only (red, on the right) and signal+background (blue, on the left) hypotheses. The black line represents the value of the  $q_\mu$  on the tested data. The shaded areas represent  $1 - CL_b$  (red) and  $CL_{s+b}$  (blue). From [62]

## 11.2 Upper limits on SMS models

For each mass-pair in a given model, the upper limit is calculated as described in section 11.1 using the likelihood constructed in section 8.1 by considering the relevant categories listed in table 16.

### 11.2.1 Upper limits on T2cc

The color scale in figure 11.2(a) shows the observed upper limit at 95% confidence level for each sparticle mass-pair bin in the SMS model where a stop particle decays to a charm quark and a neutralino (T2cc). The mass-pair bins left of the thick black curve have a calculated cross section upper limit below the theoretical production cross section, i.e.  $\frac{\sigma_{\text{obs. upper limit}}}{\sigma_{\text{theory}}} < 1$ , and are therefore excluded. The thinner black lines represent exclusion regions obtained by comparing the calculated upper limit with the theoretical cross section shifted up down and by

its theoretical uncertainty i.e.  $\frac{\sigma_{\text{obs. upper limit}}}{\sigma_{\text{theory} \pm \text{uncertainty}}} < 1$ . The dashed purple lines indicate the median (thick line)  $\pm 1\sigma$  (thin lines) expected exclusion regions. The  $\pm 1\sigma$  expected exclusion regions are not obtained by varying the theoretical cross section but rather by comparing the calculated expected upper limit  $\pm 1\sigma$  uncertainty with the nominal cross section. The observed upper limit curve lies within  $+1\sigma$  expected curve. For comparison, figure 11.2(b) shows similar exclusion limits obtained by the ATLAS collaboration [63] for the same model.

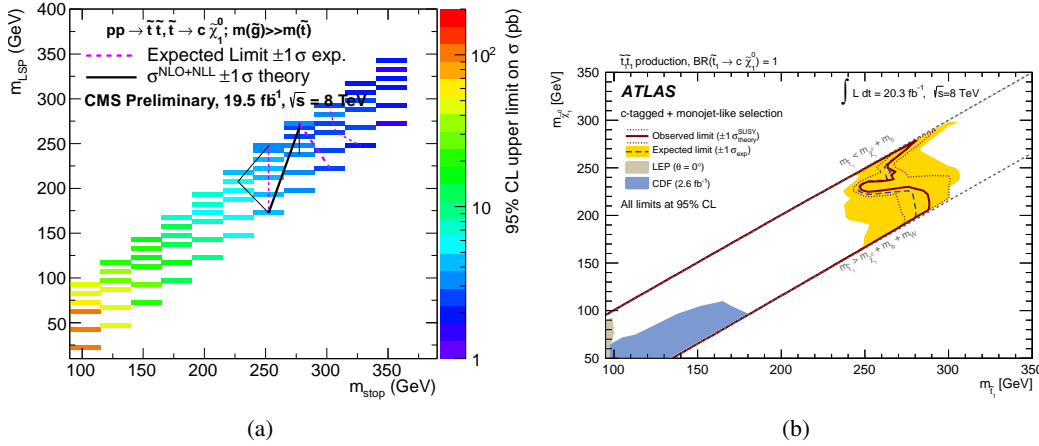


Figure 11.2: (a) shows the expected and observed upper limits on the production cross section for the model  $T2cc$  obtained in this analysis. See text for detail on each curve. (b) shows exclusion region in the same model obtained by the ATLAS collaboration, from [64]

### 11.2.2 Upper limits on $T2tt$

The color scale in figure 11.2.2 shows the observed upper limit at 95% confidence level for each sparticle mass-pair bin in the SMS model where a stop particle decays to a top quark and a neutralino ( $T2tt$ ). The definitions of the excluded regions remain the same as  $T2cc$ . The observed upper limit disagrees with the expected by more than  $2\sigma$ .

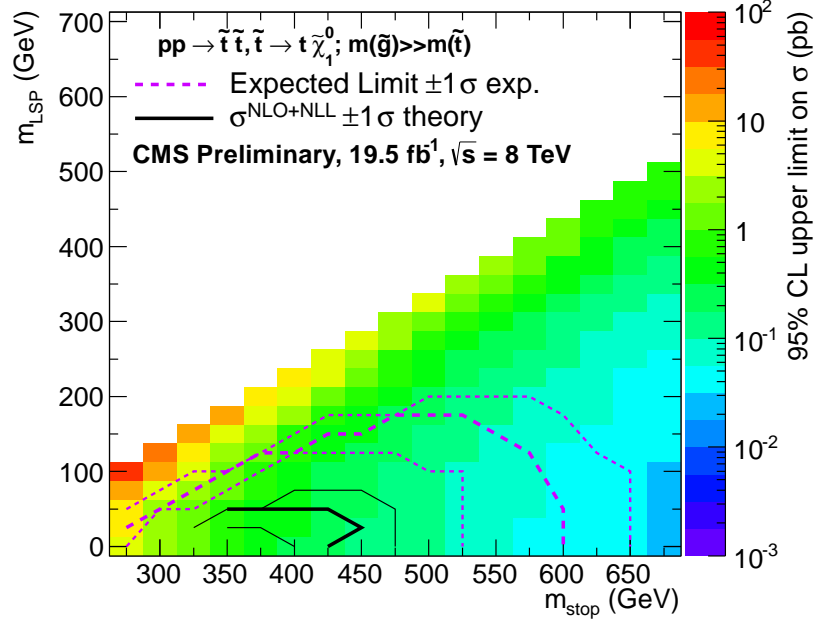


Figure 11.3: Expected and observed upper limits on the production cross section for the for the models T2tt (bottom).

It is instructive to re-examine the  $H_T$  bins which show the highest excesses when considering a SM-only hypotheses. To this intent, figure 9.1(b) of chapter 9 is re-plotted in figure 11.4 to isolate the categories used in interpreting T2tt. In the  $n_{\text{jet}} \geq 4$  and  $n_b = 2$  category,  $H_T$  bins 575 – 675 and 675 – 775 GeV show excesses of  $\sim 2.5\sigma$  and  $\sim 1.5\sigma$  respectively. In the  $n_{\text{jet}} \geq 4$  and  $n_b = 1$  category, the lowest two  $H_T$  bins are  $\sim 1.5\sigma$  from expectation. More generally, the categories used to interpret T2tt can be characterized by mild excesses in the lowest  $H_T$  bins and with a more pronounced excess in  $H_T = 575 \text{ GeV} - 675 \text{ GeV}$  in  $n_{\text{jet}} \geq 4$  and  $n_b = 2$  category. The discrepancy in the observed and expected limit is better understood with a closer study of the mass-pair bin ( $m_{\tilde{t}} = 400 \text{ GeV}$ ,  $m_{\text{LSP}} = 0 \text{ GeV}$ ), which is expected to be excluded but it is not by the observed data. It is useful to gauge the signal significance, defined here as the signal yield divided by  $\sqrt{b + (.1b)^2}$  where  $b$  is the SM expectation as determined by a simultaneous fit to all under the SM background hypothesis. Figure 11.5 plots the signal significance in bins of  $H_T$  and shows that most of the significance is expected in the lower  $H_T$  bins in both categories. Furthermore, figure 11.6 shows the  $H_T$ -binned observed

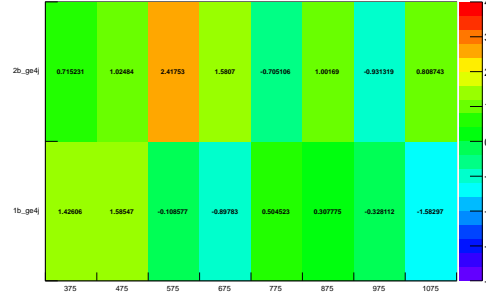


Figure 11.4: Pulls in categories used in T2cc interpretation.

data yields and expectations for the hadronic sample, as determined by a simultaneous fit to all data samples under a signal+background hypothesis. The signal under consideration remains  $m_{\tilde{t}} = 400$  GeV and  $m_{\text{LSP}} = 100$  GeV. The fit is performed simultaneously across both event categories. The plots give the indication that while the excesses in the low  $H_T$  bins are mild, they are enough to accommodate a signal-like excess. Finally, a profile likelihood ratio scan is performed as a function of signal strength to visualize the signal strength value best fitting the data and the upper limit on that signal strength at 95% confidence level.

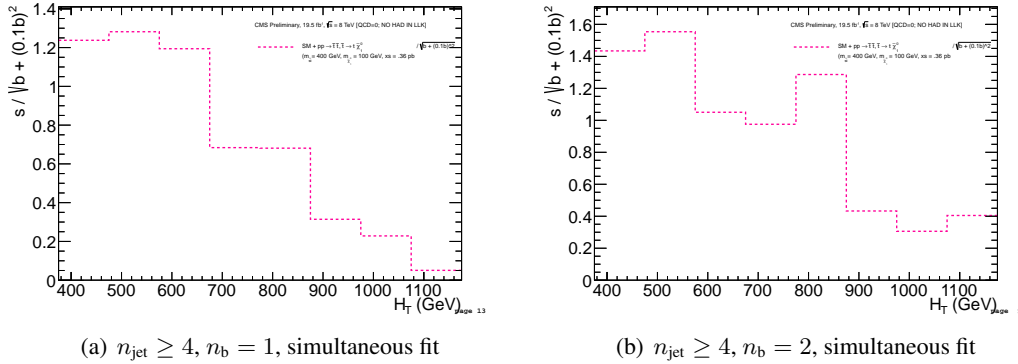


Figure 11.5: The  $H_T$ -binned signal significance defined as the signal yield divided by the  $\sqrt{b + (0.1b)^2}$  where  $b$  is the SM expectation obtained by a fit to all control data samples under the SM-only background hypothesis for the two categories (a)  $n_{\text{jet}} \geq 4, n_b = 1$  and (b)  $n_{\text{jet}} \geq 4, n_b = 2$  simultaneously. The signal model is T2tt with  $m_{\tilde{t}} = 400$  GeV and  $m_{\text{LSP}} = 100$  GeV.

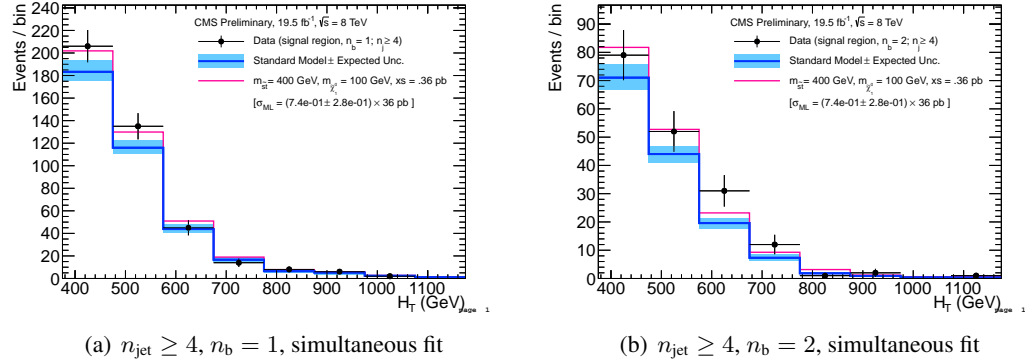


Figure 11.6: The comparison of the  $H_T$ -binned observed data yields and expectations for the hadronic sample, as determined by a simultaneous fit to all data samples under the signal plus SM background hypothesis. The observed event yields in data (black dots), the SM expectations (dark blue solid line), and the signal expectations (pink solid line), as determined by the simultaneous fit, for the signal model T2tt with  $m_{\tilde{t}} = 400$  GeV and  $m_{\text{LSP}} = 100$  GeV. Two event categories are considered: (a)  $n_{\text{jet}} \geq 4$  and  $n_b = 1$ , (b)  $n_{\text{jet}} \geq 4$  and  $n_b = 2$ .

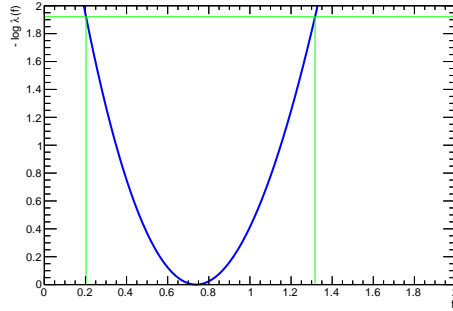


Figure 11.7: The profile likelihood ratio (defined in sec. 11.1) as a function of the signal strength. The likelihood considers all data samples under the signal plus SM background hypothesis for the signal model T2tt with  $m_{\tilde{t}} = 400$  GeV and  $m_{\text{LSP}} = 100$  GeV. The minimum defines the signal strength estimate which maximizes the likelihood and the green vertical line on the right of the minimum indicates the upper-limit at 95% confidence level.

## 11.3 Summary

Years of effort from thousands of people around the world has brought the LHC and CMS past through the phases of design, construction, and commission, to a successful physics run in 2012. Through a dedicated team of engineers and physicists, CMS recorded more than  $20 \text{ fb}^{-1}$  of data and which in the process allowed the confirmation of the existence of the Higgs boson. The spectacular efficiency of the detector also allowed searches beyond the Standard Model; this work presents such a search in events with jets and missing transverse energy. By using the variable  $\alpha_T$  the analysis effectively rejects multijet events stemming from QCD and mismeasured events. The remaining backgrounds are constrained using data samples which limit the reliance on Monte Carlo simulations. Though a slight excess is seen in some event categories, the observations are found to agree with the expectations of the Standard Model. The results are interpreted in two simplified supersymmetric models: (1) a pair-produced stop decays into a b quark jet, W boson, and a neutralino, (2) a pair-produced stop decays into a b quark, W boson and neutralino. In the latter model, exclusion limits comparable to other analyses are set.

## A Detailed example of background estimation

Consider the following bin:  $n_{\text{jet}} \geq 4$ ,  $n_b = 1$ ,  $375 \leq H_T \leq 475$ . The hadronic selection is run on the HTMHT dataset (the yield is denoted by  $N_{\text{obs}}^{\text{had}}$ ). The hadronic selection is also run on all SM MC datasets used in the analysis ( the yield is denoted by  $N_{\text{MC}}^{\text{had}} = N_W^{\text{had}} + N_{t\bar{t}}^{\text{had}} + N_{Z \rightarrow \nu\bar{\nu}}^{\text{had}} + N_{\text{DY}}^{\text{had}} + N_{\gamma}^{\text{had}} + N_{\text{top}}^{\text{had}} + N_{\text{di-boson}}^{\text{had}}$ ). It will be useful to split the total background into two components  $N_{\text{MC}}^{\text{had}} = N_{Z \rightarrow \nu\bar{\nu}}^{\text{had}} + N_{t\bar{t}W}^{\text{had}}$  where  $N_{t\bar{t}W}^{\text{had}}$  is the yield of all background except  $Z \rightarrow \nu\bar{\nu}$ .

Because  $n_b < 2$ , the photon control sample is used to predict the  $Z \rightarrow \nu\bar{\nu}$  background. The yields for the photon control sample are obtained by running the photon selection on the ‘‘SinglePhoton’’ dataset (the yield is symbolized by  $N_{\text{obs}}^{\gamma \text{ control}}$ ) and running the same photon selection on all SM MC datasets used in the analysis ( the yield is symbolized by  $N_{\text{MC}}^{\gamma \text{ control}} = N_W^{\gamma \text{ control}} + N_{t\bar{t}}^{\gamma \text{ control}} + N_{Z \rightarrow \nu\bar{\nu}}^{\gamma \text{ control}} + N_{\text{DY}}^{\gamma \text{ control}} + N_{\gamma}^{\gamma \text{ control}} + N_{\text{top}}^{\gamma \text{ control}} + N_{\text{di-boson}}^{\gamma \text{ control}}$ ). The background prediction is made by using the translation factor:

$$TF^{\gamma} = \frac{N_{Z \rightarrow \nu\bar{\nu}}^{\text{had}}}{N_{\text{MC}}^{\gamma \text{ control}}} \quad (31)$$

and the predicted  $Z \rightarrow \nu\bar{\nu}$  background is:

$$N_{\text{pre}, Z \rightarrow \nu\bar{\nu}}^{\text{had}} = TF^{\gamma} \times N_{\text{obs}}^{\gamma \text{ control}} \quad (32)$$

The rest of the background is predicted by the muon control sample. Analogously to the above, we run a muon selection on the ‘‘SingleMuon’’ dataset ( $N_{\text{obs}}^{\mu}$ ) and on the full suite of SM MC ( $N_{\text{MC}}^{\mu \text{ control}}$ ) The translation factor is

$$TF^{\mu} = \frac{N_{t\bar{t}W}^{\text{had}}}{N_{\text{MC}}^{\mu \text{ control}}} \quad (33)$$

and the predicted  $t\bar{t}W$  background is:

$$N_{\text{pre}, t\bar{t}W}^{\text{had}} = TF^{\mu} \times N_{\text{obs}}^{\mu \text{ control}} \quad (34)$$



the total background prediction is then:

$$N_{\text{pre}}^{\text{had}} = N_{\text{pre}, Z \rightarrow \nu \bar{\nu}}^{\text{had}} + N_{\text{pre}, t\bar{t}W}^{\text{had}} \quad (35)$$

## B Background estimation from control samples

Table 20: Photon Sample Predictions Normalized to  $19.5\text{fb}^{-1}$  ( $2 \leq n_{\text{jet}} \leq 3, n_b = 0$ )

$H_T$ Bin (GeV)	375–475	475–575	575–675	675–775
MC $Z \rightarrow \nu\bar{\nu}$	$1725.7 \pm 8.9_{\text{stat}}$	$571.8 \pm 3.9_{\text{stat}}$	$202.1 \pm 2.3_{\text{stat}}$	$78.0 \pm 1.4_{\text{stat}}$
MC $\gamma + \text{jets}$	$3721.1 \pm 32.4_{\text{stat}}$	$1303.9 \pm 18.2_{\text{stat}}$	$459.7 \pm 10.9_{\text{stat}}$	$185.4 \pm 6.9_{\text{stat}}$
MC Ratio (TF)	0.46	0.44	0.44	0.42
Data $\gamma + \text{jets}$	3951.3	1191.3	403.0	125.5
$Z \rightarrow \nu\bar{\nu}$ Prediction	$1832.5 \pm 29.0_{\text{stat}} \pm 109.9_{\text{syst}}$	$522.4 \pm 15.0_{\text{stat}} \pm 31.3_{\text{syst}}$	$177.1 \pm 8.8_{\text{stat}} \pm 12.4_{\text{syst}}$	$52.8 \pm 4.7_{\text{stat}} \pm 6.3_{\text{syst}}$
$H_T$ Bin (GeV)	775–875	875–975	975–1075	1075– $\infty$
MC $Z \rightarrow \nu\bar{\nu}$	$33.3 \pm 0.9_{\text{stat}}$	$13.3 \pm 0.6_{\text{stat}}$	$6.2 \pm 0.4_{\text{stat}}$	$2.8 \pm 0.3_{\text{stat}}$
MC $\gamma + \text{jets}$	$68.4 \pm 4.2_{\text{stat}}$	$27.9 \pm 2.7_{\text{stat}}$	$16.1 \pm 2.0_{\text{stat}}$	$8.2 \pm 1.5_{\text{stat}}$
MC Ratio (TF)	0.49	0.48	0.39	0.34
Data $\gamma + \text{jets}$	49.4	21.7	9.9	6.9
$Z \rightarrow \nu\bar{\nu}$ Prediction	$24.0 \pm 3.4_{\text{stat}} \pm 2.9_{\text{syst}}$	$10.4 \pm 2.2_{\text{stat}} \pm 1.8_{\text{syst}}$	$3.8 \pm 1.2_{\text{stat}} \pm 0.6_{\text{syst}}$	$2.3 \pm 0.9_{\text{stat}} \pm 0.4_{\text{syst}}$

Table 21: Muon Sample Predictions Normalized to  $19.5\text{fb}^{-1}$  ( $2 \leq n_{\text{jet}} \leq 3, n_b = 0$ )

$H_T$ Bin (GeV)	375–475	475–575	575–675	675–775
MC $W + t\bar{t}$	$1088.0 \pm 12.8_{\text{stat}}$	$294.9 \pm 6.1_{\text{stat}}$	$85.1 \pm 3.2_{\text{stat}}$	$27.7 \pm 1.8_{\text{stat}}$
MC $\mu + \text{jets}$	$9759.6 \pm 38.9_{\text{stat}}$	$4015.5 \pm 23.3_{\text{stat}}$	$1736.3 \pm 15.1_{\text{stat}}$	$810.2 \pm 10.1_{\text{stat}}$
MC Ratio (TF)	0.11	0.07	0.05	0.03
Data $\mu + \text{jets}$	8962.9	3500.1	1518.5	677.3
$W + t\bar{t}$ Prediction	$999.2 \pm 10.5_{\text{stat}} \pm 60.0_{\text{syst}}$	$257.1 \pm 4.3_{\text{stat}} \pm 15.4_{\text{syst}}$	$74.4 \pm 1.9_{\text{stat}} \pm 5.2_{\text{syst}}$	$23.1 \pm 0.9_{\text{stat}} \pm 2.8_{\text{syst}}$
$H_T$ Bin (GeV)	775–875	875–975	975–1075	1075– $\infty$
MC $W + t\bar{t}$	$12.8 \pm 1.2_{\text{stat}}$	$3.8 \pm 0.6_{\text{stat}}$	$2.1 \pm 0.5_{\text{stat}}$	$0.7 \pm 0.3_{\text{stat}}$
MC $\mu + \text{jets}$	$386.8 \pm 6.8_{\text{stat}}$	$208.1 \pm 4.9_{\text{stat}}$	$113.7 \pm 3.7_{\text{stat}}$	$65.8 \pm 2.7_{\text{stat}}$
MC Ratio (TF)	0.03	0.02	0.02	0.01
Data $\mu + \text{jets}$	321.9	157.0	77.0	53.3
$W + t\bar{t}$ Prediction	$10.7 \pm 0.6_{\text{stat}} \pm 1.3_{\text{syst}}$	$2.9 \pm 0.2_{\text{stat}} \pm 0.5_{\text{syst}}$	$1.5 \pm 0.2_{\text{stat}} \pm 0.2_{\text{syst}}$	$0.6 \pm 0.1_{\text{stat}} \pm 0.1_{\text{syst}}$

Table 22: Photon Sample Predictions Normalized to  $19.5\text{fb}^{-1}$  ( $n_{\text{jet}} \geq 4, n_{\text{b}} = 0$ )

$H_{\text{T}}$ Bin (GeV)	375–475	475–575	575–675	675–775
MC $Z \rightarrow \nu\bar{\nu}$	$211.0 \pm 3.4_{\text{stat}}$	$158.7 \pm 2.2_{\text{stat}}$	$85.8 \pm 1.5_{\text{stat}}$	$40.4 \pm 1.0_{\text{stat}}$
MC $\gamma + \text{jets}$	$402.1 \pm 10.8_{\text{stat}}$	$314.3 \pm 9.0_{\text{stat}}$	$157.8 \pm 6.4_{\text{stat}}$	$79.3 \pm 4.5_{\text{stat}}$
MC Ratio (TF)	0.52	0.51	0.54	0.51
Data $\gamma + \text{jets}$	421.8	339.8	153.1	82.0
$Z \rightarrow \nu\bar{\nu}$ Prediction	$221.4 \pm 10.7_{\text{stat}} \pm 13.3_{\text{syst}}$	$171.6 \pm 9.3_{\text{stat}} \pm 10.3_{\text{syst}}$	$83.2 \pm 6.7_{\text{stat}} \pm 6.7_{\text{syst}}$	$41.8 \pm 4.6_{\text{stat}} \pm 5.8_{\text{syst}}$
$H_{\text{T}}$ Bin (GeV)	775–875	875–975	975–1075	1075– $\infty$
MC $Z \rightarrow \nu\bar{\nu}$	$18.5 \pm 0.7_{\text{stat}}$	$8.2 \pm 0.5_{\text{stat}}$	$4.7 \pm 0.3_{\text{stat}}$	$2.4 \pm 0.2_{\text{stat}}$
MC $\gamma + \text{jets}$	$31.4 \pm 2.9_{\text{stat}}$	$17.7 \pm 2.2_{\text{stat}}$	$7.4 \pm 1.4_{\text{stat}}$	$4.5 \pm 1.0_{\text{stat}}$
MC Ratio (TF)	0.59	0.46	0.64	0.53
Data $\gamma + \text{jets}$	31.6	20.7	7.9	4.9
$Z \rightarrow \nu\bar{\nu}$ Prediction	$18.6 \pm 3.3_{\text{stat}} \pm 2.6_{\text{syst}}$	$9.6 \pm 2.1_{\text{stat}} \pm 1.3_{\text{syst}}$	$5.0 \pm 1.8_{\text{stat}} \pm 0.7_{\text{syst}}$	$2.6 \pm 1.2_{\text{stat}} \pm 0.6_{\text{syst}}$

Table 23: Muon Sample Predictions Normalized to  $19.5\text{fb}^{-1}$  ( $n_{\text{jet}} \geq 4, n_{\text{b}} = 0$ )

$H_{\text{T}}$ Bin (GeV)	375–475	475–575	575–675	675–775
MC $W + t\bar{t}$	$223.2 \pm 6.4_{\text{stat}}$	$134.3 \pm 4.5_{\text{stat}}$	$58.0 \pm 2.8_{\text{stat}}$	$25.1 \pm 1.8_{\text{stat}}$
MC $\mu + \text{jets}$	$1322.2 \pm 15.8_{\text{stat}}$	$1041.8 \pm 18.0_{\text{stat}}$	$574.7 \pm 9.6_{\text{stat}}$	$315.7 \pm 14.1_{\text{stat}}$
MC Ratio (TF)	0.17	0.13	0.10	0.08
Data $\mu + \text{jets}$	1233.2	876.7	554.9	304.1
$W + t\bar{t}$ Prediction	$208.1 \pm 5.9_{\text{stat}} \pm 12.5_{\text{syst}}$	$113.1 \pm 3.8_{\text{stat}} \pm 6.8_{\text{syst}}$	$56.0 \pm 2.4_{\text{stat}} \pm 4.5_{\text{syst}}$	$24.1 \pm 1.4_{\text{stat}} \pm 3.4_{\text{syst}}$
$H_{\text{T}}$ Bin (GeV)	775–875	875–975	975–1075	1075– $\infty$
MC $W + t\bar{t}$	$8.7 \pm 1.0_{\text{stat}}$	$4.3 \pm 0.8_{\text{stat}}$	$2.0 \pm 0.5_{\text{stat}}$	$1.2 \pm 0.4_{\text{stat}}$
MC $\mu + \text{jets}$	$175.4 \pm 5.2_{\text{stat}}$	$91.3 \pm 3.8_{\text{stat}}$	$53.8 \pm 2.9_{\text{stat}}$	$31.4 \pm 2.3_{\text{stat}}$
MC Ratio (TF)	0.05	0.05	0.04	0.04
Data $\mu + \text{jets}$	159.9	80.0	46.4	28.6
$W + t\bar{t}$ Prediction	$7.9 \pm 0.6_{\text{stat}} \pm 1.1_{\text{syst}}$	$3.8 \pm 0.4_{\text{stat}} \pm 0.5_{\text{syst}}$	$1.7 \pm 0.2_{\text{stat}} \pm 0.2_{\text{syst}}$	$1.1 \pm 0.2_{\text{stat}} \pm 0.2_{\text{syst}}$

Table 24: Photon Sample Predictions Normalized to  $19.5\text{fb}^{-1}$  ( $2 \leq n_{\text{jet}} \leq 3, n_{\text{b}} = 1$ )

$H_{\text{T}}$ Bin (GeV)	375–475	475–575	575–675	675–775
MC $Z \rightarrow \nu\bar{\nu}$	$155.7 \pm 2.7_{\text{stat}}$	$54.2 \pm 1.3_{\text{stat}}$	$19.5 \pm 0.8_{\text{stat}}$	$6.6 \pm 0.4_{\text{stat}}$
MC $\gamma + \text{jets}$	$360.0 \pm 10.2_{\text{stat}}$	$126.4 \pm 5.9_{\text{stat}}$	$47.0 \pm 3.6_{\text{stat}}$	$19.0 \pm 2.3_{\text{stat}}$
MC Ratio (TF)	0.43	0.43	0.41	0.34
Data $\gamma + \text{jets}$	438.6	142.2	48.4	14.8
$Z \rightarrow \nu\bar{\nu}$ Prediction	$189.7 \pm 9.0_{\text{stat}} \pm 11.4_{\text{syst}}$	$61.0 \pm 5.1_{\text{stat}} \pm 3.7_{\text{syst}}$	$20.1 \pm 2.9_{\text{stat}} \pm 1.4_{\text{syst}}$	$5.1 \pm 1.3_{\text{stat}} \pm 0.6_{\text{syst}}$
$H_{\text{T}}$ Bin (GeV)	775–875	875–975	975–1075	1075– $\infty$
MC $Z \rightarrow \nu\bar{\nu}$	$2.9 \pm 0.3_{\text{stat}}$	$1.4 \pm 0.2_{\text{stat}}$	$0.5 \pm 0.1_{\text{stat}}$	$0.3 \pm 0.1_{\text{stat}}$
MC $\gamma + \text{jets}$	$8.1 \pm 1.5_{\text{stat}}$	$4.7 \pm 1.2_{\text{stat}}$	$1.8 \pm 0.7_{\text{stat}}$	$1.0 \pm 0.5_{\text{stat}}$
MC Ratio (TF)	0.36	0.31	0.28	0.28
Data $\gamma + \text{jets}$	5.9	4.0	1.0	0.0
$Z \rightarrow \nu\bar{\nu}$ Prediction	$2.2 \pm 0.9_{\text{stat}} \pm 0.3_{\text{syst}}$	$1.2 \pm 0.6_{\text{stat}} \pm 0.2_{\text{syst}}$	$0.3 \pm 0.4_{\text{stat}} \pm 0.0_{\text{syst}}$	$0.0 \pm 0.3_{\text{stat}}$

Table 25: Muon Sample Predictions Normalized to  $19.5\text{fb}^{-1}$  ( $2 \leq n_{\text{jet}} \leq 3, n_b = 1$ )

$H_T$ Bin (GeV)	375–475	475–575	575–675	675–775
MC W + $t\bar{t}$	$214.4 \pm 6.3_{\text{stat}}$	$51.8 \pm 3.0_{\text{stat}}$	$15.5 \pm 1.7_{\text{stat}}$	$3.9 \pm 0.7_{\text{stat}}$
MC $\mu$ + jets	$2200.8 \pm 21.7_{\text{stat}}$	$788.0 \pm 12.6_{\text{stat}}$	$325.9 \pm 8.1_{\text{stat}}$	$148.3 \pm 5.6_{\text{stat}}$
MC Ratio (TF)	0.10	0.07	0.05	0.03
Data $\mu$ + jets	2243.2	777.0	320.9	135.3
W + $t\bar{t}$ Prediction	$218.5 \pm 4.6_{\text{stat}} \pm 13.1_{\text{syst}}$	$51.1 \pm 1.8_{\text{stat}} \pm 3.1_{\text{syst}}$	$15.3 \pm 0.8_{\text{stat}} \pm 1.1_{\text{syst}}$	$3.5 \pm 0.3_{\text{stat}} \pm 0.4_{\text{syst}}$
$H_T$ Bin (GeV)	775–875	875–975	975–1075	1075– $\infty$
MC W + $t\bar{t}$	$1.9 \pm 0.5_{\text{stat}}$	$0.5 \pm 0.2_{\text{stat}}$	$0.1 \pm 0.1_{\text{stat}}$	$0.1 \pm 0.1_{\text{stat}}$
MC $\mu$ + jets	$70.2 \pm 3.8_{\text{stat}}$	$39.7 \pm 2.9_{\text{stat}}$	$20.6 \pm 1.9_{\text{stat}}$	$9.2 \pm 1.3_{\text{stat}}$
MC Ratio (TF)	0.03	0.01	0.01	0.02
Data $\mu$ + jets	62.2	24.7	15.8	7.9
W + $t\bar{t}$ Prediction	$1.7 \pm 0.2_{\text{stat}} \pm 0.2_{\text{syst}}$	$0.3 \pm 0.1_{\text{stat}} \pm 0.1_{\text{syst}}$	$0.1 \pm 0.0_{\text{stat}} \pm 0.0_{\text{syst}}$	$0.1 \pm 0.0_{\text{stat}} \pm 0.0_{\text{syst}}$

Table 26: Photon Sample Predictions Normalized to  $19.5\text{fb}^{-1}$  ( $n_{\text{jet}} \geq 4, n_b = 1$ )

$H_T$ Bin (GeV)	375–475	475–575	575–675	675–775
MC $Z \rightarrow \nu\bar{\nu}$	$29.5 \pm 1.3_{\text{stat}}$	$24.1 \pm 0.9_{\text{stat}}$	$12.7 \pm 0.6_{\text{stat}}$	$5.9 \pm 0.4_{\text{stat}}$
MC $\gamma$ + jets	$68.4 \pm 4.5_{\text{stat}}$	$55.4 \pm 3.9_{\text{stat}}$	$23.5 \pm 2.5_{\text{stat}}$	$11.2 \pm 1.7_{\text{stat}}$
MC Ratio (TF)	0.43	0.43	0.54	0.53
Data $\gamma$ + jets	96.8	76.1	32.6	12.8
$Z \rightarrow \nu\bar{\nu}$ Prediction	$41.8 \pm 4.2_{\text{stat}} \pm 2.5_{\text{syst}}$	$33.0 \pm 3.8_{\text{stat}} \pm 2.0_{\text{syst}}$	$17.7 \pm 3.1_{\text{stat}} \pm 1.4_{\text{syst}}$	$6.8 \pm 1.9_{\text{stat}} \pm 0.9_{\text{syst}}$
$H_T$ Bin (GeV)	775–875	875–975	975–1075	1075– $\infty$
MC $Z \rightarrow \nu\bar{\nu}$	$3.2 \pm 0.3_{\text{stat}}$	$1.8 \pm 0.2_{\text{stat}}$	$0.6 \pm 0.1_{\text{stat}}$	$0.3 \pm 0.1_{\text{stat}}$
MC $\gamma$ + jets	$7.2 \pm 1.3_{\text{stat}}$	$1.9 \pm 0.7_{\text{stat}}$	$1.2 \pm 0.6_{\text{stat}}$	$0.4 \pm 0.3_{\text{stat}}$
MC Ratio (TF)	0.44	0.95	0.47	0.81
Data $\gamma$ + jets	6.9	3.0	4.0	2.0
$Z \rightarrow \nu\bar{\nu}$ Prediction	$3.1 \pm 1.2_{\text{stat}} \pm 0.4_{\text{syst}}$	$2.8 \pm 1.6_{\text{stat}} \pm 0.4_{\text{syst}}$	$1.9 \pm 0.9_{\text{stat}} \pm 0.3_{\text{syst}}$	$1.6 \pm 1.1_{\text{stat}} \pm 0.3_{\text{syst}}$

Table 27: Muon Sample Predictions Normalized to  $19.5\text{fb}^{-1}$  ( $n_{\text{jet}} \geq 4, n_b = 1$ )

$H_T$ Bin (GeV)	375–475	475–575	575–675	675–775
MC W + $t\bar{t}$	$142.3 \pm 5.5_{\text{stat}}$	$82.1 \pm 4.0_{\text{stat}}$	$35.2 \pm 2.6_{\text{stat}}$	$14.0 \pm 1.6_{\text{stat}}$
MC $\mu$ + jets	$1248.7 \pm 23.2_{\text{stat}}$	$881.7 \pm 14.1_{\text{stat}}$	$474.2 \pm 10.2_{\text{stat}}$	$241.8 \pm 7.2_{\text{stat}}$
MC Ratio (TF)	0.11	0.09	0.07	0.06
Data $\mu$ + jets	1222.3	869.8	380.1	199.4
W + $t\bar{t}$ Prediction	$139.3 \pm 4.0_{\text{stat}} \pm 8.4_{\text{syst}}$	$81.0 \pm 2.7_{\text{stat}} \pm 4.9_{\text{syst}}$	$28.2 \pm 1.4_{\text{stat}} \pm 2.3_{\text{syst}}$	$11.5 \pm 0.8_{\text{stat}} \pm 1.6_{\text{syst}}$
$H_T$ Bin (GeV)	775–875	875–975	975–1075	1075– $\infty$
MC W + $t\bar{t}$	$5.1 \pm 1.0_{\text{stat}}$	$2.6 \pm 0.6_{\text{stat}}$	$1.1 \pm 0.4_{\text{stat}}$	$0.7 \pm 0.3_{\text{stat}}$
MC $\mu$ + jets	$126.6 \pm 5.1_{\text{stat}}$	$63.2 \pm 3.8_{\text{stat}}$	$36.0 \pm 2.8_{\text{stat}}$	$20.2 \pm 2.1_{\text{stat}}$
MC Ratio (TF)	0.04	0.04	0.03	0.03
Data $\mu$ + jets	84.9	54.3	24.7	10.9
W + $t\bar{t}$ Prediction	$3.4 \pm 0.4_{\text{stat}} \pm 0.5_{\text{syst}}$	$2.3 \pm 0.3_{\text{stat}} \pm 0.3_{\text{syst}}$	$0.7 \pm 0.1_{\text{stat}} \pm 0.1_{\text{syst}}$	$0.4 \pm 0.1_{\text{stat}} \pm 0.1_{\text{syst}}$

Table 28: Muon Sample Predictions Normalized to  $19.5\text{fb}^{-1}$  ( $2 \leq n_{\text{jet}} \leq 3, n_{\text{b}} = 2$ )

$H_{\text{T}}$ Bin (GeV)	375–475	475–575	575–675	675–775
MC W + $t\bar{t}$	$46.7 \pm 2.9_{\text{stat}}$	$12.6 \pm 1.6_{\text{stat}}$	$3.1 \pm 0.8_{\text{stat}}$	$1.4 \pm 0.5_{\text{stat}}$
MC $\mu$ + jets	$670.0 \pm 12.0_{\text{stat}}$	$208.0 \pm 6.6_{\text{stat}}$	$84.2 \pm 4.2_{\text{stat}}$	$31.3 \pm 2.7_{\text{stat}}$
MC Ratio (TF)	0.07	0.06	0.04	0.05
Data $\mu$ + jets	659.5	214.2	74.0	17.8
W + $t\bar{t}$ Prediction	$45.9 \pm 1.8_{\text{stat}} \pm 2.8_{\text{syst}}$	$13.0 \pm 0.9_{\text{stat}} \pm 0.8_{\text{syst}}$	$2.7 \pm 0.3_{\text{stat}} \pm 0.2_{\text{syst}}$	$0.8 \pm 0.2_{\text{stat}} \pm 0.1_{\text{syst}}$
$H_{\text{T}}$ Bin (GeV)	775–875	875–975	975–1075	1075– $\infty$
MC W + $t\bar{t}$	$0.0 \pm 0.0_{\text{stat}}$	$0.0 \pm 0.0_{\text{stat}}$	$0.0 \pm 0.0_{\text{stat}}$	$0.0 \pm 0.0_{\text{stat}}$
MC $\mu$ + jets	$12.8 \pm 1.6_{\text{stat}}$	$6.5 \pm 1.3_{\text{stat}}$	$2.7 \pm 0.8_{\text{stat}}$	$1.9 \pm 0.6_{\text{stat}}$
MC Ratio (TF)	0.00	0.00	0.00	0.00
Data $\mu$ + jets	14.8	4.9	2.0	1.0
W + $t\bar{t}$ Prediction	$0.0 \pm 0.0_{\text{stat}} \pm 0.0_{\text{syst}}$	$0.0 \pm 0.0_{\text{stat}} \pm 0.0_{\text{syst}}$	$0.0 \pm 0.0_{\text{stat}} \pm 0.0_{\text{syst}}$	$0.0 \pm 0.0_{\text{stat}} \pm 0.0_{\text{syst}}$

Table 29: Muon Sample Predictions Normalized to  $19.5\text{fb}^{-1}$  ( $n_{\text{jet}} \geq 4, n_{\text{b}} = 2$ )

$H_{\text{T}}$ Bin (GeV)	375–475	475–575	575–675	675–775
MC W + $t\bar{t}$	$64.8 \pm 3.5_{\text{stat}}$	$42.2 \pm 2.9_{\text{stat}}$	$17.2 \pm 1.9_{\text{stat}}$	$6.7 \pm 1.2_{\text{stat}}$
MC $\mu$ + jets	$735.0 \pm 12.5_{\text{stat}}$	$530.6 \pm 10.6_{\text{stat}}$	$279.3 \pm 7.7_{\text{stat}}$	$134.2 \pm 5.3_{\text{stat}}$
MC Ratio (TF)	0.09	0.08	0.06	0.05
Data $\mu$ + jets	750.4	508.5	270.5	122.4
W + $t\bar{t}$ Prediction	$66.1 \pm 2.4_{\text{stat}} \pm 4.0_{\text{syst}}$	$40.4 \pm 1.8_{\text{stat}} \pm 2.4_{\text{syst}}$	$16.6 \pm 1.0_{\text{stat}} \pm 1.3_{\text{syst}}$	$6.1 \pm 0.5_{\text{stat}} \pm 0.9_{\text{syst}}$
$H_{\text{T}}$ Bin (GeV)	775–875	875–975	975–1075	1075– $\infty$
MC W + $t\bar{t}$	$2.0 \pm 0.6_{\text{stat}}$	$1.4 \pm 0.5_{\text{stat}}$	$0.7 \pm 0.4_{\text{stat}}$	$0.3 \pm 0.2_{\text{stat}}$
MC $\mu$ + jets	$67.7 \pm 3.8_{\text{stat}}$	$35.0 \pm 2.7_{\text{stat}}$	$18.1 \pm 1.9_{\text{stat}}$	$9.7 \pm 1.4_{\text{stat}}$
MC Ratio (TF)	0.03	0.04	0.04	0.03
Data $\mu$ + jets	54.3	18.8	10.9	8.9
W + $t\bar{t}$ Prediction	$1.6 \pm 0.2_{\text{stat}} \pm 0.2_{\text{syst}}$	$0.8 \pm 0.2_{\text{stat}} \pm 0.1_{\text{syst}}$	$0.4 \pm 0.1_{\text{stat}} \pm 0.1_{\text{syst}}$	$0.3 \pm 0.1_{\text{stat}} \pm 0.1_{\text{syst}}$

## **C Maximum likelihood parameter values**

Table 30: SM-only maximum-likelihood parameter values (0b 1e3j).

name	value	error
$\text{EWK}^0$	2.64e+03	4.7e+01
$\text{EWK}^1$	7.59e+02	2.2e+01
$\text{EWK}^2$	2.52e+02	1.1e+01
$\text{EWK}^3$	7.64e+01	6.0e+00
$\text{EWK}^4$	3.37e+01	3.5e+00
$\text{EWK}^5$	1.18e+01	2.0e+00
$\text{EWK}^6$	6.32e+00	1.4e+00
$\text{EWK}^7$	3.15e+00	8.9e-01
$f_{\text{Zinv}}^0$	0.64	0.02
$f_{\text{Zinv}}^1$	0.67	0.02
$f_{\text{Zinv}}^2$	0.70	0.02
$f_{\text{Zinv}}^3$	0.70	0.04
$f_{\text{Zinv}}^4$	0.69	0.04
$f_{\text{Zinv}}^5$	0.76	0.05
$f_{\text{Zinv}}^6$	0.76	0.06
$f_{\text{Zinv}}^7$	0.82	0.06
$\rho_{\mu W}^0$	1.01	0.05
$\rho_{\mu W}^1$	1.00	0.06
$\rho_{\mu W}^2$	1.00	0.07
$\rho_{\mu W}^3$	1.00	0.11
$\rho_{\mu W}^4$	1.01	0.11
$\rho_{\mu W}^5$	1.02	0.16
$\rho_{\mu W}^6$	0.98	0.15
$\rho_{\mu W}^7$	1.00	0.16
$\rho_{\gamma Z}^0$	1.02	0.04
$\rho_{\gamma Z}^1$	0.99	0.04
$\rho_{\gamma Z}^2$	1.00	0.06
$\rho_{\gamma Z}^3$	0.99	0.10
$\rho_{\gamma Z}^4$	1.02	0.11
$\rho_{\gamma Z}^5$	1.05	0.16
$\rho_{\gamma Z}^6$	0.95	0.14
$\rho_{\gamma Z}^7$	0.98	0.15

Table 31: SM-only maximum-likelihood parameter values (1b le3j).

name	value	error
$\text{EWK}^0$	4.13e+02	1.4e+01
$\text{EWK}^1$	1.11e+02	5.9e+00
$\text{EWK}^2$	3.58e+01	3.0e+00
$\text{EWK}^3$	1.01e+01	1.6e+00
$\text{EWK}^4$	3.66e+00	8.2e-01
$\text{EWK}^5$	1.63e+00	6.0e-01
$\text{EWK}^6$	4.87e-01	3.1e-01
$\text{EWK}^7$	1.21e-01	4.7e-02
$f_{\text{Zinv}}^0$	0.47	0.02
$f_{\text{Zinv}}^1$	0.55	0.03
$f_{\text{Zinv}}^2$	0.57	0.04
$f_{\text{Zinv}}^3$	0.64	0.07
$f_{\text{Zinv}}^4$	0.55	0.11
$f_{\text{Zinv}}^5$	0.81	0.08
$f_{\text{Zinv}}^6$	0.82	0.12
$f_{\text{Zinv}}^7$	0.00	0.83
$\rho_{\mu W}^0$	0.95	0.05
$\rho_{\mu W}^1$	0.99	0.06
$\rho_{\mu W}^2$	1.00	0.07
$\rho_{\mu W}^3$	0.98	0.11
$\rho_{\mu W}^4$	1.00	0.11
$\rho_{\mu W}^5$	1.00	0.16
$\rho_{\mu W}^6$	1.00	0.16
$\rho_{\mu W}^7$	1.00	0.16
$\rho_{\gamma Z}^0$	0.96	0.05
$\rho_{\gamma Z}^1$	0.99	0.06
$\rho_{\gamma Z}^2$	1.00	0.07
$\rho_{\gamma Z}^3$	0.96	0.11
$\rho_{\gamma Z}^4$	1.00	0.11
$\rho_{\gamma Z}^5$	0.99	0.15
$\rho_{\gamma Z}^6$	0.99	0.15
$\rho_{\gamma Z}^7$	1.00	0.16



Table 32: SM-only maximum-likelihood parameter values (2b 1e3j).

name	value	error
$\text{EWK}^0$	6.30e+01	3.8e+00
$\text{EWK}^1$	1.80e+01	1.5e+00
$\text{EWK}^2$	4.25e+00	5.4e-01
$\text{EWK}^3$	1.11e+00	2.7e-01
$\text{EWK}^4$	2.10e-01	5.9e-02
$\text{EWK}^5$	3.83e-02	1.8e-02
$\text{EWK}^6$	2.33e-02	1.7e-02
$\text{EWK}^7$	1.30e-03	1.3e-03
$\rho_{\mu W}^0$	0.94	0.05
$\rho_{\mu W}^1$	1.00	0.06
$\rho_{\mu W}^2$	0.98	0.07
$\rho_{\mu W}^3$	0.98	0.11
$\rho_{\mu W}^4$	1.00	0.11
$\rho_{\mu W}^5$	1.00	0.16
$\rho_{\mu W}^6$	1.00	0.16
$\rho_{\mu W}^7$	1.00	0.16

Table 33: SM-only maximum-likelihood parameter values (0b ge4j).

name	value	error
$\text{EWK}^0$	4.60e+02	1.6e+01
$\text{EWK}^1$	2.98e+02	1.2e+01
$\text{EWK}^2$	1.46e+02	8.2e+00
$\text{EWK}^3$	6.59e+01	5.7e+00
$\text{EWK}^4$	2.71e+01	3.3e+00
$\text{EWK}^5$	1.39e+01	2.2e+00
$\text{EWK}^6$	6.47e+00	1.5e+00
$\text{EWK}^7$	3.19e+00	9.5e-01
$f_{\text{Zinv}}^0$	0.52	0.02
$f_{\text{Zinv}}^1$	0.60	0.02
$f_{\text{Zinv}}^2$	0.61	0.03
$f_{\text{Zinv}}^3$	0.63	0.05
$f_{\text{Zinv}}^4$	0.71	0.05
$f_{\text{Zinv}}^5$	0.73	0.06
$f_{\text{Zinv}}^6$	0.74	0.07
$f_{\text{Zinv}}^7$	0.67	0.11
$\rho_{\mu W}^0$	0.98	0.05
$\rho_{\mu W}^1$	1.00	0.06
$\rho_{\mu W}^2$	0.97	0.07
$\rho_{\mu W}^3$	1.00	0.13
$\rho_{\mu W}^4$	1.00	0.13
$\rho_{\mu W}^5$	1.00	0.13
$\rho_{\mu W}^6$	1.00	0.13
$\rho_{\mu W}^7$	1.01	0.19
$\rho_{\gamma Z}^0$	0.98	0.05
$\rho_{\gamma Z}^1$	0.99	0.05
$\rho_{\gamma Z}^2$	0.96	0.07
$\rho_{\gamma Z}^3$	1.00	0.11
$\rho_{\gamma Z}^4$	0.99	0.12
$\rho_{\gamma Z}^5$	0.99	0.12
$\rho_{\gamma Z}^6$	1.01	0.13
$\rho_{\gamma Z}^7$	1.03	0.19

Table 34: SM-only maximum-likelihood parameter values (1b ge4j).

name	value	error
$\text{EWK}^0$	1.92e+02	8.5e+00
$\text{EWK}^1$	1.22e+02	6.1e+00
$\text{EWK}^2$	4.48e+01	3.5e+00
$\text{EWK}^3$	1.71e+01	2.1e+00
$\text{EWK}^4$	6.82e+00	1.3e+00
$\text{EWK}^5$	5.43e+00	1.5e+00
$\text{EWK}^6$	2.43e+00	7.9e-01
$\text{EWK}^7$	1.21e+00	6.3e-01
$f_{\text{Zinv}}^0$	0.23	0.02
$f_{\text{Zinv}}^1$	0.29	0.03
$f_{\text{Zinv}}^2$	0.38	0.05
$f_{\text{Zinv}}^3$	0.36	0.08
$f_{\text{Zinv}}^4$	0.49	0.10
$f_{\text{Zinv}}^5$	0.58	0.12
$f_{\text{Zinv}}^6$	0.70	0.11
$f_{\text{Zinv}}^7$	0.72	0.16
$\rho_{\mu W}^0$	0.99	0.05
$\rho_{\mu W}^1$	0.98	0.05
$\rho_{\mu W}^2$	1.00	0.07
$\rho_{\mu W}^3$	1.03	0.13
$\rho_{\mu W}^4$	0.99	0.13
$\rho_{\mu W}^5$	1.00	0.13
$\rho_{\mu W}^6$	1.00	0.13
$\rho_{\mu W}^7$	1.01	0.19
$\rho_{\gamma Z}^0$	1.00	0.06
$\rho_{\gamma Z}^1$	0.99	0.06
$\rho_{\gamma Z}^2$	1.00	0.08
$\rho_{\gamma Z}^3$	1.02	0.13
$\rho_{\gamma Z}^4$	0.99	0.13
$\rho_{\gamma Z}^5$	0.99	0.13
$\rho_{\gamma Z}^6$	1.01	0.13
$\rho_{\gamma Z}^7$	1.03	0.19

Table 35: SM-only maximum-likelihood parameter values (2b ge4j).

name	value	error
EWK <sup>0</sup>	7.42e+01	4.4e+00
EWK <sup>1</sup>	4.70e+01	3.1e+00
EWK <sup>2</sup>	2.01e+01	1.8e+00
EWK <sup>3</sup>	7.71e+00	1.1e+00
EWK <sup>4</sup>	1.85e+00	3.4e-01
EWK <sup>5</sup>	9.29e-01	2.3e-01
EWK <sup>6</sup>	4.32e-01	1.4e-01
EWK <sup>7</sup>	4.09e-01	1.5e-01
$\rho_{\mu W}^0$	1.01	0.05
$\rho_{\mu W}^1$	0.98	0.05
$\rho_{\mu W}^2$	0.94	0.07
$\rho_{\mu W}^3$	0.93	0.11
$\rho_{\mu W}^4$	1.01	0.13
$\rho_{\mu W}^5$	0.98	0.13
$\rho_{\mu W}^6$	1.01	0.13
$\rho_{\mu W}^7$	0.98	0.18

## D SM-only yield tables

The following tables compare the observations in the hadronic and control samples with the maximum-likelihood expectations obtained by the SM-only fit.

Table 36: 0b 1e3j

$H_T$ Bin (GeV)	375–475	475–575	575–675	675–775	775–875	875–975	975–1075	1075– $\infty$
SM hadronic	$2744^{+48}_{-43}$	$771^{+21}_{-23}$	$254^{+13}_{-13}$	$76.5^{+6.1}_{-4.8}$	$33.7^{+3.7}_{-3.8}$	$11.8^{+1.9}_{-2.1}$	$6.3^{+1.4}_{-1.3}$	$3.2^{+1.0}_{-0.9}$
Data hadronic	2728	766	257	77	32	9	9	4
SM $\mu$ +jets	$9072^{+97}_{-113}$	$3543^{+56}_{-62}$	$1539^{+39}_{-41}$	$686^{+25}_{-26}$	$325^{+17}_{-17}$	$158^{+13}_{-12}$	$78.6^{+7.8}_{-8.3}$	$54.1^{+7.0}_{-6.8}$
Data $\mu$ +jets	9078	3545	1538	686	326	159	78	54
SM $\gamma$ +jets	$3990^{+54}_{-61}$	$1203^{+34}_{-37}$	$410^{+17}_{-19}$	$127^{+10}_{-10}$	$48.8^{+6.0}_{-6.9}$	$19.9^{+3.3}_{-4.2}$	$12.1^{+3.0}_{-2.9}$	$7.7^{+2.9}_{-2.7}$
Data $\gamma$ +jets	4000	1206	408	127	50	22	10	7

Table 37: 0b ge4j

$H_T$ Bin (GeV)	375–475	475–575	575–675	675–775	775–875	875–975	975–1075	1075– $\infty$
SM hadronic	$456^{+15}_{-14}$	$291^{+12}_{-12}$	$148^{+8}_{-7}$	$66.0^{+5.6}_{-5.2}$	$27.1^{+2.9}_{-3.4}$	$14.0^{+1.9}_{-2.1}$	$6.5^{+1.5}_{-1.2}$	$3.2^{+1.0}_{-0.9}$
Data hadronic	480	299	158	66	28	15	6	2
SM $\mu$ +jets	$1260^{+36}_{-36}$	$891^{+29}_{-30}$	$566^{+23}_{-23}$	$308^{+20}_{-14}$	$162^{+11}_{-12}$	$81.3^{+8.6}_{-8.1}$	$46.9^{+7.3}_{-6.1}$	$28.6^{+6.4}_{-4.4}$
Data $\mu$ +jets	1249	888	562	308	162	81	47	29
SM $\gamma$ +jets	$439^{+20}_{-18}$	$349^{+16}_{-18}$	$161^{+10}_{-13}$	$83.0^{+7.9}_{-8.5}$	$32.6^{+5.7}_{-5.6}$	$21.8^{+3.6}_{-4.2}$	$7.7^{+2.4}_{-2.0}$	$4.2^{+1.7}_{-1.7}$
Data $\gamma$ +jets	427	344	155	83	32	21	8	5

Table 38: 1b le3j

$H_T$ Bin (GeV)	375–475	475–575	575–675	675–775	775–875	875–975	975–1075	1075– $\infty$
SM hadronic	$426^{+15}_{-17}$	$114^{+6}_{-6}$	$35.5^{+3.3}_{-2.8}$	$10.1^{+1.4}_{-1.5}$	$3.7^{+0.9}_{-0.8}$	$1.6^{+0.7}_{-0.6}$	$0.5^{+0.3}_{-0.4}$	$0.1^{+0.1}_{-0.0}$
Data hadronic	444	118	36	15	3	2	1	0
SM $\mu$ +jets	$2282^{+50}_{-45}$	$789^{+26}_{-27}$	$325^{+20}_{-17}$	$139^{+11}_{-14}$	$62.7^{+9.2}_{-6.5}$	$25.1^{+4.8}_{-5.1}$	$16.1^{+3.9}_{-4.1}$	$7.9^{+2.9}_{-2.9}$
Data $\mu$ +jets	2272	787	325	137	63	25	16	8
SM $\gamma$ +jets	$452^{+20}_{-22}$	$146^{+9}_{-10}$	$49.3^{+6.6}_{-5.9}$	$18.1^{+3.8}_{-4.4}$	$5.6^{+2.4}_{-2.4}$	$4.3^{+1.9}_{-1.8}$	$1.4^{+1.0}_{-1.4}$	$0.0^{+0.0}_{-0.0}$
Data $\gamma$ +jets	444	144	49	15	6	4	1	0

Table 39: 1b ge4j

$H_T$ Bin (GeV)	375–475	475–575	575–675	675–775	775–875	875–975	975–1075	1075– $\infty$
SM hadronic	$190^{+10}_{-8}$	$120^{+6}_{-5}$	$45.6^{+3.1}_{-3.8}$	$17.1^{+2.6}_{-1.9}$	$6.8^{+1.5}_{-1.3}$	$5.4^{+1.3}_{-1.6}$	$2.4^{+0.9}_{-0.9}$	$1.2^{+0.7}_{-0.8}$
Data hadronic	206	135	45	14	8	6	2	0
SM $\mu$ +jets	$1250^{+37}_{-28}$	$891^{+27}_{-31}$	$385^{+21}_{-20}$	$200^{+12}_{-12}$	$86.6^{+9.0}_{-10.1}$	$55.3^{+7.7}_{-7.3}$	$24.9^{+4.4}_{-5.3}$	$10.7^{+3.1}_{-3.4}$
Data $\mu$ +jets	1238	881	385	202	86	55	25	11
SM $\gamma$ +jets	$102^{+10}_{-9}$	$81.3^{+8.2}_{-7.9}$	$32.7^{+5.5}_{-5.6}$	$11.9^{+3.7}_{-3.0}$	$7.6^{+2.6}_{-2.6}$	$3.3^{+1.2}_{-1.6}$	$3.7^{+1.9}_{-1.9}$	$1.1^{+0.8}_{-1.1}$
Data $\gamma$ +jets	98	77	33	13	7	3	4	2

Table 40: 2b le3j

$H_T$ Bin (GeV)	375–475	475–575	575–675	675–775	775–875	875–975	975–1075	1075– $\infty$
SM hadronic	$65.0^{+4.3}_{-4.3}$	$18.4^{+1.7}_{-1.6}$	$4.2^{+0.6}_{-0.5}$	$1.1^{+0.3}_{-0.2}$	$0.2^{+0.1}_{-0.1}$	$0.0^{+0.0}_{-0.0}$	$0.0^{+0.0}_{-0.0}$	$0.0^{+0.0}_{-0.0}$
Data hadronic	78	18	8	3	0	0	0	0
SM $\mu$ +jets	$681^{+26}_{-31}$	$217^{+14}_{-14}$	$78.8^{+9.4}_{-9.3}$	$19.9^{+4.1}_{-3.8}$	$14.8^{+4.0}_{-3.9}$	$5.0^{+2.0}_{-2.1}$	$2.0^{+1.0}_{-1.0}$	$1.0^{+1.0}_{-1.0}$
Data $\mu$ +jets	668	217	75	18	15	5	2	1
Data $\gamma$ +jets	36	8	4	0	0	1	0	0

Table 41: 2b ge4j

$H_T$ Bin (GeV)	375–475	475–575	575–675	675–775	775–875	875–975	975–1075	1075– $\infty$
SM hadronic	$73.6^{+4.2}_{-4.2}$	$45.7^{+2.8}_{-2.9}$	$20.4^{+1.8}_{-1.8}$	$7.7^{+1.2}_{-1.0}$	$1.9^{+0.3}_{-0.3}$	$0.9^{+0.2}_{-0.2}$	$0.4^{+0.1}_{-0.1}$	$0.4^{+0.1}_{-0.2}$
Data hadronic	79	52	31	12	1	2	0	1
SM $\mu$ +jets	$765^{+26}_{-27}$	$521^{+23}_{-22}$	$285^{+15}_{-17}$	$128^{+12}_{-10}$	$54.1^{+7.5}_{-8.0}$	$20.1^{+4.6}_{-4.1}$	$10.6^{+2.9}_{-2.9}$	$9.6^{+2.9}_{-2.9}$
Data $\mu$ +jets	760	515	274	124	55	19	11	9
Data $\gamma$ +jets	19	17	10	4	0	2	1	0

## E Efficiencies and systematic uncertainties for simplified models

### E.1 T2cc

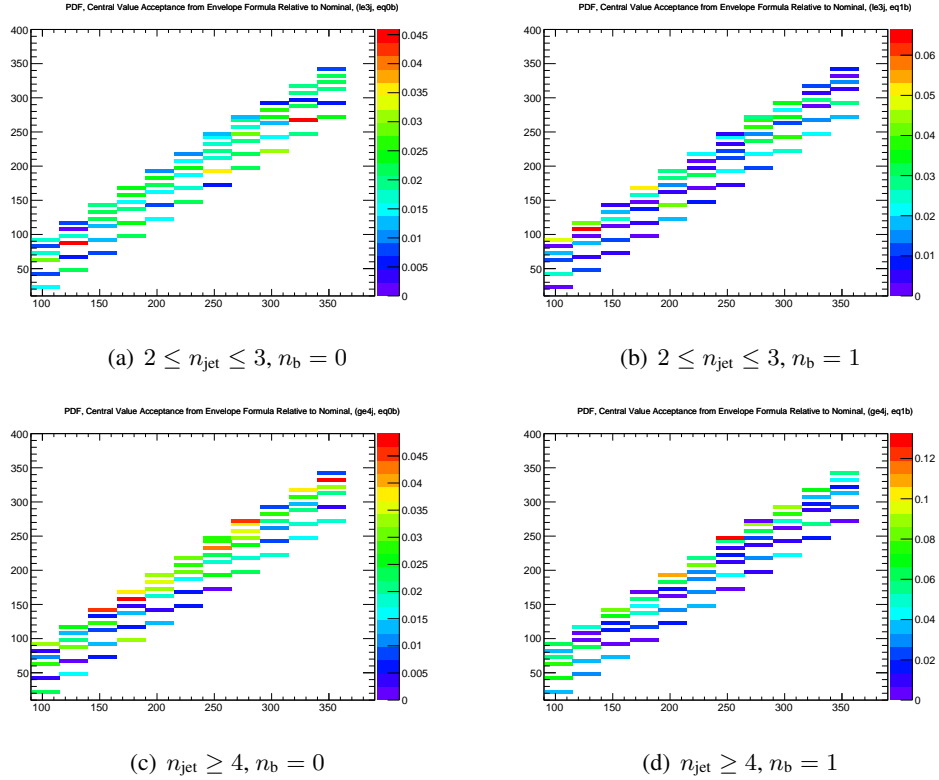


Figure E.1: Ratio of efficiency times acceptance for the (middle) central value, (top)  $+1\sigma$  value, (bottom)  $-1\sigma$  value of the envelope calculation relative to the nominal PDF set used to produce the T2cc sample.



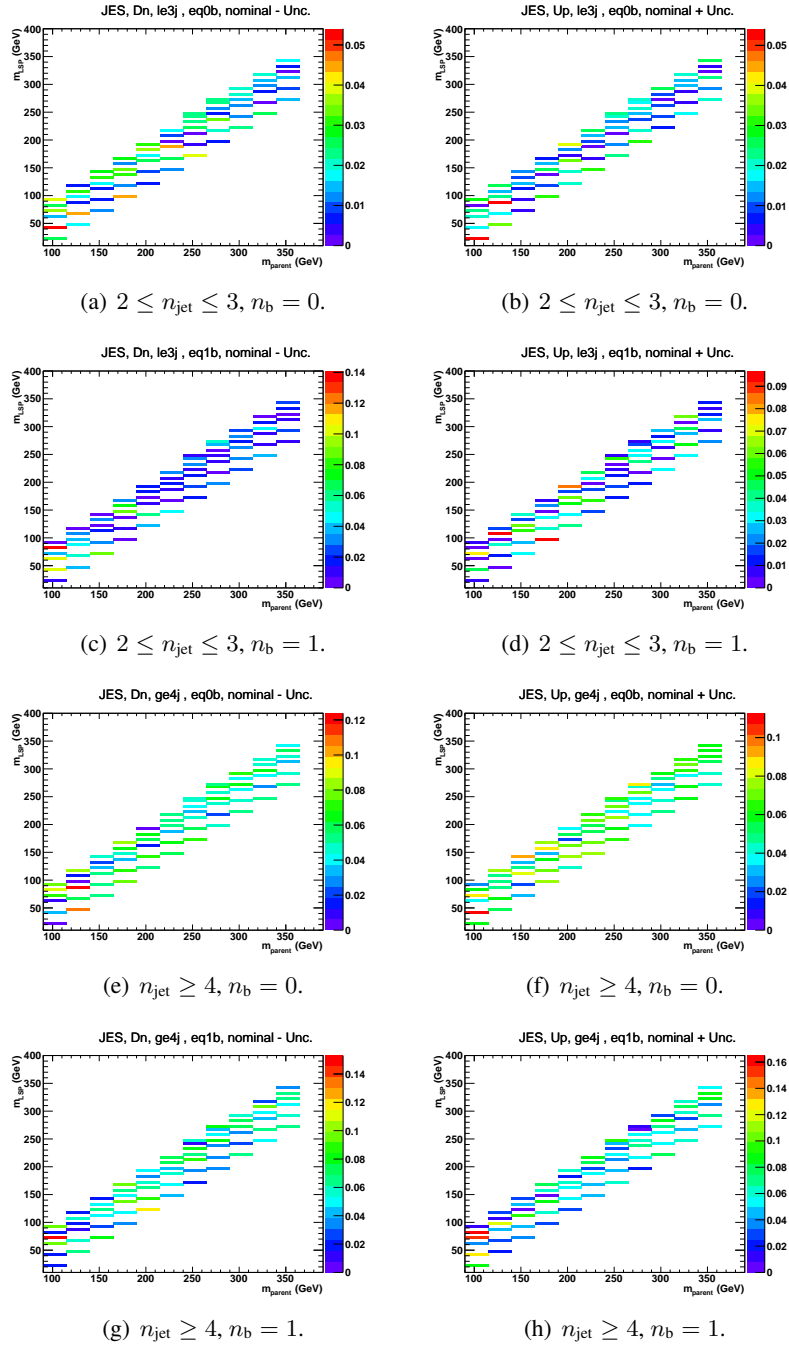


Figure E.2: The fractional change in signal efficiency due to systematically (Left) increasing and (Middle) decreasing all jet energies, and (Right) the resulting (symmetric) systematic uncertainties due to JES uncertainties for T2cc.

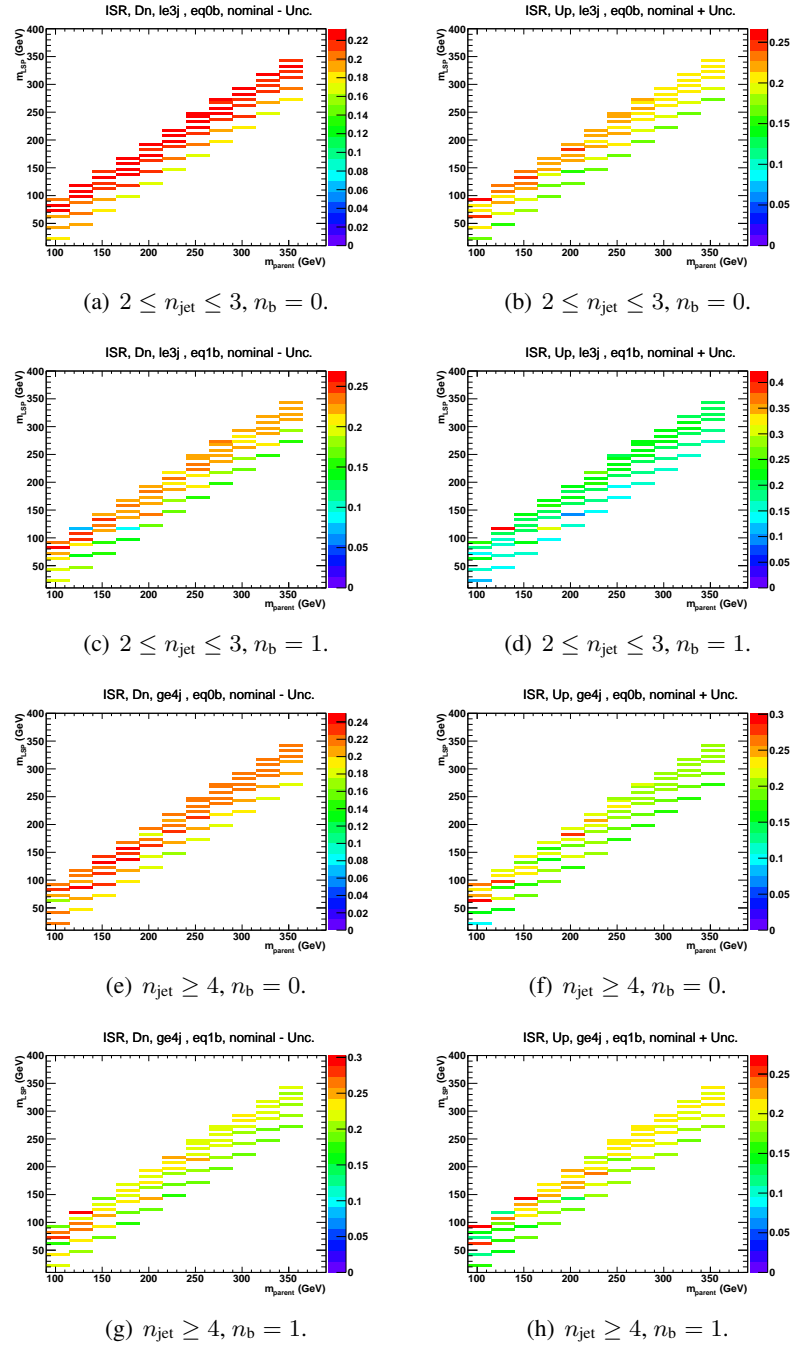


Figure E.3: The fractional change in signal efficiency due to systematically (Left) increasing and (Middle) decreasing event weights according to ISR uncertainties, and (Right) the resulting (symmetric) systematic uncertainties due to ISR uncertainties for T2cc.

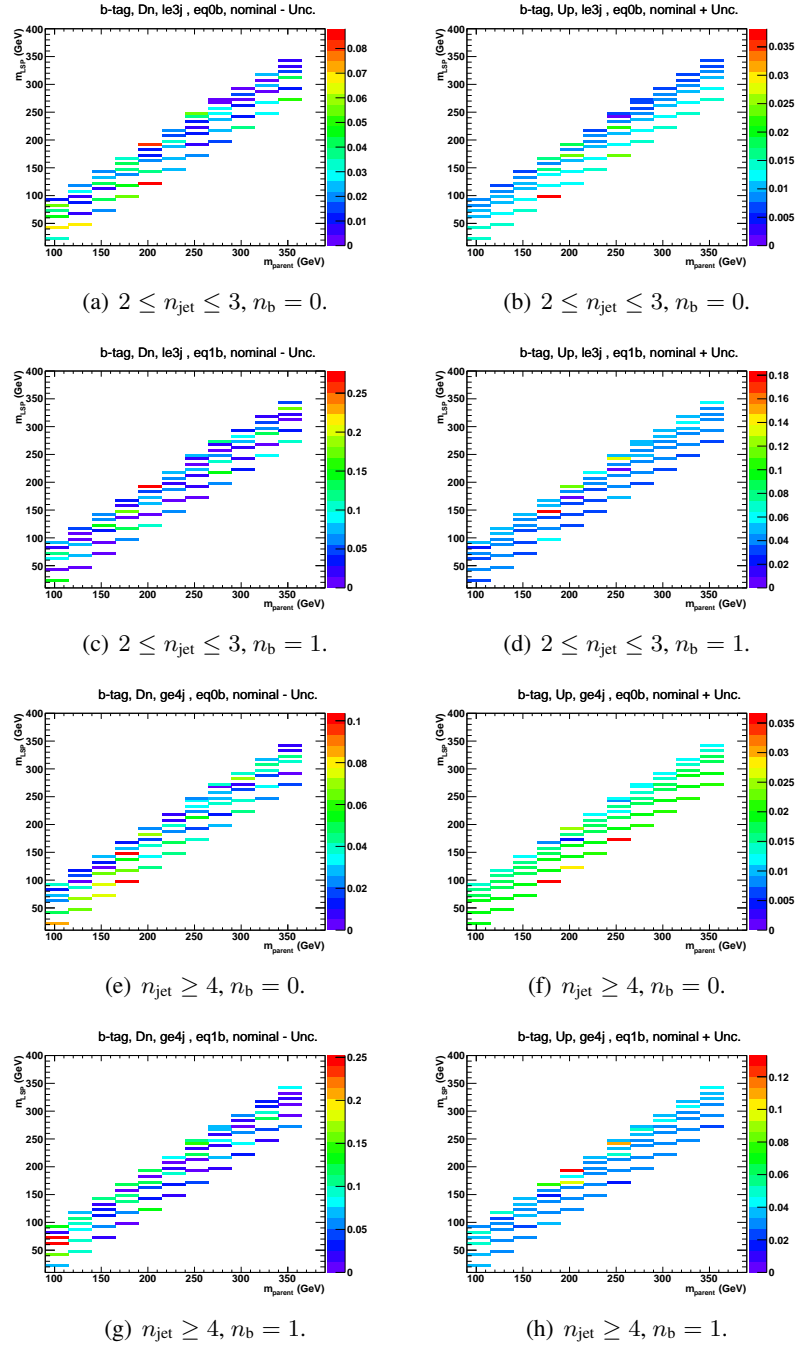


Figure E.4: The fractional change in signal efficiency due to systematically (Left) increasing and (Middle) decreasing all b-tag efficiencies according to the scale factor uncertainties, and (Right) the resulting (symmetric) systematic uncertainties due to b-tag scale factor uncertainties for T2cc.

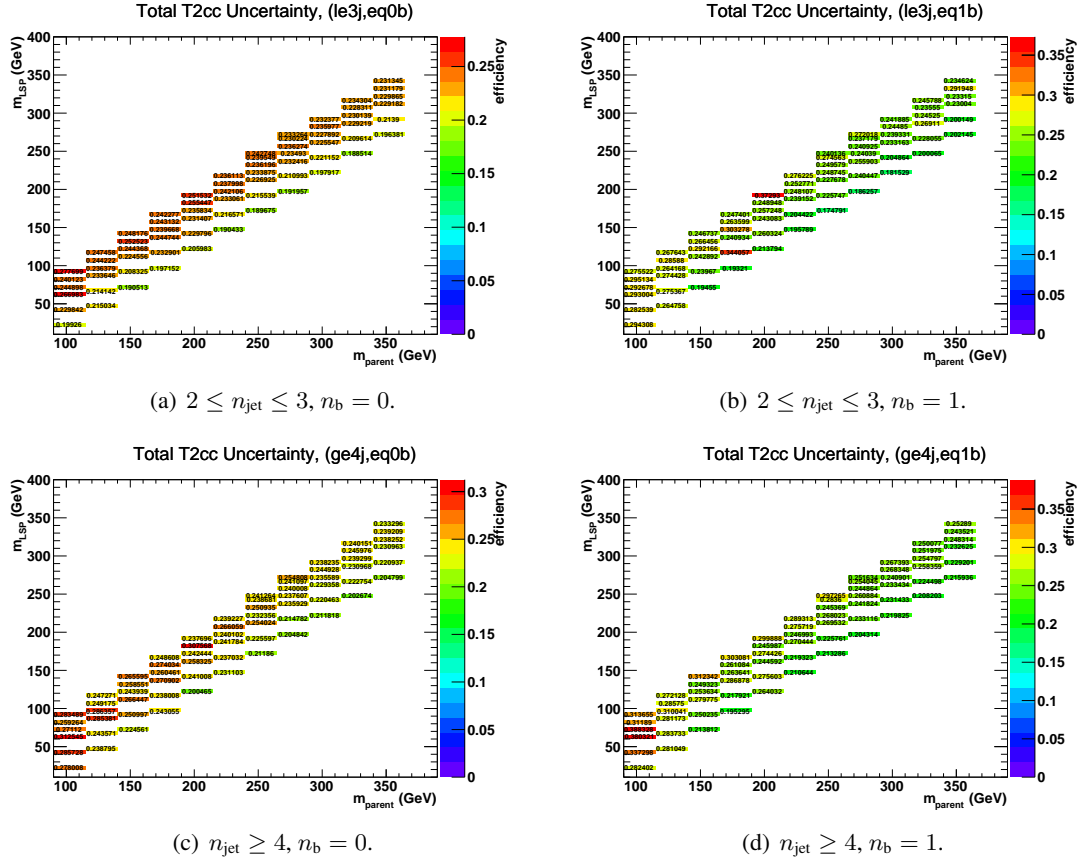


Figure E.5: The total systematic uncertainty in the signal efficiency times acceptance for all relevant event categories for the T2cc interpretation.

## E.2 T2tt

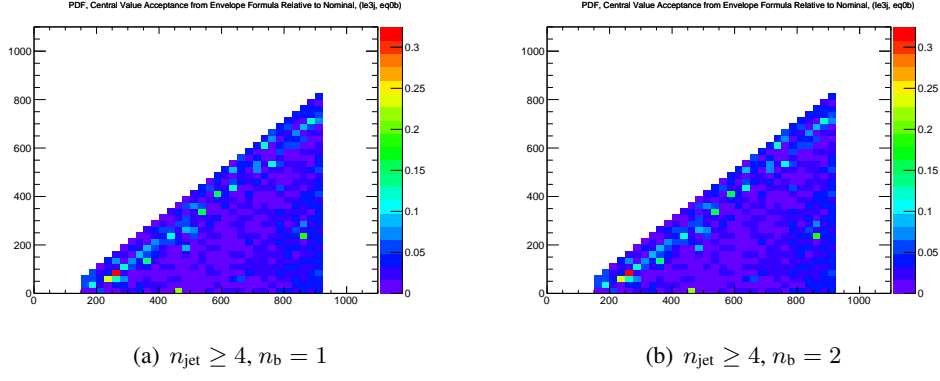


Figure E.6: Ratio of efficiency times acceptance for the (middle) central value, (top)  $+1\sigma$  value, (bottom)  $-1\sigma$  value of the envelope calculation relative to the nominal PDF set used to produce the T2tt sample.

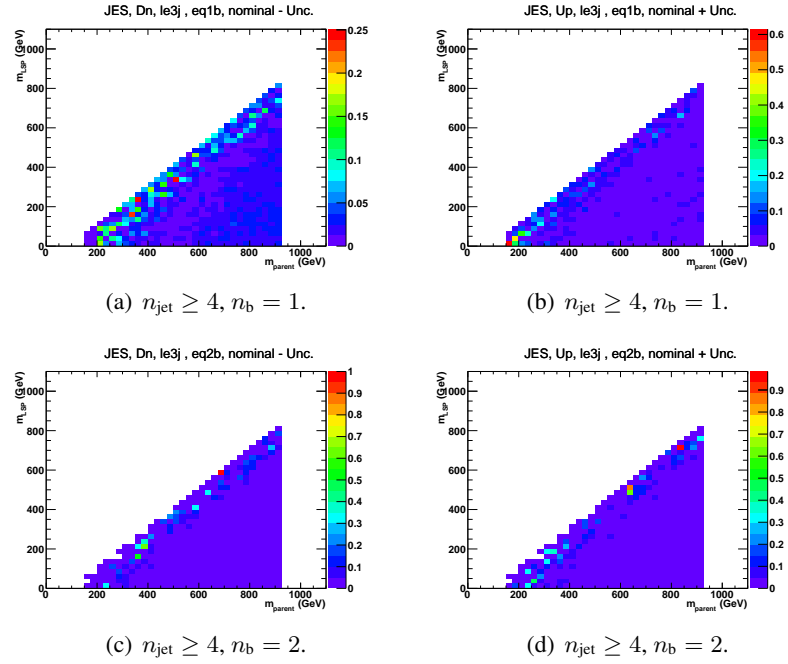


Figure E.7: The fractional change in signal efficiency due to systematically (Left) increasing and (Middle) decreasing all jet energies, and (Right) the resulting (symmetric) systematic uncertainties due to JES uncertainties for  $T2\tau\tau$ .

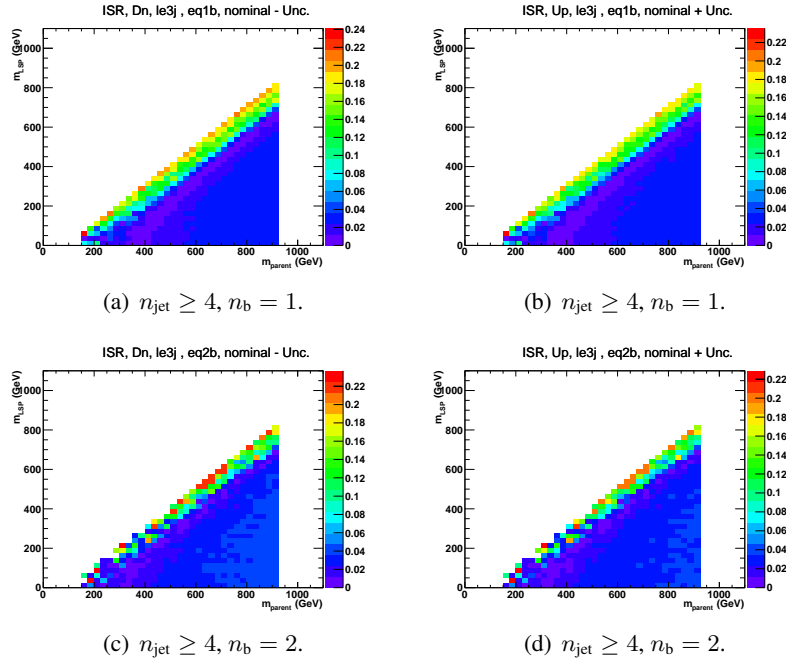


Figure E.8: The fractional change in signal efficiency due to systematically (Left) increasing and (Middle) decreasing event weights according to ISR uncertainties, and (Right) the resulting (symmetric) systematic uncertainties due to ISR uncertainties for T2tt.

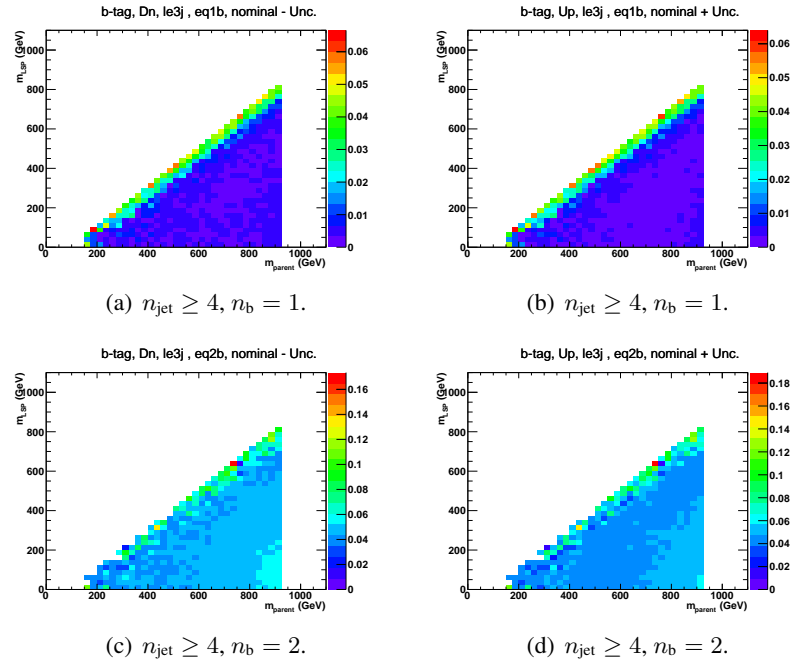


Figure E.9: The fractional change in signal efficiency due to systematically (Left) increasing and (Middle) decreasing all b-tag efficiencies according to the scale factor uncertainties, and (Right) the resulting (symmetric) systematic uncertainties due to b-tag scale factor uncertainties for  $T2t\bar{t}$ .



## References

- [1] A. Bettini. *Introduction to Elementary Particle Physics*. Cambridge University Press, 2014.
- [2] D. Griffiths. *Introduction to Elementary Particles*. Physics textbook. Wiley, 2008.
- [3] D.H. Perkins. *Introduction to High Energy Physics*. Cambridge University Press, 2000.
- [4] Stephen P. Martin. A Supersymmetry primer. *Adv.Ser.Direct.High Energy Phys.*, 21:1–153, 2010.
- [5] J. Wess and J. Bagger. *Supersymmetry and Supergravity*. Princeton series in physics. Princeton University Press, 1992.
- [6] R. Keith Ellis, W. James Stirling, and B.R. Webber. QCD and collider physics. *Camb.Monogr.Part.Phys.Nucl.Phys.Cosmol.*, 8:1–435, 1996.
- [7] Daniele Alves et al. Simplified Models for LHC New Physics Searches. *J.Phys.*, G39:105005, 2012.
- [8] W.J. Stirling. private communication. <http://www.hep.ph.ic.ac.uk/~wstirling/plots/plots.html>.
- [9] W. Beenakker, R. Hopker, and M. Spira. PROSPINO: A Program for the production of supersymmetric particles in next-to-leading order QCD. 1996.
- [10] S. Chatrchyan et al. The cms experiment at the cern lhc. *Journal of Instrumentation*, 3(08):S08004, 2008.
- [11] The CMS Collaboration. Performance of CMS muon reconstruction in pp collision events at  $\sqrt{s} = 7$  TeV. *Journal of Instrumentation*, 7:2P, October 2012.
- [12] Absolute Calibration of the Luminosity Measurement at CMS: Winter 2012 Update. Technical Report CMS-PAS-SMP-12-008, CERN, Geneva, 2012.

- [13] G L Bayatian et al. *CMS Physics: Technical Design Report Volume 1: Detector Performance and Software*. Technical Design Report CMS. CERN, Geneva, 2006. There is an error on cover due to a technical problem for some items.
- [14] G L Bayatian et al. CMS Physics: Technical Design Report Volume 2: Physics Performance. *J. Phys. G*, 34(CERN-LHCC-2006-021. CMS-TDR-8-2):995–1579. 669 p, 2007. revised version submitted on 2006-09-22 17:44:47.
- [15] CMS Collaboration. Performance of muon identification in pp collisions at  $\sqrt{s} = 7$  tev. CMS Physics Analysis Summary MUO-10-002, CMS, 2010.
- [16] M. Cacciari, G. P. Salam, and G. Soyez. The anti- $k_t$  jet clustering algorithm. *JHEP*, 04:063, 2008.
- [17] Serguei Chatrchyan et al. Determination of Jet Energy Calibration and Transverse Momentum Resolution in CMS. *JINST*, 6:P11002, 2011.
- [18] The CMS collaboration. Missing transverse energy performance of the cms detector. *Journal of Instrumentation*, 6(09):P09001, 2011.
- [19] CMS Collaboration. Matching simulated pileup distribution to data conditions. [https://twiki.cern.ch/twiki/bin/view/CMSPublic/SWGuideFastSimPileUp#Access\\_to\\_the\\_true\\_pile\\_up\\_distr](https://twiki.cern.ch/twiki/bin/view/CMSPublic/SWGuideFastSimPileUp#Access_to_the_true_pile_up_distr).
- [20] CMS Collaboration. Standard Model cross sections at 8 TeV. <https://twiki.cern.ch/twiki/bin/viewauth/CMS/StandardModelCrossSectionsat8TeV>.
- [21] CMS Collaboration. LO cross sections from the PREP tool. <http://cms.cern.ch/iCMS/rep/requestmanagement>.
- [22] R. Bainbridge, S. A. Koay. DY+jets at 8TeV: comparison of HT and Njet binned samples. <https://indico.cern.ch/event/271369/>.
- [23] V. Khachatryan et al. Search for Supersymmetry in pp Collisions at 7 TeV in Events with Jets and Missing Transverse Energy. *Phys. Lett. B*, 698:196, 2011.

- [24] CMS Collaboration. MET Optional Filters. <https://twiki.cern.ch/twiki/bin/view/CMS/MissingETOptionalFilters>.
- [25] CMS Collaboration. Particleflow event reconstruction in cms and performance for jets, taus, and  $\cancel{E}_T$ . CMS Physics Analysis Summary PFT-09-001, CMS, 2009.
- [26] Matteo Cacciari and Gavin P. Salam. Pileup subtraction using jet areas. *Physics Letters B*, 659:119 – 126, 2008.
- [27] Matteo Cacciari, Gavin P. Salam, and Gregory Soyez. The catchment area of jets. *Journal of High Energy Physics*, 2008(04):005, 2008.
- [28] CMS Collaboration. Jet ID. <https://twiki.cern.ch/twiki/bin/viewauth/CMS/JetID>.
- [29] S. Chatrchyan et al. Identification of b-quark jets with the cms experiment. *JINST*, 8:P04013, 2013.
- [30] CMS Collaboration. Baseline Muon ID. <https://twiki.cern.ch/twiki/bin/view/CMSPublic/SWGuideMuonId>.
- [31] CMS Collaboration. Egamma cut-based photon ID. <https://twiki.cern.ch/twiki/bin/view/CMS/CutBasedPhotonID2012>.
- [32] CMS Collaboration. Egamma cut-based electron ID. <https://twiki.cern.ch/twiki/bin/view/CMS/EgammaCutBasedIdentification>.
- [33] CMS Collaboration. Egamma Particle Flow Based Isolation. <https://twiki.cern.ch/twiki/bin/view/CMS/EgammaPFBasedIsolation>.
- [34] CMS Collaboration. MET Corrections. <https://twiki.cern.ch/twiki/bin/view/CMS/MissingET>.
- [35] [http://cms.cern.ch/iCMS/jsp/db\\_notes/noteInfo.jsp?cmsnoteid=CMSAN-2013/089](http://cms.cern.ch/iCMS/jsp/db_notes/noteInfo.jsp?cmsnoteid=CMSAN-2013/089). Search for Direct Top Squark Pair Production in the Single Lepton Channel with Transverse Mass at 8 TeV, CMS AN-2013/089.

- 
- [36] S. Chatrchyan et al. Search for supersymmetry in hadronic final states with missing transverse energy using the variables  $\alpha_T$  and b-quark multiplicity in pp collisions at  $\sqrt{s} = 8$  TeV. *EPJC*, 01:077, 2013.
- [37] CMS Collaboration. Electron reconstruction and identification at  $\sqrt{s} = 7$  tev. CMS Physics Analysis Summary EGM-10-004, CMS, 2010.
- [38] Search for supersymmetry in two-photons+jet events with razor variables in pp collisions at  $\sqrt{s} = 8$  TeV. Technical Report CMS-PAS-SUS-14-008, CERN, Geneva, 2014.
- [39] V. Khachatryan et al. Search for new physics in events with photons, jets, and missing transverse energy in pp collisions at  $\sqrt{s} = 7$  TeV. *JHEP*, 03:111, 2013.
- [40] CMS Collaboration. Isolated photon reconstruction and identification at  $\sqrt{s} = 7$  tev. CMS Physics Analysis Summary EGM-10-006, CMS, 2010.
- [41] L. Randall and D. Tucker-Smith. Dijet searches for supersymmetry at the large hadron collider. *Phys. Rev. Lett.*, 101:221803, 2008.
- [42] CMS Collaboration. Search strategy for exclusive multi-jet events from supersymmetry at cms. CMS Physics Analysis Summary SUS-09-001, CMS, 2009.
- [43] CMS Collaboration. Data-driven estimation of the invisible Z background to the SUSY MET plus jets search. CMS Physics Analysis Summary SUS-08-002, CMS, 2008.
- [44] Z. Bern, G. Diana, L.J. Dixon, F. Febres Cordero, S. Hoche, et al. Driving Missing Data at Next-to-Leading Order. *Phys.Rev.*, D84:114002, 2011.
- [45] S. Chatrchyan et al. Search for supersymmetry at the lhc in events with jets and missing transverse energy. *Phys. Rev. Lett.*, 107:221804, 2011.
- [46] CMS Collaboration. Muon Trigger Efficiencies. <https://twiki.cern.ch/twiki/bin/view/CMS/MuonReferenceEffs>.

- [47] Robert Cousins. Probability Density Functions for Positive Nuisance Parameters. [http://www.physics.ucla.edu/~cousins/stats/cousins\\_lognormal\\_prior.pdf](http://www.physics.ucla.edu/~cousins/stats/cousins_lognormal_prior.pdf).
- [48] Wouter Verkerke and David Kirkby. RooFit. <http://root.cern.ch/drupal/content/roofit>.
- [49] F. James and M. Roos. Minuit: A System for Function Minimization and Analysis of the Parameter Errors and Correlations. *Comput.Phys.Commun.*, 10:343–367, 1975.
- [50] Glen D Cowan. *Statistical data analysis*. Oxford Univ. Press, Oxford, 1998.
- [51] Johan Alwall, Philip Schuster, and Natalia Toro. Simplified Models for a First Characterization of New Physics at the LHC. *Phys. Rev.*, D79:075020, 2009.
- [52] Johan Alwall, My-Phuong Le, Mariangela Lisanti, and Jay G. Wacker. Model-Independent Jets plus Missing Energy Searches. *Phys.Rev.*, D79:015005, 2009.
- [53] D. Alves, N. Arkani-Hamed, S. Arora, et al. Simplified models for lhc new physics searches. 2011. Official summary of results from the 'Topologies for Early LHC Searches' workshop, SLAC, September 2010.
- [54] Johan Alwall et al. MadGraph/MadEvent v4: The New Web Generation. *JHEP*, 09:028, 2007.
- [55] M. Botje, J. Butterworth, A. Cooper-Sarkar, et al. The pdf4lhc working group interim recommendations. 2011.
- [56] D. Olivito, F. Wurthwein, et al. Hadronic recoil studies of heavy boosted systems, an -2013/059.
- [57] <https://twiki.cern.ch/twiki/bin/viewauth/CMS/BtagPOG>.
- [58] Edward M. Laird. *A Search for Squarks and Gluinos with the CMS Detector*. PhD thesis, Princeton University, 2011.

- 
- [59] G. Cowan et al. Asymptotic formulae for likelihood-based tests of new physics. *Eur. Phys. J. C*, 71:1554, 2011.
- [60] A. L. Read. Presentation of search results: the  $CL_s$  technique. *J. Phys. G*, 28:2693, 2002.
- [61] T Junk. Confidence level computation for combining searches with small statistics. *Nucl. Instr. and Meth. A*, 434:435, 1999.
- [62] Lorenzo Moneta, Kevin Belasco, Kyle Cranmer, Alfio Lazzaro, Danilo Piparo, Gregory Schott, Wouter Verkerke, Matthias Wolf, Kevin Belasco, Kyle Cranmer, Alfio Lazzaro, Danilo Piparo, Gregory Schott, Wouter Verkerke, and Matthias Wolf. The RooStats Project. *PoS, ACAT2010*(arXiv:1009.1003):057, Sep 2010. Comments: 11 pages, 3 figures, ACAT2010 Conference Proceedings.
- [63] G. Aad et al. The ATLAS Experiment at the CERN Large Hadron Collider. *JINST*, 3:S08003, 2008.
- [64] Georges Aad et al. Search for pair-produced third-generation squarks decaying via charm quarks or in compressed supersymmetric scenarios in  $pp$  collisions at  $\sqrt{s} = 8$  TeV with the ATLAS detector. *Phys.Rev.*, D90:052008, 2014.